Non-invasive monitoring

of water and solute fluxes in a cropped soil

I n a u g u r a l – D i s s e r t a t i o n

zur

Erlangung des Grades

Doktor der Agrarwissenschaften

(Dr.agr.)

der

Hohen Landwirtschaftlichen Fakultät

der

Rheinischen Friedrich-Wilhelms-Universität

zu Bonn

vorgelegt am 14. September 2010

von Sarah Garré

aus Halle, Belgien

Science is the poetry of reality.

Richard Dawkins

Acknowledgements

The pages of this book represent many questions and some answers, intense and pleasant collaborations, long and complex discussions and internal debate and most of all it represents the pleasure of curiosity. This book is not the work of one person only. On the contrary, it wouldn't exist if it were not for the many helping hands and minds I've been lucky to meet during the past years.

N. Hermes, F. Engels, A. Weuthen und J. Höltkemeier haben mir den Weg gezeigt durch einen Wald von Kabel, Multiplexer, Ventile und Schläuche. Ihre Arbeit und Ihre Begeisterung für das Projekt, haben es möglich gemacht viele complexe Messungen im Lysimeterkeller durch zu führen.

Measuring is one thing. Understanding the measurements is another. I would like to thank Prof. J. Vanderborght and Prof. M. Javaux for the support, their many ideas and their patience. It was a joy to be allowed to develop a personal way of working and yet receive valued support. Additionally, I wish to thank them and the institute leader Prof. H. Vereecken for the possibility they gave me to work in the Agrosphere institute and within the framework of the INVEST project. Next to the funding, the INVEST group provided interesting links to scientists from other universities. Un grand merci aussi à prof. L. Pagès de l'INRA Avignon pour les deux mois extraordinaires à Avignon.

I would also like to thank Dr. T. Pütz and Dr. W. Mittelstaedt for the lysimeter excavation and R. Harms and H. Rützel for technical support in the control area and in the field. I am very grateful for the measurements and analyses of Dr. R. Kasteel and A. Langen from the soil physics lab as well as for the help of Dr. L. Weihermüller and Dr. S. Huisman with the TDR calibration and other big and small issues. I would like to thank all the PhD students of the ICG-4 and especially my colleagues Dr. J. Köstel and M. Bechtold for their help when I needed it. Many thanks to M. Vanderploeg (Wageningen) and E. Laloy (Louvain-la-neuve) as well for inspiring conversations about work and other things. Dankeschön auch an T. Muckenheim und W. Tappe für den morgendlichen Kaffee.

Summary

Although the influence of root water uptake on solute transport is commonly recognized as important, it has barely been studied throughout the literature. However, plants take up a big amount of the infiltrating water and therefore they influence water flow patterns in the soil and concurrently solute transport processes. For this reason, experiments are required to investigate the relationship between plant root water uptake and flow field variability. Within this PhD project, we tried to elucidate the role of root water uptake on soil moisture distribution and solute transport in two undisturbed soil columns. During three consecutive experimental phases, the soil hydraulic and solute transport characteristics were investigated and the influence of growing barley on water content and tracer movement were studied. Soil water concentration and moisture content in the lysimeters were monitored non-invasively using 3-D electrical resistivity tomography (ERT). Next to that, time domain reflectometry (TDR) probes, tensiometers and temperature probes were installed to measure local soil water contents, matrix potentials and electrical conductivities. Also the outflow volume and the electrical conductivity of the effluent were registered.

ERT is a valuable technique to monitor processes in the unsaturated zone. It is suitable to quantify solute concentration or soil moisture content at the decimeter scale in different soils and under varying conditions. In combination with TDR and effluent measurements, different aspects of the solute transport process and manifestations of preferential flow can be investigated. Steady-state step tracer experiments are very suitable for this purpose, since the water content is kept constant during tracer movement. Soil moisture measurements with ERT were conducted as well, but an horizon-specific in-situ calibration of the ERT-measurements for water content was a prerequisite for success.

We observed that the solute transport in our silty lysimeters was considerably more heterogeneous than in the loamy-sand soil studied by Koestel (2008; 2009a; 2009b). We observed a clear preferential flow path in one of the lysimeters and found that soil layering had a big influence on the leaching process. During the cropped soil experiment under barley without irrigation, we observed a rather high soil moisture variability as compared to values reported in the literature for bare soil. The measured

water depletion rate, being the result of combined effects of root water uptake and soil water redistribution, was compared with the evaporative demand and root length densities. We could observe a gradual downward movement of the maximum water depletion rate together with periods of redistribution when there was less transpiration. However, we were unable to make the distinction between soil water fluxes and root water uptake, since modeling of the soil water flow field using the time series of water content was not satisfying. We observed root growth at rhizotube surfaces and noted an increasing number of roots with depth. In one lysimeter, we tested the influence of remaining salt tracer in the soil matrix. The number of roots in the saline part was markedly lower than in the lysimeter without tracer at the same depth. Since the minirhizotron measurements were only conducted at four depths and thus represent a small volume of the entire root zone, we estimated a root architecture model for the barley plants using RootTyp. We were able to set up a simple model, but to obtain better results, the effect of soil constraints and the process of re-iteration should be included.

Many aspects of water flow and solute transport in the root zone need to be further investigated. The need for high-quality soil moisture data and simultaneous root architecture data remains. ERT is a promising technique to fill part of this gap, however some issues need to be solved before it can be used without difficulties. Next to measurements, the effort to improve our soil water flow models must be continued in order to improve the estimation of soil water fluxes. Only in this way, we will be able to measure root water uptake at the lysimeter and field scale. This is a necessary step towards a better understanding of the interactions in the soil-plant continuum.

Kurzfassung

Pflanzen können über die Wurzel große Mengen an Wasser aufnehmen und dadurch die Fließ- und Transportwege in Böden wesentlich verändern. Dieser Einfluss wird zwar allgemein als wichtig erachtet, jedoch sind die zugrundeliegenden Prozesse kaum untersucht. Im Rahmen dieser Doktorarbeit wurde die Rolle der Wasseraufnahme durch Pflanzen bezüglich der Verteilung der Bodenfeuchte und beim Stofftransport mittels einem nicht-invasiven Messverfahren an zwei ungestörten Bodensäulen untersucht. In drei aufeinander folgenden Versuchsphasen wurden die hydraulischen und Transporteigenschaften des Bodens sowie der Einfluss wachsender Gerste auf den Wassergehalt und die Verlagerung zugefügter Salztracer ermittelt. Der Bodenfeuchtegehalt und die Leitfähigkeit des Porenwassers in den Lysimetern wurde mithilfe der dreidimensionalen elektrischen Widerstandstomographie (ERT) nicht-invasiv überwacht. Der lokale Wassergehalt und die elektrische Leitfähigkeit des Bodens wurden mittels Time-Domain-Reflectrometry-(TDR)-Sonden gemessen. Darüber hinaus wurden das Volumen und die elektrische Leitfähigkeit des Abflusses aufgezeichnet sowie die Bodentemperatur und Saugspannung gemessen.

ERT ermöglicht die Quantifizierung gelöster Stoffkonzentrationen bzw. der Bodenfeuchte in unterschiedlichen Böden und unter wechselnden Bedingungen im Dezimeterbereich und ist geeignet, zeitliche Veränderungen in der ungesättigten Zone zu erfassen. In Verbindung mit TDR- und Abflussmessungen können so verschiedene Aspekte des Stofftransports und Ausprägungen des präferentiellen Flusses untersucht werden. Step-Tracer-Versuche unter stationären Fließbedingungen sind dafür besonders zweckmäßig, da der Wassergehalt während des Stofftransportes zeitlich konstant bleibt. Darüber hinaus ermöglichten die ERT-Messungen unter Verwendung einer horizontspezifischen in-situ-Kalibrierung eine erfolgreiche Charakterisierung der räumlichen Variabilität der Bodenfeuchte.

Der Stofftransport in den mit Schluffboden gefüllten Lysimetern erwies sich als weitaus heterogener als in den von Koestel et al. (2008; 2009a; 2009b) untersuchten lehmigen Sandböden. Auch wurde ein deutlicher präferentieller Fluss in einem der Lysimeter beobachtet und festgestellt, dass der Bodenaufbau mit verschiedenen Horizonten einen großen Einfluss auf den Versickerungsprozess hat. Im Gersteversuch ohne Bewässerung wurde im Vergleich zu den in der Literatur angegebenen Werten für vegetationslose Böden eine recht hohe Variabilität der Bodenfeuchte beobachtet. Die gemessene Wasserverlustrate, die aus dem Zusammenwirken von Wurzelwasseraufnahme und Umverteilung von Bodenwasser resultiert, wurde mit der potenziellen Verdunstung und Wurzellängendichte verglichen. Dabei wurde eine schrittweise Verringerung der maximalen Wasserverlustrate mit der Tiefe zusammen mit Umverteilungsphasen bei niedriger Transpiration beobachtet. Die Aufschlüsselung der Wasseraufnahme zwischen Wurzel und Umverteilungsmechanismen konnte jedoch mittels 3D-Modellierung nicht zufriedenstellend gelöst werden. Das Wurzelwachstum wurde anhand von Minirhizotron-Röhren untersucht. An der Oberfläche der Röhren wurde mit wachsender Tiefe eine steigende Anzahl von Wurzeln beobachtet. In einem der Lysimeter wurde die Wirkung von in der Bodenmatrix verbleibendem salzhaltigen Tracer untersucht. Die Zahl der Wurzeln im salzhaltigen Boden war bei gleicher Tiefe bedeutend geringer als im Lysimeter ohne Tracer. Zur Quantifizierung der Wurzelarchitektur wurde ein einfaches Wurzelmodell (anhand RootTyp) für die Gerstepflanzen erstellt. Auswertung der Ergebnisse zeigte jedoch, das die Wirkung von verschiedenen Bodenhorizonten und die Möglichkeit einer Reiteration bestimmter Wurzeln berücksichtigt werden müssen.

Die Ergebnisse der Arbeit zeigen klar, dass die simultane und nicht-invasive Erfassung von Bodenfeuchte und Wurzelarchitektur unabdingbar ist, um die Rolle der Wasserwurzelaufnahme auf Stoffflüsse in Böden besser zu verstehen. ERT ist ein aussichtsreiches Verfahren, um diese Lücke zumindest teilweise zu

schließen. Allerdings sind noch einige Verbesserungen erforderlich, bevor das Verfahren ohne Probleme genutzt werden kann. Zusätzlich müssen auch unsere Bodenmodelle verbessert werden, damit die Wasserströmungen im Boden besser eingeschätzt werden können. Nur so wird es möglich sein, die Wasseraufnahme über die Wurzel im Lysimeter- und im Feldmaßstab zu messen.

x

Contents

List of Tables

List of Figures

List of Acronyms

BC	boundary condition
BTC	breakthrough curve
CDE	convection-dispersion equation
CV	coefficient of variation
D	drainage
DOY	day of the year
DR	water depletion rate
E	soil surface evaporation
EC	electrical conductivity
EC_b	bulk electrical conductivity
EC_w	solute electrical conductivity
ERT	electrical resistivity tomography
ET	evapotranspiration
ETc	potential crop evapotranspiration
ETo	reference evapotranspiration
FTL	fraction of total leaching
GPR	ground penetrating radar
HI	heterogeneity index
LS	loamy sand lysimeter
MIM	mobile-immobile model
MRI	magnetic resonance imaging
nDR	normalized water depletion rate
PVC	poly-vinyl chloride
RA	root architecture
RLD	root length density
RMSE	root mean squared error
RWU	root water uptake
S1, S2	silty lysimeter 1, silty lysimeter 2
SSDC	spatial solute distribution curve
STAL	scaled total amount leached
STM	stream tube model
Surf	leaching surface
TDR	time domain reflectometry
WC	water content
W-S	Waxman and Smits

List of Symbols

ρ_a	apparent resistivity
K_p	cell constant of the TDR probe
R^2	coefficient of determination
ξ_c	composite dielectric constant
z	depth, vertical coordinate (cm)
D	diameter
DI	direction vector
$Dist_{Ram}$	distance between primary root ramifications
Φ	electric potential
σ	electrical conductivity
Δl	elongation in Δt
ε	error level
W_ε	error weighting matrix
α, ζ	free parameters of the standard beta function
G	gravity vector
h	height
Z_C	impedance of the TDR device
v_{INIT}	initial root growth velocity
α	insertion angle
v	integral velocity (solute transport) / effective growth velocity (root architecture)
c_{grav}	intensity of gravitropism
u	local velocity (solute transport)
Nr_{Max}	maximal amount of primary roots intercepted by a rhizotube
L_{max}	maximal root length
J_s	normalized solute flux
$\varepsilon_{N/R}$	normal-reciprocal error
Nr_{Prim}	number of primary roots
ψ	objective function
ρ_∞	reflection coefficient at very long times
λ	regularization parameter (ERT inversion) / dispersion coefficient (solute transport)
R	resistance
W_s	smoothness operator
SLP	slope of the growth curve between t80% and t20%
j_s	source current density

t$_{50\%}$	time at which 50% of the final amount of primary roots is reached
θ	volumetric water content
ρ$_j$	voxel electrical resistivity
m	weight

Part I

General Introduction

Why is it so important to know how plants take up water from their environment? Why do we even care about soil moisture at all? The answers are not quite as simple as the questions. The unique role soil moisture plays in the environment originates from the fact that the soil is a thin, porous layer separating the atmosphere above from the hydrosphere below. Groundwater is recharged by seepage of water through the soil. Pollutants dissolved in this water, move through what we call the unsaturated or vadose zone. Soil moisture can be lost by evaporation to the atmosphere and indirectly through growing plants. The combined loss, called evapotranspiration, exerts a strong impact on the energy and water balance of the earth (Hillel, 1998). About 25 percent of incoming solar energy leaves the earths surface through evaporation (Lindsey, 2009), of which about 14% from land and 86% from water surfaces (Shiklomanov, 1993).

The exchange of water between soil and atmosphere is thus crucial for the partitioning of incoming radiation energy. As a consequence, soil moisture indirectly influences the air temperature (Koster et al., 2006). Climate predictions point out that the variability of the summer temperature in large parts of Europe will increase (Giorgi et al., 2004; Schar et al., 2004; Vidale et al., 2007). Seneviratne et al. (2006) showed that this variability is mainly due to feedbacks between the land surface and the atmosphere. Furthermore, they showed that land-atmosphere interactions might not only increase temperature variability, but also climate variability in general. A detailed knowledge of soil moisture redistribution is thus of major importance for our understanding of climatological changes and thus of global warming (Maxwell et al., 2008).

However, we don't need to look at the global scale to see the need for a good understanding of soil moisture redistribution and root water uptake. Soils are used for industrial and municipal purposes, for agriculture, for grassland and forestry. Leaching and run-off of plant nutrients from agricultural soils, for example, is a persistent problem of modern agriculture. A surplus of an applied compound occurs when not all the input is taken up by the crops and removed

by harvesting. In the EU, more than 95 % of the 7.1 million tonnes of nitrogen surplus is likely to contribute to leakage of nitrogen into waters (EEA, 2000). Contaminants in the soil are transported either in dissolved form or associated with particles (e.g. Vanclooster et al., 2005; Kanti Sen et al., 2006). In both cases, soil moisture content and soil structure can significantly modify the contaminant transfer, because they determine the water flow velocity (Padilla et al., 1999). Therefore, we need to know how the soil moisture distribution evolves in order to predict the leaching of contaminants or agrochemicals to groundwater reservoirs accurately. Root water uptake is known to affect the soil moisture distribution (Sharp et al., 1985; Katul et al., 1997; Coelho et al., 1999; Srayeddin et al., 2009), but its influence on solute transport is not yet very well understood.

In the context of water scarcity, access to fresh water and good water management are the key issues to ensure sustainable agricultural production. Only about 9000-14000 km³ (=6-9 10^{-3}% of the total amount of water on earth) of the worlds fresh water resources are economically available for human use. With 70% of the fresh-water consumption (about 95% for developing countries), agriculture is the biggest user of this water (FAO, 2010). Maximizing the use of water supplies can increase agricultural productivity enormously. Application of irrigation techniques can increase the yield up to 400% as compared to rainfed yields. In 2002, 18% of the cultivated land was under irrigation (WRI, 2005) and produced about 40% of the worlds' food. The food and agriculture organization (FAO) expects that over the next 30 years 70% of the gains in ceral production will come from irrigated land. However, poor irrigation practices can cause waterlogging and salinization. About 10 % of the world's irrigated land has been degraded because of these processes already (FAO, 2010). An improvement of the management of agricultural water thus becomes the key to the achievement of global food security (Pimentel et al., 1997). Therefore, local irrigation, where water is provided frequently and with small quantities to each plant, becomes increasingly popular. In order to optimize this system, the crops' water demand, root development and reaction to water stress have to be known.

It is therefore not surprising that the understanding of water flow processes taking place in the soil-plant-atmosphere continuum has been a popular research topic during the second half of the 20th and beginning of the 21st century. Furthermore, almost 40% of the publications containing 'root water uptake' or 'soil-root-interactions' in their title were published in the past 10 years (see Figure 1). It must of course be noted that the total number of scientific publications has also been growing steadily in recent decades and thus the increase might also (partly) be related to changing publication behaviour. Over the years, many root water uptake model approaches have been suggested at different scales and with varying objectives. Some studies described interesting experiments and then used them for model validation. For a comprehensive overview of existing root water uptake models, see Part VII of Hillel (1998).
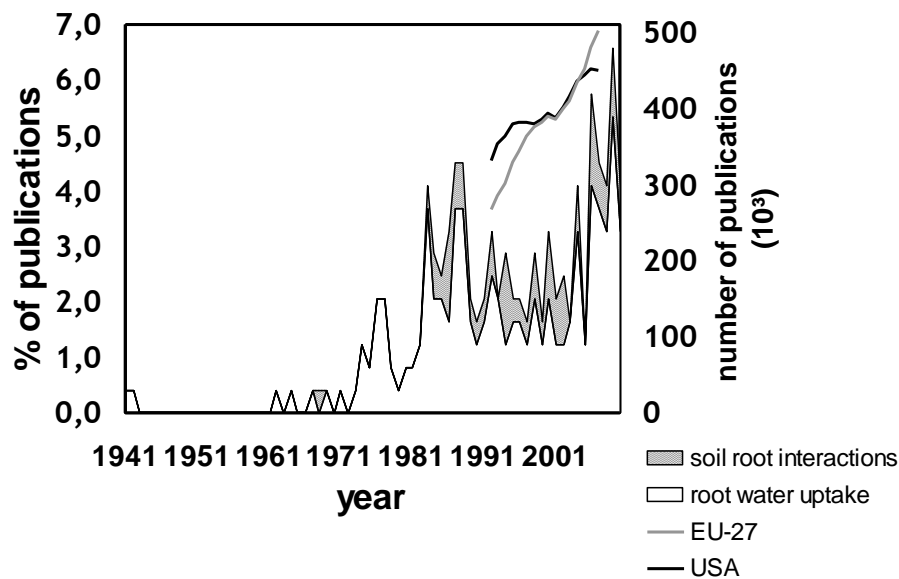
Figure 1. The percentage of publications with a title containing 'root water uptake' or 'soil-root interactions' (1940-2009) (Source: Web of knowledge, August 2010) and the overall trend of increasing publication numbers (1992-2007) (Haustein et al., 2009).

However, controversy still remains about the main factor controlling root water uptake, especially under non-uniform soil moisture distribution or intermediately wet soil. There are several reasons for this. Firstly, both soil and root system are highly dynamic and inextricably intertwined (Doussan et al., 2006). The representation of the soil-root continuum is scale-dependent (Jackson, 2000).

Water flow in this system at the single plant or field scale soon becomes a complex process. This motivated researchers to search for ways to decrease the problem's dimensionality. Secondly, root system architecture measurements remain time-consuming and expensive. Furthermore, only a few techniques can be used to follow root growth in a 'natural' environment without destroying parts of the root system and the soil matrix. We are in need of minimal-invase measurement techniques to image the root system and soil water content with high spatial and temporal resolution to validate existing models.

The main objective of this PhD was to improve our understanding on the effect of crops on water fluxes and solute transport in a natural soil. Firstly, we provided high-quality experimental data incorporating information on root architecture and soil characteristics and states under known boundary conditions. We designed a series of experiments with two large undisturbed soil monoliths. The experiments allowed us to explore the hydraulic and transport characteristics of the soil and the different effects of plant growth on water flow and solute transport. Secondly, we investigated the value of 3-D electrical resistivity tomography (ERT) in particular to measure soil moisture dynamics and solute transport continuously and non-invasively. The results of this PhD project are presented in three chapters, corresponding to published or submitted publications to international peer-reviewed journals. Until now, three research papers have emerged from this project focusing on (i) solute transport characteristics of two bare, undisturbed soils; (ii) 3-D measurement of soil water depletion in a cropped soil; (iii) measurement of root growth and root system architecture of barley in a natural soil.

Chapter 1 compares the solute transport in two undisturbed soil columns measured with ERT, Time Domain Reflectrometry (TDR) and effluent conductivity during a step tracer experiment. At the column scale the transport in the loamy-sand was essentially non-preferential in behavior, while at the scale of voxels the transport was revealed to be preferential. The transport in the silty soil was considerably more heterogeneous.

Chapter 2 explores the potential of ERT to measure soil water depletion in an undisturbed soil monolith cropped with summer barley. Our analysis sustained the value of ERT as a tool to monitor and quantify water contents and water content changes in the soil, as long as the root biomass does not influence the observed resistivity. This is shown using a global water mass balance and a local validation using TDR probes.

Chapter 3 deals with the estimation of a root architecture (RA) model for summer barley in both lysimeters using the minirhizotron measurements. The information content of the minirhizotron measurements was examined and growth curves of the number of roots at a certain depth were used to optimize the RA model. The simplest model was acceptable, but to obtain satisfying results, soil density effects and the incorporation of 'reiteration' of root tips should be included.

Since these chapters are dealing with very different aspects of the central research question, each chapter has its own objectives, introduction and description of the materials and methods. A general overview of the experimental set-up and the experiments conducted in the lysimeter facility can be found in Part II: general set-up.

Part II

Experimental Set-Up

Lysimeter extraction and properties

All experiments were conducted on two soil monoliths, which were sampled using large PVC columns with a height of 150 cm, an inner diameter of 116 cm and a wall thickness of 2 cm. The PVC column was gently driven into the soil using the hydraulic shovel of an excavator. In order to reduce friction, the soil around the column was gradually excavated and the bottom of the PVC column was sharpened. When the column was completely filled with soil, a steel plate was driven horizontally under the monolith to isolate it. The column was transported to the lysimeter facility of the Forschungszentrum Jülich, where it was placed on a scale (Bizerba, Balingen, Germany), after a suction plate was mounted to the bottom of the column. Due to the placement of the suction plate and some space left between the top of the PVC column and the soil surface, the soil was 142 cm deep in lysimeter 1 (S1) and 139 cm in lysimeter 2 (S2). The upper boundary of the lysimeter was aligned with the soil surface above the lysimeter basement. The column was covered from rainfall by a steel cover or by a greenhouse construction, depending on the experimental phase. Figure 2 shows an overview of the lysimeter extraction, transportation and installation.
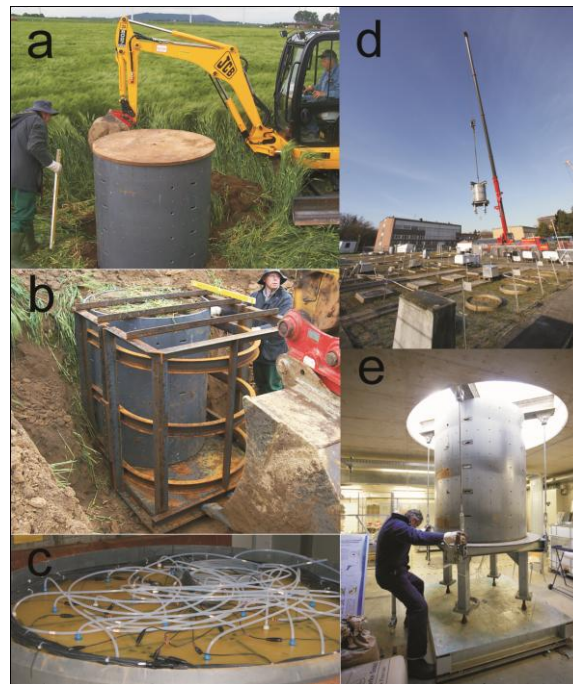
Figure 2. (a, b) Soil excavation, (c) suction plate installation and (d,e) transportation to the lysimeter facility in Jülich.

The monoliths were taken from intensively used arable land near Merzenhausen. The field is located on a weakly inclined and structured, high terrace of the Rur bassin. The markedly profound loess from fluviatil origin, which is the parent material for this soil, is dated to the Pleistocen/Holocen, whereas the original eolian sediment has been transported through the river water. The soil was classified as an orthic Luvisol (FAO/ISRIC/ISSS, 1998). Four soil horizons were identified: A_p (0-40 cm), B_t (41-70 cm), B_{v1} (71-100 cm) and B_{v2} (>100cm). The soil properties are given in Table 1. With a content of approximately 80 %, silt is the main textural fraction, whereby the coarse silt dominates with approximately 50 %. The clay content is about 20 % and the total sand content is lower than ≤ 5 % in all horizons. The A_p-horizon is characterized as a clayey silt, the B_t-horizon as a highly clayey silt, underlayed by a moderately clayey silt in the B_v-horizon. The homogeneity in all horizons is confirmed by the nearly constant soil bulk densities. In the B_t-horizon coarse prismatic structures and redbrown clay cutanes on the surfaces of the aggregates indicate clay enrichment (Weihermueller, 2005). Earthworm burrows are abundant down to depths of more than 150 cm. However, few direct connections to the soil surface exist because of frequent ploughing (Burkhardt et al., 2005). Root channels are generally <10 mm in diameter and were found above a depth of 1.2 m. The two excavated monoliths are referred to as lysimeter 1 (S1) and lysimeter 2 (S2).

Table 1. Description of the soil horizons in the lysimeters. Textures (Burkhardt et al., 2005), K_s (Schmidt-Eisenlohr, 2001), bulk density (BD) and porosity (Weihermueller, 2005).

Horizon	Depth (cm)	Sand (%)	Silt (%)	Clay (%)	BD (g.cm^{-3})	K_s (log$_{10}$[cm.day^{-1}])	Porosity (%)
A_p	0 - 40	3	79	18	1.48	1.89	43.5
B_t	41 - 70	1	76	23	1.54	1.4	41.7
B_{v1}	71 - 100	1	79	20	1.54	1.4	41.7
B_{v2}	>100	2	84	14	1.56	1.35	40.9

Equipment

The bottom of both lysimeters was be kept at known, constant suctions up to a maximum of -500 hPa by a polyamid-membrane suction plate (ecoTech GmbH, Bonn, Germany) and a vacuum pump (UMS, Munich, Germany). We used a drip tape configuration (T-Tape by John Deere, Mannheim, Germany) containing 16 drippers for experiments with irrigation. The irrigation fluid (tap water or $CaCl_2$-solution) always had the ambient temperature of the lysimeter basement (10 ± 4°C) and a known, constant electrical conductivity (EC) (0.590 and 2.63 mS.cm^{-1} respectively). 212 Electrodes were inserted at the side of the soil column extending 1.5 cm into the soil. The electrodes at the side of the column were arranged in six horizontal rings of 32 equidistantly distributed electrodes (horizontal spacing = 11.8 cm). Four vertical transects of five electrodes were added in between these circles (see Figure 3). The electrodes were connected with relay boxes to a six channel RESECS prototype (GeoServe, Kiel, Germany) to conduct ERT measurements. Horizontal TDR probes were inserted diametrically to each other in the column to measure water content and bulk electrical conductivity. The probes were arranged in four vertical transects of five probes at different depths. We used a three-rod design (Heimovaara, 1993) with a rod length of 19 cm, a rod spacing of 2.6 cm and a rod spacing/diameter-ratio of 13:2. A TDR100 system and SDMX50 multiplexers (Campbell Scientific, Utah, USA) were used to conduct the TDR measurements. A CR10X logger (Campbell Scientific, Utah, USA) logged the data at 1h intervals. In order to avoid current losses through the TDR probes, all TDR probes were galvanically disconnected from the multiplexers during ERT measurements using relays (Koestel et al., 2008). A switchbox was used to trigger the relays automatically by using a RESECS signal. In addition to the TDR probes, ten tensiometers were inserted in each soil column in two diametrical transects to monitor the matric potential of the soil as well as six platinum resistance thermometers (PT100) to be able to correct for the effect of temperature changes on electrical resistivity. The tensiometer and PT100 sensor data were logged with a DL2e data logger. The electrical conductivity of the effluent was measured with a Cond i325 conductivity meter (WTW,

Weilheim, Germany). Finally, we equipped the lysimeters with a vertical transect of four horizontally installed minirhizotron tubes at -22.5/19.5, -47.5/44.5, -72.5/69.5 and -122.5/119.5 cm depth for S1/S2 respectively. The tubes were made of plexiglass, were 60 cm long and had a diameter of 5.72 cm. A BTC2 video microscope (Bartz Technology Corporation, Carpinteria, CA, USA) was used to monitor root length density (RLD) and root growth on the outer walls of the tubes.
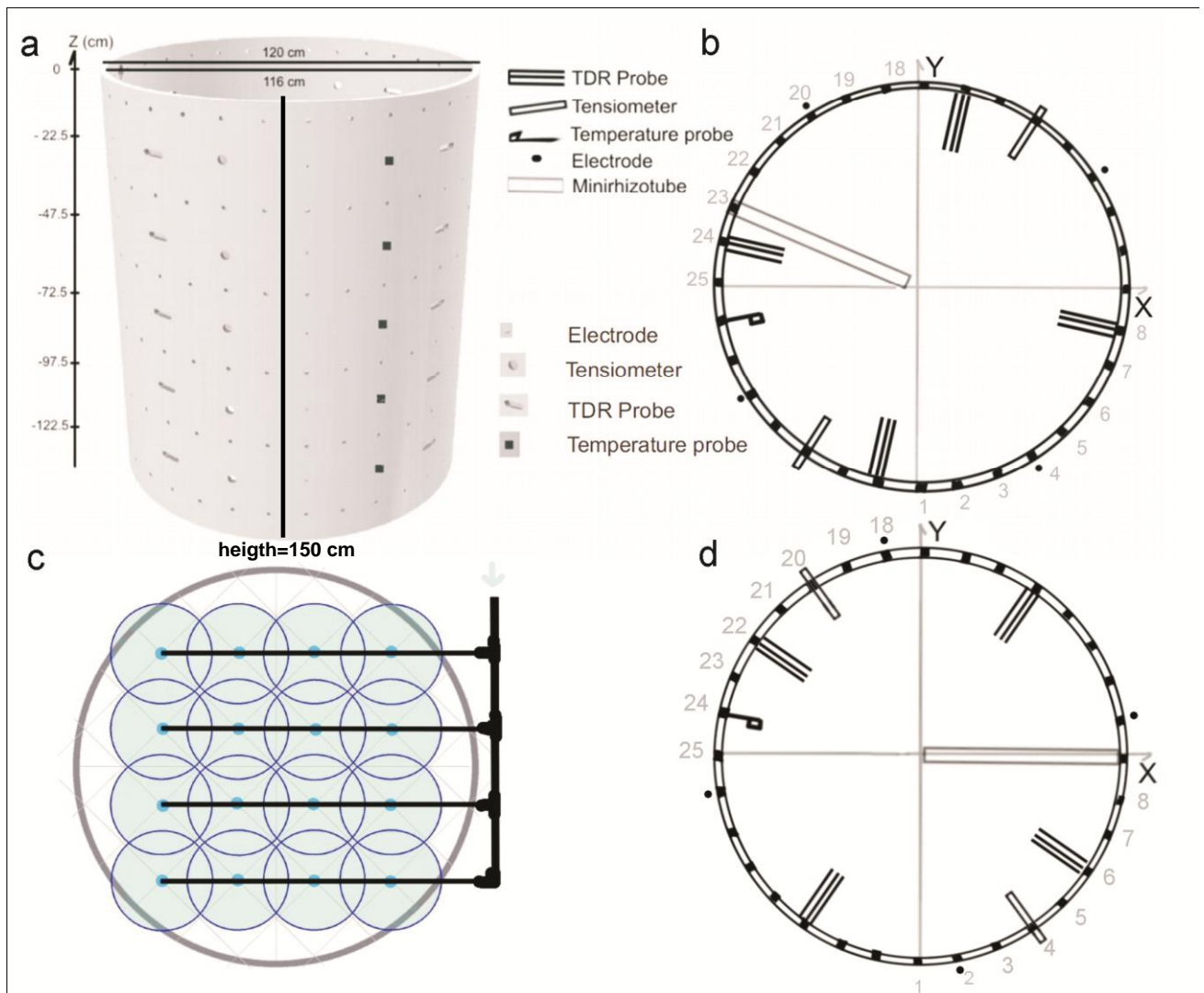
Figure 3. Experimental set-up. (a) 3-D representation of the lysimeter with its equipment; (b,d) horizontal scheme of the equipment of lysimeters S1 and S2 respectively; (c) irrigation with drippers.

Experiments

We conducted a series of consecutive experiments to elucidate the role of root water uptake on the soil water flow regime and solute transport. Since these are complex processes in which many factors have an influence on the outcome, the experiments where designed to separate the different factors and assess there influence. Through comparison of these experiments we aimed at getting a better grip on the many facets of soil water flow and solute transport in a cropped soil. Figure 4 shows an overview of the consecutive experiments conducted in the lysimeters. Basically, three big groups can be separated: bare soil experiments, cropped soil experiments and bare soil experiments with remaining dead roots.

Bare soil experiments

We conducted two experiments with bare soil columns: a $CaCl_2$-tracer step experiment (see Figure 4-a [1], -b [1]) to assess the occurrence of preferential flow and a drainage experiment (see Figure 4-a [2], -b [2]) to be able to infer in-situ hydraulic properties of the bare soil. The results of the tracer step experiment are shown and discussed in Part III: Results, Chapter 1, whereas the results of the drainage experiment where analyzed by V. Couvreur (UCL, Belgium) as a part of his MsC thesis. After these treatments, the lysimeters were flushed with tap water. S1 was irrigated until half of the tracer was flushed out, whereas S2 is flushed entirely. After that, both lysimeters were draining until the cropped soil experiments could start.

Cropped soil

We sew summer barley (*Hordeum vulgare L.*) at the same day in both lysimeters. However, the initial water content was somewhat higher in S2 than in S1 because the foregoing irrigation phase lasted longer. During the entire growing season, no water was added. The irrigation system was shut down and the lysimeters were covered by a greenhouse construction. During this period, changes in water content were entirely related to root water uptake and the resulting water fluxes in the soil (see Figure 4-b [4]). The results of the cropped soil experiment of S2 are shown and discussed in Part III: Results, Chapter 2.

When the barley plants were mature, we harvested and started irrigating again in order to flush the remaining tracer from S1 and to bring both soil columns back to steady-state water flow conditions. The ensemble of the negative tracer step interrupted by the barley growing season in S1 gives us information on the influence of root water uptake on the breakthrough of solutes in the soil (see Figure 4-a [4]). However, the analysis of the latter experiment is not yet finished and is not included in this dissertation.

Bare soil with remaining dead roots

Again, we applied a different treatment to both lysimeters. On S1, we repeated a $CaCl_2$-tracer step experiment interrupted by a pause without irrigation when the tracer was flushed out of half the column (see Figure 4-a [5]). The length of the pause was similar to the length of the barley growing season. This experiment was conducted in order to see if there was an important difference between the breakthrough with evapotranspiration and the one without. The data have not been analyzed yet and are therefore not included in this dissertation. On S2, we repeated exactly the same tracer step experiment as on the bare soil (see Figure 4-b [6]). The aim of this experiment was to assess if the physical presence of roots had changed the solute transport behavior of the soil. The data have not been analyzed yet and are therefore not included in this dissertation.
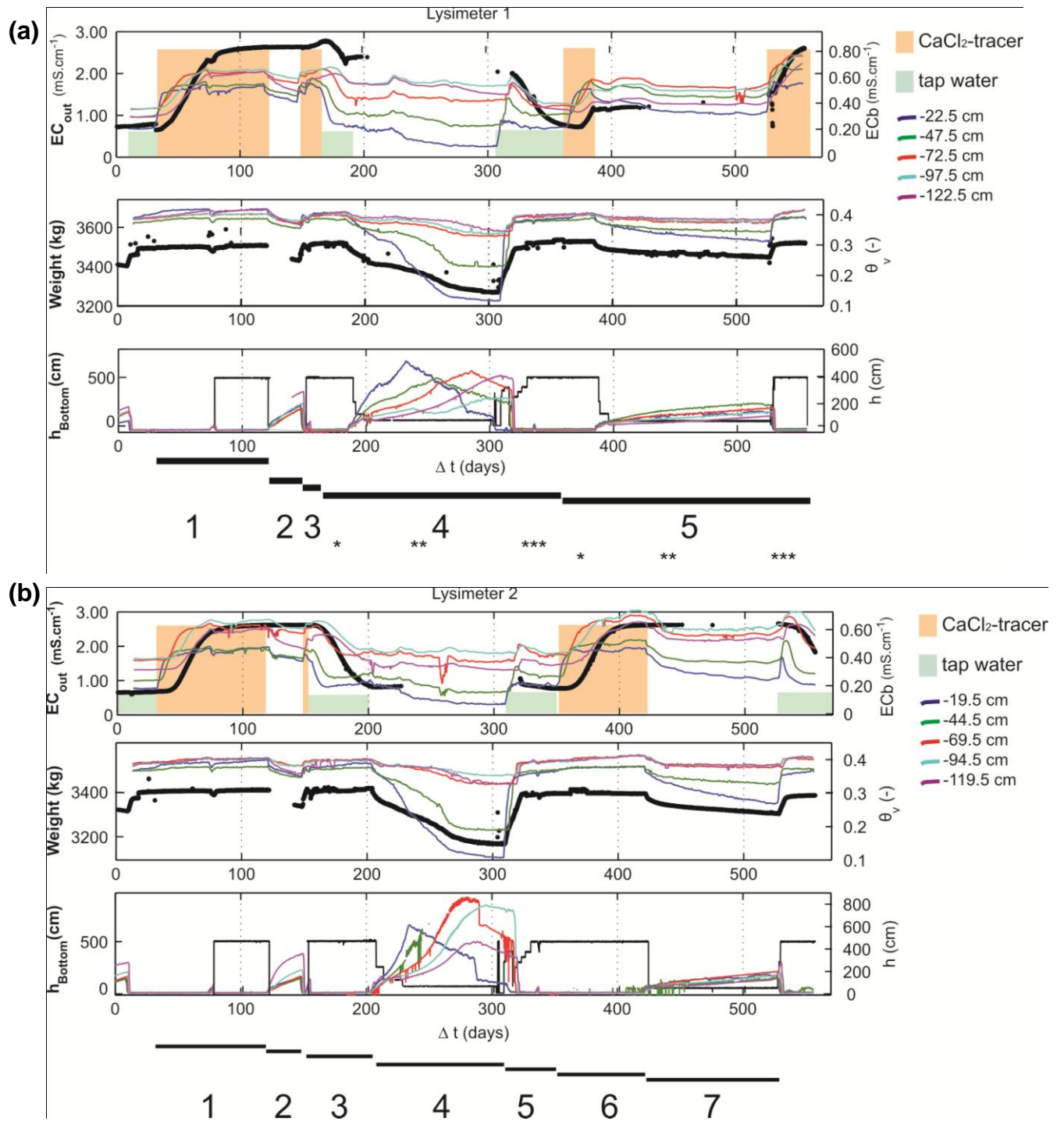
Figure 4. Overview of all lysimeter experiments showing TDR, tensiometer, effluent conductivity, bottom suction and weight measurements. (a) Lysimeter 1 (S1): [1] CaCl2-tracer step experiment; [2] drainage; [3] CaCl2-tracer infiltration; [4] tap water breakthrough curve with root water uptake consisting of [*] constant irrigation with tap water, [**] no irrigation, [***] constant irrigation with tap water; [5] CaCl2-tracer breakthrough without root water uptake consisting of [*] constant irrigation with tracer, [**] no irrigation, [***] constant irrigation with tracer.

Part III
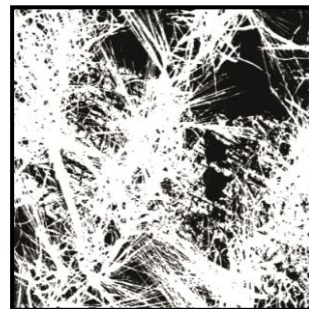
Results
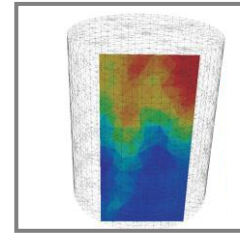
Comparison of Heterogeneous Transport Processes Observed with Electrical Resistivity Tomography in Two Soils[1]

Abstract.

Preferential flow in soils can manifest itself in several ways. To illustrate this, we analysed the solute transport during a step tracer experiment in two soils expected to differ in their governing transport processes: a loamy sand and a silty soil. By combining Electrical Resistivity Tomography (ERT), Time Domain Reflectrometry (TDR) and effluent measurements we observed different preferential flow phenomena. The transport process was characterized using voxel and column scale effective CDE parameters, local velocities and leaching surfaces. At the column scale, transport in the loamy-sand was dominated by a homogeneous convective-dispersive transport behaviour, but at the scale of the voxel preferential transport was observed. The transport in the silty soil was considerably more heterogeneous. Preferential flow was identified using ERT, voxel and column-scale effective CDE parameters, local velocities and leaching surfaces. In these soils, a clear influence of the soil layering on the solute transport was observed.

---

[1] Adapted from: Garré, S., Koestel, J., Günther, T., Javaux, M., Vanderborght, J., Vereecken, H. 2010. Comparison of Heterogeneous Transport Processes Observed with Electrical Resistivity Tomography in Two Soils. Vadose Zone J 9: 336-349.

1. Introduction

Clothier et al. (2008) defined preferential flow as 'all phenomena where water and solute move along certain pathways, while bypassing a fraction of the porous matrix'. Based on literature, four different preferential flow phenomena can be identified: (i) The most obvious phenomenon linked to preferential flow is, that solute concentrations in a plane perpendicular to the mean water flow direction are not homogeneous. This is often visualized with dye tracer studies (eg Flury et al., 1994; Flury et al., 2003; Burkhardt et al., 2005). The heterogeneity in solute concentrations has important consequences for reactive transport when chemical reactions depend in a non-linear way on local concentrations (Kasteel et al., 2002; Javaux et al., 2006; Vanderborght et al., 2006). The lack of solute mixing and its effect on reactive transport is currently a major research topic in reactive groundwater transport (Cirpka et al., 2008). (ii) A second way preferential flow may manifest itself is by a larger spreading of the tracer front or breakthrough curve compared to a uniform flow domain. The spreading is either defined by the second centralized spatial moment (Freyberg, 1986) of a plume or second centralized temporal moment (Aris, 1958; Kreft et al., 1978) of a breakthrough curve. Water flow in regions that bypass a part of the soil matrix leads to a rapid downward transport whereas solutes that enter into bypassed regions move considerably slower. This causes an increased spreading (eg Adams et al., 1992; Salamon et al., 2007; Vanderborght et al., 2007). (iii) A third preferential flow appearance is a more rapid increase of the plume spreading with time or breakthrough spreading with depth than is predicted by a convective-dispersive process. In a stochastic-convective process, the spreading increases linearly with time or depth (Jury et al., 1990). (iv) Finally, the manifestation to which preferential flow and transport are typically related is an early breakthrough with high peak concentrations and a long tailing of concentrations that decline very slowly. In this case, the breakthrough is much earlier than would be expected when flow takes place uniformly in the entire pore space or volume. Fast leaching may result in insufficient time for chemical or biological degradation of contaminants in the

root zone (eg Edwards et al., 1992). These contaminants then leach to the groundwater, where it may take very long before they are degraded (Stagnitti et al., 2003). It must be noted that the above mentioned preferential flow manifestations do not necessarily occur simultaneously. It depends on the type of preferential flow which phenomena or characteristics are present.

Different approaches have been used in the literature to quantify the different forms of appearance of preferential transport. The first type of preferential flow (i) caused by incomplete mixing, can be characterized by entropy measures such as the dilution index (Kitanidis, 1994), determination of spatial covariances of concentrations or transport parameters (Koestel et al., 2009) that characterize locally observed transport, or leaching surfaces (De Rooij et al., 2002). The second (ii) and third appearances (iii) may be characterized by dispersion coefficients of laterally averaged concentrations or by spatial covariances of local advection velocities. Manifestation four (iv) may be characterized by parameters of mobile-immobile model (MIM) or dual permeability models which consider rapid transport in a part of the pore volume and a rate limited solute mass exchange between different pore regions. Depending on how preferential flow manifests itself, different modelling approaches may be required to describe it. Models that may be used are the convection-dispersion model (CDE), the stream tube model (STM), the MIM and the stochastic continuum model (see Feyen et al., 1998 for an overview). Using a CDE model to describe preferential flow processes may sound controversial. However, if preferential flow is defined more broadly than pure macropore flow with an early peak breakthrough and a long tailing, it may well be that a CDE model can be used to describe a transport process in which water and solutes pass a fraction of the soil matrix.

Different experimental methods and setups have been developed and used to characterize the different forms of preferential flow. Dye tracer experiments mainly focussed on non-homogeneous tracer distributions (Gjettermann et al., 1997; Burkhardt et al., 2005; Sander et al., 2007). Tracer experiments in which

the breakthrough is measured in the effluent of a (large) column (Schoen et al., 1999 among others) or in a field drain (Jaynes et al., 2001 among others) focussed on rapid peak breakthroughs, whereas tracer experiments in which breakthrough is monitored at several depths investigated on the increase of the breakthrough spreading with depth. A major problem in preferential flow and transport research is the impossibility to extrapolate one type of appearance of preferential flow to another. For instance, spatial variations of local concentrations do not necessarily correspond to a non-Fickian dispersion process or early peak breakthrough. Neither does an early arrival of the peak concentration in combination with a long tailing of a breakthrough curve, which is observed, for instance, in columns packed with micro-porous glass beads (Desmedt et al., 1984), necessarily correspond to a spatial variation of macroscopically averaged concentrations. Therefore, in order to obtain a more comprehensive insight, experimental methods that enable simultaneous observation of different appearances of preferential flow and transport are needed. Examples of such methods are spatial discretized sampling of water and solute fluxes (Quisenberry et al., 1994; Stagnitti et al., 1999; De Rooij et al., 2000; De Rooij et al., 2002; De Rooij et al., 2006; Bloem et al., 2009) or measuring in situ concentration breakthrough curves at several locations with suction cups or TDR. The problem that remains with these methods is that the full 3-D structure of flow and transport process cannot be observed. This structure can be observed with non-invasive 3-D imaging techniques such as X-ray tomography (eg Mooney et al., 2008), magnetic resonance imaging (MRI) at the small soil column scale (Hoffman et al., 1996; Oswald et al., 1997; Herrmann et al., 2002) or geo-electrical methods like electrical resistivity tomography (ERT) at the larger column (Binley et al., 1996; Olsen et al., 1999; Slater et al., 2002; Koestel et al., 2008) or field plot scale (al Hagrey et al., 1999; French et al., 2002; Looms et al., 2008).

The objective of this paper is to characterize the different forms in which preferential transport may appear in two different soils: a loamy sand soil, which was investigated by Koestel et al. (2008) and a silty soil. Based on their textural

and structural differences, solute transport is expected to be different in these two soils. We used electrical resistivity tomography combined with TDR and effluent concentration measurements to observe solute transport and to map the spatial and temporal variation of solute (resident) concentrations. From breakthrough curves which are observed at different scales, the spatial variability of the transport process and scale dependence of the solute spreading are inferred using effective transport model parameters. In addition, we explore the use of leaching surfaces to characterize the underlying transport processes within the two soils.

2. Materials and methods

2.1 Soils

Transport experiments were conducted on three different soil monoliths, which were sampled using large PVC columns with a height of 150 cm, an inner diameter of 116 cm and a wall thickness of 2 cm. The soils were classified as a gleyic Cambisol (FAO/ISRIC/ISSS, 1998) and an orthic Luvisol. One monolith was taken from an agricultural field site near Kaldenkirchen (Germany) and the soil at this site was classified as a gleyic Cambisol. The soil parent material consists of Aeolian sands. At about 33 cm depth a sharp boundary between the plough layer and the subsoil was observed. This boundary shows an undulation oriented perpendicular to the plough direction. The bottom of the plough horizon was compacted which indicates the presence of a plough pan. This loamy sand lysimeter will be referred to with LS.

Two monoliths were taken from intensively used arable land near Merzenhausen, where the soil was classified as an orthic Luvisol. These are the lysimeters presented in Part II: Experimental set-up. The soil parent material at this site is Löss. Earthworm burrows are abundant down to more than 150 cm depth, although few direct connections to the soil surface exist because of frequent ploughing (Burkhardt et al., 2005). Burkhardt et al. (2005) estimated the number of earthworm burrows and root channels for four horizontal planes

in the subsoil to be about 15 and 350 .10^{-4} cm^{-2}, respectively. These two columns will be called S1 and S2.
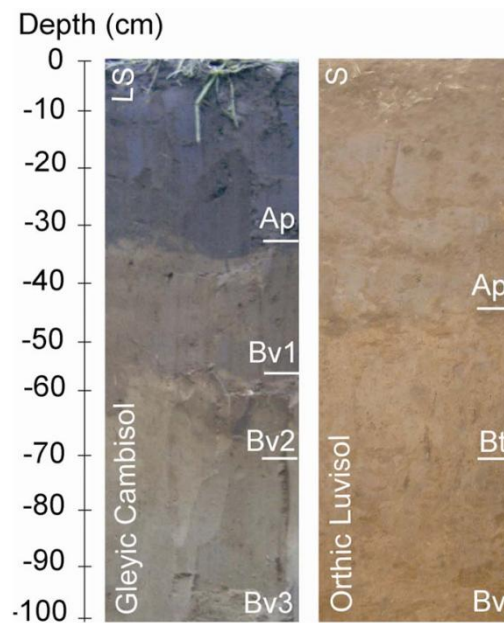
Figure 5. (left) Soil profile of the loamy sand soil (LS) at the Kaldenkirchen field site. (right) Soil profile of the silty soil (S1/S2) at the Merzenhausen field site.

2.2 Lysimeter setup

The bottom boundary of the LS lysimeter was a seepage face through which water could leave the saturated part of the flow domain. This means that there is no flux as long as the local pressure head at the bottom of the soil profile is negative. As soon as the bottom of the profile becomes saturated, a flux is assumed. This type of boundary condition very often applies to finite lysimeters that are allowed to drain under gravity. The bottom of both the S1 and S2 lysimeters was kept at -500 hPa by a polyamid-membrane suction plate (ecoTech GmbH, Bonn, Germany) and a vacuum pump (UMS, Munich, Germany). The suction plate i) avoids the formation of a saturated layer at the capillary fringe of the lysimeter which would affect the tracer transport and (ii) accelerates the tracer movement in the S soil which was expected to be slower than in the LS. It is our aim to show how different transport patterns and phenomena can be distinguished and visualized using ERT rather than to compare the transport properties of the two soils under identical boundary conditions.

In all three lysimeters, 212 Electrodes were inserted at the side of the column extending 1.5 cm into the soil. The electrodes at the side of the column were arranged in six horizontal rings of 32 equidistantly distributed electrodes. Four vertical transects of five electrodes were added in between these circles (see Figure 3). Details about the electrode arrangement are documented in Koestel et al. (2008). The electrodes were connected with relay boxes to a six channel RESECS prototype (GeoServe, Kiel, Germany) to conduct ERT measurements.

Horizontal TDR probes were inserted diametrically to each other in the column to measure water content and bulk electrical conductivity. The LS lysimeter counted ten probes, whereas S1 and S2 had 20, arranged in vertical transects of five probes. We used a three-rod design (Heimovaara, 1993) with a rod length of 19 cm, a rod spacing of 2.6 cm and a rod spacing/diameter-ratio of 13:2. A TDR100 system and SDMX50 multiplexers (Campbell Scientific, Utah, USA) were used to conduct the TDR measurements. A CR10X logger (Campbell Scientific, Utah, USA) logged the data at 1h intervals. In order to avoid current losses through the TDR probes, all TDR probes were galvanically disconnected from the multiplexers during ERT measurements using relays (Koestel et al., 2008). A switchbox was used to trigger the relays automatically by using a RESECS signal. In addition to the TDR probes, ten tensiometers were inserted in each soil column in two diametrical transects to monitor the matric potential of the soil as well as six platinum resistance thermometers (PT100) to be able to correct for the effect of temperature changes on electrical resistivity. The tensiometer and PT100 sensor data were logged with a DL2e data logger. The electrical conductivity of the effluent was measured with a Cond i325 conductivity meter (WTW, Weilheim, Germany). See Figure 3 for an overview of the experimental set-up.

2.3 Experimental design of tracer experiments

The soil columns were placed in the lysimeter facility of the Forschungszentrum Jülich and were kept at a temperature of 10°C (± 4°C). Steady-state flow conditions were imposed with tap water on all soil columns using a constant

irrigation of 1.5 cm.day^{-1}. These flow conditions were necessary to enable quantitative interpretation of the ERT images. The irrigation rate is a compromise between feasibility (due to technical (homogeneous irrigation) and temporal constraints (fast tracer displacement)) and approximately natural boundary condition (BC). Vanderborght et al. (2000a, 2000b) showed that experiments run under high steady flow rates, but under a flow rate that is still relevant for rainfall rates, are still relevant for transport processes under transient boundary conditions. The LS lysimeter was irrigated with a reservoir with 484 dripper needles. The S lysimeters were equipped with a drip tape configuration (T-Tape by John Deere Water, Mannheim, Germany) containing sixteen individual drippers. The irrigation water had the ambient temperature of the lysimeter basement. The soil columns were at steady state when the experiments started with a volumetric water content varying with depth between 0.19 and 0.29 for the LS and between 0.30 and 0.43 for the S (see Table 2).

Table 2. Average volumetric water content (WC) during the experiment measured with TDR at five depths in the lysimeters. LS= loamy sand lysimeter, S1= silty lysimeter 1, S2= silty lysimeter 2.

LS		S1		S2	
Depth (cm)	WC (-)	Depth (cm)	WC (-)	Depth (cm)	WC (-)
-17.5	0.25	-22.5	0.43	-19.5	0.39
-42.5	0.19	-47.5	0.4	-44.5	0.38
-67.5	0.19	-72.5	0.4	-69.5	0.4
-92.5	0.19	-97.5	0.39	-94.5	0.4
-117.5	0.3	-122.5	0.4	-199.5	0.4

After steady-state conditions were obtained for water flow as well as solute concentration, a CaCl$_2$-tracer step was applied until the tracer concentration in the effluent remained constant and was equal to the input tracer concentrations. This experimental design allows the determination of solute tracer concentrations directly from imaged bulk electrical conductivity measured with ERT as shown by Koestel et al. (2008). We adjusted the temperature corrected tap water background conductivity to 503 µS.cm^{-1} for the LS column and to 590 µS.cm^{-1} for the S columns using CaCl$_2$. The tracer conductivities were 2530

µS.cm^{-1} and 2630 µS.cm^{-1} respectively. The concentrations in the effluent were equal to the input concentrations after one month and two months of tracer application in the LS and S soil, respectively. Figure 6 shows an overview of the boundary conditions.
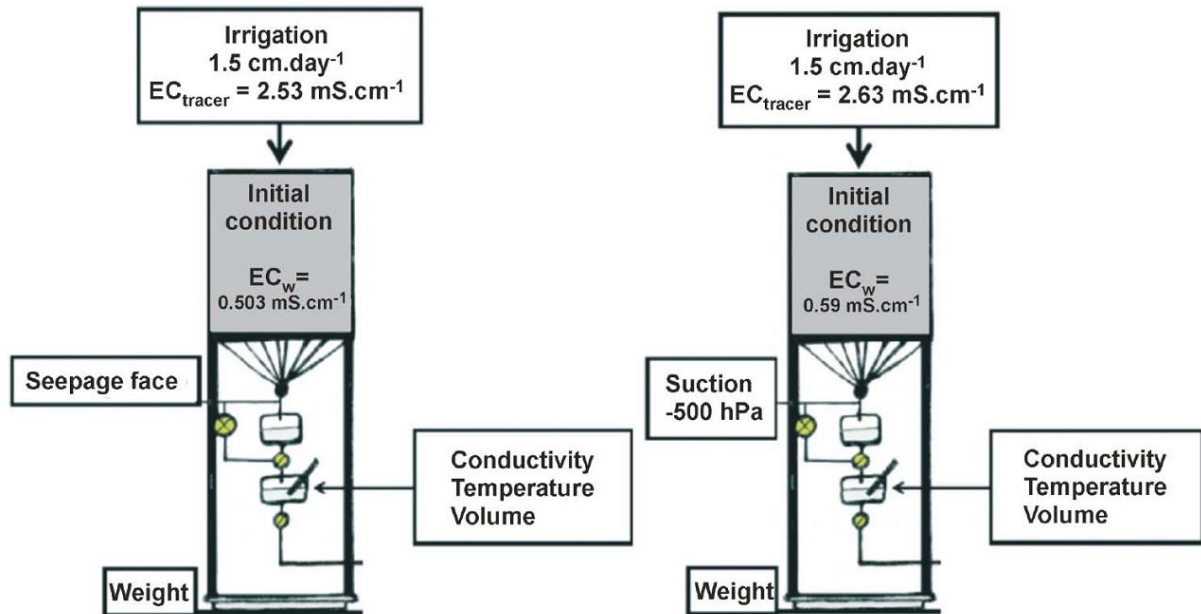
Figure 6. (left) Boundary conditions for the loamy-sand soil (LS). (right) Boundary conditions for the silty soil (S1 and S2).

2.4 Time-lapse electrical resistivity tomography (ERT)

Forward problem and inversion algorithm

We used a 3-D inversion of the ERT data to image changes in soil bulk electrical conductivity (EC$_b$). A 'skip one' dipole-dipole scheme was used as described in Slater and Sandberg (2000). Half of the measurements were run in a reciprocal mode in order to assess data quality (LaBrecque et al., 1996; Koestel et al., 2008). Specifications of the measurement scheme can be found in Koestel et al. (2008). For all lysimeters, a finite element method was used to solve the forward problem, which was formulated as the Poisson equation:

$$\nabla.(\sigma\nabla\phi) - \nabla.j_s = 0, \qquad\qquad (1)$$

where σ is the electrical conductivity, Φ the electric potential and j_s the source current density. No-flow boundary conditions were applied on all boundaries.

The inversion was carried out using an error-weighted, smoothness constrained Occam type algorithm. This means that the smoothest distribution of resistivities was searched to fit the data to a specified error level (ε_i). Given a set of N measurements of four-electrode resistance (R_i, i=1,2,…,N), minimization of the objective function (ψ) given by

$$\Psi = \left\| \mathbf{W}_\varepsilon \left[\mathbf{d} - f(\mathbf{m}) \right] \right\|_2^2 + \lambda \left\| \mathbf{W}_s (\mathbf{m} - m_0) \right\|_2^2 , \qquad (2)$$

produces an image of M voxel electrical resistivities (ρ_j, j=1,2, …,M). Here, *d* is the data vector, given by

$$d_i\text{=-log}(\rho_{ai}), \qquad i=1,2,…,N \qquad (3)$$

where $\rho_{a,i}$ is the ith apparent resistivity. The parameters of the inversion, m, are given by

$$m_j\text{=-log}(\rho_j), \qquad j=1,2,…,M \qquad (4)$$

f(m) is the forward model for the model vector (m); m_0 is the starting or reference model; W_ε is an error weighting matrix (see Table 3 for the definition); W_s is a smoothness operator calculated from the discretized first or second derivative of m; λ is a regularization parameter which determines the amount of smoothing imposed on m during the inversion (see Table 3). For further details we refer to Kemna (2000) and Günther et al. (2006).

As the minimization of the objective function is done using the Tikhonov approach, both the minimization of ψ and the adjustment of λ are intimately intertwined (Kemna, 2000). If the optimum value of λ is found using a univariate

search, the minimization procedure finds the value of λ fitting the data to the desired target misfit. This implies that the smoothness of the final inversion result is affected by the error estimates (ε_i). Therefore, a good estimation of the real data error is important.

ERT Data error analysis

As suggested by Koestel at al. (2009), we assumed that the data error could be approximated using a Gaussian error model which comprises an absolute resistance error component (a, Ω), and a relative resistance error component (b, -). These two components were then used in the inversion algorithm to calculate the error (ε_i) of each single data point d_i as follows:

$$\varepsilon_i = \frac{a}{R_i} + b.$$
(5)

We applied the approach proposed by Koestel et al. (2008) and used the normal-reciprocal error ($\varepsilon_{N/R}$) as a starting and reference point for the parameterization of Gaussian error model. This approach considers the error model being spatially and temporally constant, in order to reduce the degrees of freedom in the error estimation.

Koestel et al. (2008) showed that the model for the normal-reciprocal error is spatially variable, not only because of varying solute concentration but also because of varying water content. For the measurements of the LS soil, the mean of the error model parameter a was found to be 0.009 Ω (maximum 0.031 Ω) whereas the mean of parameter b was 0.5 % (maximum 1.1 %). For the S soil the mean of a was 0.0041 Ω (maximum 0.0072 Ω) whereas the mean of b was 1.9 % (maximum 3.3 %). We discarded all data points which had an $\varepsilon_{N/R}$ larger than the five-fold of the fitted error model in one or more of the timeframes in order to maintain a similar sensitivity distribution throughout the experiment.

Table 3. Overview of the inversion parameters and methodology for the 2 different codes used in this chapter. †DOF = degrees of freedom.

	Gleyic Cambisol (LS), Code A. Binley	**Orthic Luvisol (S1 and S2),** Code BERT T. Günther
	MEASUREMENTS	
Measurement scheme	skip one dipole-dipole	
Measured combinations	46260	27077
Length timeframe	8h 23min	5h 50min
Frequency	1 frame/day	2 frames/day
Vertical dipole length	25 cm	
Horizontal dipole length	22.8 cm	
	FORWARD PROBLEM	
Numerical calculation of the electric field	finite element	finite element
Forward mesh	structured triangular prism mesh	unstructured tetrahedral mesh
Forward mesh resolution	edge length ca. 6 cm	variable
DOF† of forward mesh	8472 nodes	33365 nodes
DOF† of primary mesh	-	125420 nodes
More information	Binley et al. (1996)	Günther et al. (2006)
	INVERSION	
Meshes	dual grid approach	triple grid approach with singularity removal
Objective function minimization	Gauss-Newton Minimization	Gauss-Newton Minimization
	Data functional	
Data vector	$d_i = -\log(\rho_{a,i})$	$d_i = \log(\rho_{a,i})$
Data weighting matrix	$W_\varepsilon = \mathrm{diag}[1/\varepsilon_1,\dots,1/\varepsilon_N]$	$W_\varepsilon = \mathrm{diag}[1/\log(1+\varepsilon_i)]$
	Model functional	
Parameters of the inversion	$m_j = -\log(\rho_j)$	$m_j = \log(\rho_j)$
Reference model	none: $m_0 = [0\dots0]$	timelapse: $m_0 = m_{initial}$
Smoothness operator	discretized 2nd derivative	discretized 1st derivative
Regularization parameter	univariate line search (as in Labrecque, 1996)	constant lambda
DOF† of parameter mesh	2453 elements	20434 elements

2.5 Time-domain reflectometry (TDR)

Topp's equation (Topp, 1980) was used to relate the volumetric water content (WC) of the soil columns to the composite dielectric constant (ξ_c):

$$WC = -5.3.10^{-2} + (2.92.10^{-2})\xi_c - (5.5.10^{-4})\xi_c^2 + (4.3.10^{-6})\xi_c^3 . \qquad (6)$$

This calibration curve proved to be successful in soils that do not contain substantial amounts of bound water (Robinson et al., 2003).

In addition to water content, the bulk electrical conductivity was measured with TDR and served as a control measurement for the ERT data. The bulk electrical conductivity (EC_b, $S.m^{-1}$) was obtained from the TDR signal attenuation for measurement times much greater than the main detection of the reflected signal. We related the signal attenuation to the bulk electrical conductivity of the soil in the vicinity of the TDR rods using the relationship (Heimovaara, 1995; Mallants et al., 1996):

$$EC_b = \frac{K_p}{R_{TDR} - R_{Cable}} , \qquad (7)$$

where K_p is the cell constant of the TDR probe, R_{Cable} is the resistance associated with cable tester, multiplexers, and connecters, and R_{TDR} is the ohmic resistance measured by the TDR. R_{TDR} is derived from ρ_∞, the reflection coefficient at very long times and is defined as:

$$R_{TDR} = Z_C \frac{(1+\rho_\infty)}{(1-\rho_\infty)} . \qquad (8)$$

where Z_C is the impedance of the TDR device, multiplexer and cable. Both K_p and R_{Cable} were determined for each probe individually using calibration measurements. The precision of the TDR probes was investigated during a period of ten consecutive days under hydraulic and chemical steady-state

conditions. The coefficient of variation (CV) for the EC_b-measurements during this period was always lower than or equal to 2%. We also inferred the TDR accuracy by fitting the measured EC to equation 7 for ten different calibration solutions and calculating the residual. Given the bulk electrical conductivities which we measured during the experiment (25–300 µS.cm^{-1} for the LS lysimeter and 140-800 µS.cm^{-1} for the S lysimeters), we can infer a TDR accuracy of 4% or better for EC measurements in the LS soil and of 7% or better for the S soil.

2.6 Monitoring solute concentration

The soil bulk electrical conductivity (EC_b) was assumed to be linearly related to the solute electrical conductivity (EC_w). The calibration parameters of this relationship depend on the volumetric water content and soil properties like porosity, pore connectivity and electrical conductance of the electrical double layer that surrounds the soil particles. These variables and properties vary with the location within the soil monolith. Based on EC_b-measurements at the start (t_0) and the end (t_{end}) of the experiment, the parameters of the relationship between EC_b and EC_w were derived for every pixel in the soil column as in Koestel et al. (2008) using the following equation:

$$EC_w(t) = \frac{EC_b(t) - EC_b(t_0)}{EC_b(t_{end}) - EC_b(t_0)} . (EC_w(t_{end}) - EC_w(t_0)) + EC_w(t_0).$$ **(9)**

Note that the water content was constant with time within the soil column during the experiment.

2.7 Inferring transport parameters

The convection-dispersion model (CDE) is the most widely used model to interpret and characterize tracer experiments (Vanderborght et al., 2007). The apparent velocity (v) represents the transport velocity of the solute front in the vertical direction, whereas the apparent dispersivity (λ) characterizes the variance of the solute arrival time at a certain point in a given realization of the velocity field (Vanderborght et al., 2006). To characterize the transport process at different vertical and horizontal scales, the CDE was fitted to breakthrough

curves (BTCs) of the CaCl$_2$-tracer or changes in electrical conductivity that were observed at different depths within the soil monolith and that were averaged over different horizontal scales:

$$\frac{\partial EC}{\partial t} = \lambda v \frac{\partial^2 EC}{\partial z^2} - v \frac{\partial EC}{\partial z} \ ,$$

(10)

where EC is the electrical conductivity, and v (cm.day^{-1}) and λ (cm) the velocity and dispersivity, respectively, and z (cm) the vertical coordinate.

A solution of the CDE for a 1st and 3rd type top surface boundary condition was fitted to, respectively, BTCs that were observed in the effluent of the column and BTCs that were observed within the column (van Genuchten et al., 1984). In case the CDE was fitted to locally observed BTCs, the locally observed breakthrough was interpreted as the result of an equivalent one-dimensional convection-dispersion process (CDE) along a one-dimensional stream tube. This approach conceptualizes the soil as an ensemble of independent vertical stream tubes (STM) which represent the complex three-dimensional flow field. The number of stream tubes used in the analysis depends on resolution of the measurement method. For ERT measurements, the number of stream tubes at a certain depth depends on the number of voxels of the inversion mesh intersecting that depth. For the LS this resulted in 640 stream tubes and for the finer mesh of the S1 and S2 lysimeters in 1115.

The water distribution in the soil columns is not assumed to be homogeneous. In fact, we do not know the local water flux at a certain location in the lysimeter. As a consequence, smaller apparent velocities may also be due to local smaller water fluxes. For instance, a breakthrough curve that is observed in a region that is to a large part bypassed by the flow and in which the flow rate is much smaller than the average flow rate, will have a smaller velocity than the average velocity.

2.8 Different observation scales

To investigate different manifestations of preferential flow we observed tracer transport in the lysimeters at different scales. We distinguished three lateral observation scales and two vertical scales. In the lateral direction, the first observation scale corresponds to the scale of an individual voxel of the ERT mesh (subscript "vox"), i.e., approximately 7 cm length. The second lateral observation scale is related to the TDR measurement scale (subscript "tdr") which corresponds to the size of the measurement volume of an individual TDR probe based on Ferré et al. (1998). This is a cylinder with a length equal to the length of the probes (ca. 20 cm) and a radius of twice the distance between two rods of the probe. The third lateral observation scale investigated in this study is the column scale (subscript "col") (116 cm). The column scale transport is represented by the concentrations or electrical conductivities in the effluent of the column and by horizontally averaged conductivities within the soil column, which are derived from ERT measurements. It must be noted that preferential flow paths with a smaller dimension than the voxel scale may still be detected as a rapid increase in breakthrough that is followed by a long tailing of the breakthrough in that voxel.

In the vertical direction, two observation scales are distinguished which are related to the local and integral transport distance, respectively. The integral transport distance refers to the transport parameterization along a stream tube between the soil surface and a given depth. The integral velocity (v) is obtained directly from the CDE fit to the BTC of a voxel at a certain depth z_i. It is the integrated velocity along the trajectory of a solute particle from the soil surface to the observation depth. The local transport parameters refer to the transport process between two observation depths. We considered a local transport distance of 25 cm which corresponds to the distance between TDR probes in the soil columns. The local velocity (u) at depth z_i was then calculated from $v(z_{i+2})$ and $v(z_{i-2})$ as follows:

$$u_{z,i} = \frac{z_{i+2} - z_{i-2}}{\left(\dfrac{z_{i+2}}{v(z_{i+2})}\right) - \left(\dfrac{z_{i-2}}{v(z_{i-2})}\right)},$$

(11)

where i denotes the ith horizontal voxel node layer starting from the soil surface to the bottom of the lysimeters. The LS mesh has 23 voxel node layers and S1 & S2 have 59.

Table 4. Overview of the different observation scales in the lysimeter and the corresponding measurement methods.

HORIZONTAL SCALE	VERTICAL SCALE	
	Integral	Local
Voxel scale (ca. 7 cm) (vox)	ERT	ERT
TDR scale (ca. 20 cm) (tdr)	ERT,TDR	ERT
Column scale (ca. 116 cm) (col)	ERT,TDR, Effluent	ERT

2.9 Lateral mixing

As stated before, one manifestation of preferential flow is the lack of mixing or solute mass exchange between regions with low and high advection velocities. This leads to a stronger increase of the solute spreading in the vertical direction than predicted by a convective-dispersive transport model. The nature of the mixing regime may be derived from the change of the apparent dispersivity with transport distance. A linear increase of dispersivity with transport distance indicates no-mixing or a stochastic-convective process, whereas a constant dispersivity is a sign of perfect mixing or a convective-dispersive regime. In addition to mixing processes, vertical variations in soil properties (soil layering) may also lead to changes in dispersivity with depth. Other parameters, which are more direct indicators of the mixing regime, are the coefficient of variation of the local and intergral velocities (Koestel et al., 2009). A decreasing CV(v) with

travel distance indicates lateral mixing if, at the same time, the corresponding CV(u) remains constant. For a constant CV(u) with depth, a constant CV(v) indicates that no lateral mixing occurs (Javaux et al., 2003). The CVs were calculated for the integral and local voxel scale velocities, v and u respectively, as follows:

$$CV(v) = \frac{\sqrt{\mathrm{var}(v_{vox,ERT})}}{v_{vox,ERT}} \quad and \quad CV(u) = \frac{\sqrt{\mathrm{var}(u_{vox,ERT})}}{u_{vox,ERT}}. \qquad (12)$$

Convective-dispersive transport is connected with a decreasing CV(v) for increasing travel distance whereas the CV(u) stays approximately constant. However, if CV(u) as well as CV(v) stay constant with depth, the mixing is incomplete and stochastic-convective transport can be assumed (Javaux et al., 2003).

2.10 Spatio-temporal Behaviour of solute leaching

Several studies on solute transport in soils were done using multi-compartment samplers (Poletika et al., 1994; Quisenberry et al., 1994; Buchter et al., 1995; De Rooij et al., 2000), because these samplers provide information about the distribution of the solute both in space and time. The temporal aspect of solute leaching is characterized by the BTC, which describes the travel time of the solute at a given depth (Bloem, 2008). Stagnitti et al. (1999) and de Rooij and Stagnitti (2000) indicated that spatial variability of solute movement can be illustrated and quantified using the spatial solute distribution curve. This curve yields the total amount of leached solute as a function of the fraction of the total sampling area, with the sampled compartments sorted from high to low leaching rates. By plotting the BTCs of the individual compartments next to one another in order of decreasing total leaching, these authors introduced the leaching surface. The shape of this surface highlights the key features of the leaching process and facilitates the analysis of the combined variation of solute fluxes in space and time.

Leaching surfaces have been derived from local solute flux measurements after a Dirac pulse solute application. In our experiments a step input was used and local resident solute concentrations were derived. As illustrated by Bloem et al. (2008) leaching surfaces that are derived from resident concentrations may differ substantially from solute flux leaching surfaces. We defined horizontal cross sections or control planes in LS, S1 and S2 at 108, 106 and 107 cm depth respectively and derived the BTCs for the voxels in these planes in order to derive the corresponding leaching surfaces. These voxel planes where chosen because they represent practically the same vertical tracer travelling distance for all three columns and they lie in the bottom part of the lysimeters. The step pulse BTCs were translated to BTCs resulting from a Dirac pulse using the fitted CDE parameters and the solution of the CDE for a Dirac tracer application and a 1st type boundary condition. The predicted concentrations were normalized by the 0th moment of the BTC and the normalized BTC represents a travel time distribution. Subsequently, the normalized solute flux (J_s, cm.day^{-2}) was calculated by multiplying the normalized BTCs with the local velocity (u) and the volumetric water content (WC). Since the volumetric water content was not observed for each individual pixel, the average water content derived from the TDR measurements was used. The pixels in the control plane where then ranked in order of descending amount of cumulative leaching. Subsequently, we plotted the leaching surface (Surf(x,t), cm^{-2}.day^{-1}), as in de Rooij and Stagnitti (2002) (see Figure 13), whereby the horizontal x-axis represents the cumulated area of the sorted pixels (x^2 in Figure 13), the horizontal t-axis represents the time and the vertical axis the scaled flux Surf(x,t). The scaled solute flux is defined as:

$$Surf(x,t) = J_s(x,t) \left(\int_{t_0}^{\infty} \int_0^A J_s(x,t) dx dt \right)^{-1} , \qquad\qquad (13)$$

where t_0 is the application time and A the area of the reference plane. A cross-section of Surf parallel to the x-axis and at a certain point in time t* gives the spatial solute distribution curve (SSDC):

$$SSDC(x)\big|_{t*} = Surf(x, t*), \quad x \in [0, A].$$ (14)

The scaled total amount leached (STAL) at the end of the experiment (t*=∞) for each pixel was calculated as follows:

$$STAL(x)\big|_{t*} = \int_{t_0}^{t*} Surf(x, t)dt, \quad x \in [0, A].$$ (15)

We can then calculated the cumulative spatial solute distribution curve that represents the maximal fraction of the applied solute mass that leaches through a certain area within the reference plane (FTL):

$$FTL(x) == \int_{0}^{x} \int_{t_0}^{\infty} Surf(\chi, t)dtd\chi, \quad x \in [0, A].$$ (16)

As in Stagnitti et al. (1999), we fitted the cumulative density of the standard beta function to the curve resulting from FTL(x) and calculated the scaled heterogeneity index (HI) as:

$$HI(\alpha, \zeta) = \sqrt{\frac{3\zeta}{\alpha(\alpha + \zeta + 1)}}$$ (17)

where α and ζ are free parameters of the standard beta function defined by Bronshtein and Semendyayev (1979).

38

3. Results

3.1 3-D Distribution pore water electrical conductivity (EC$_w$)

Figure 7 shows the three-dimensional distribution of EC$_w$ at three different stages of the experiment, when similar amounts of pore volumes were leached through the different soils. Although the tracer transport is not totally homogeneous in the LS (top line in Figure 4), the tracer front does not have clear fingering or preferential flow patterns and we can still speak of rather homogeneous solute transport for this soil under the given boundary conditions. On the contrary, the tracer front in S1 is much more heterogeneous (bottom line of Figure 7). In the first time step shown in the image, a preferential flow path or tongue can be seen in the bottom left area of the lysimeter. Figure 8 gives a more detailed representation. This tongue appears at the very beginning of the experiment in the ERT time series and remains visible until 1.5 months after the start. After that, the whole pore volume is slowly replaced by the applied tracer concentration. In the second lysimeter (S2), which was taken from the silty soil but which is not shown in Figure 7, such distinct preferential flow paths were not observed. But, similar to the transport in lysimeter S1, the initial pore water was gradually replaced by the infiltrating tracer solution. This is in contrast with the LS lysimeter in which the invading tracer front rapidly replaces the initial pore water.
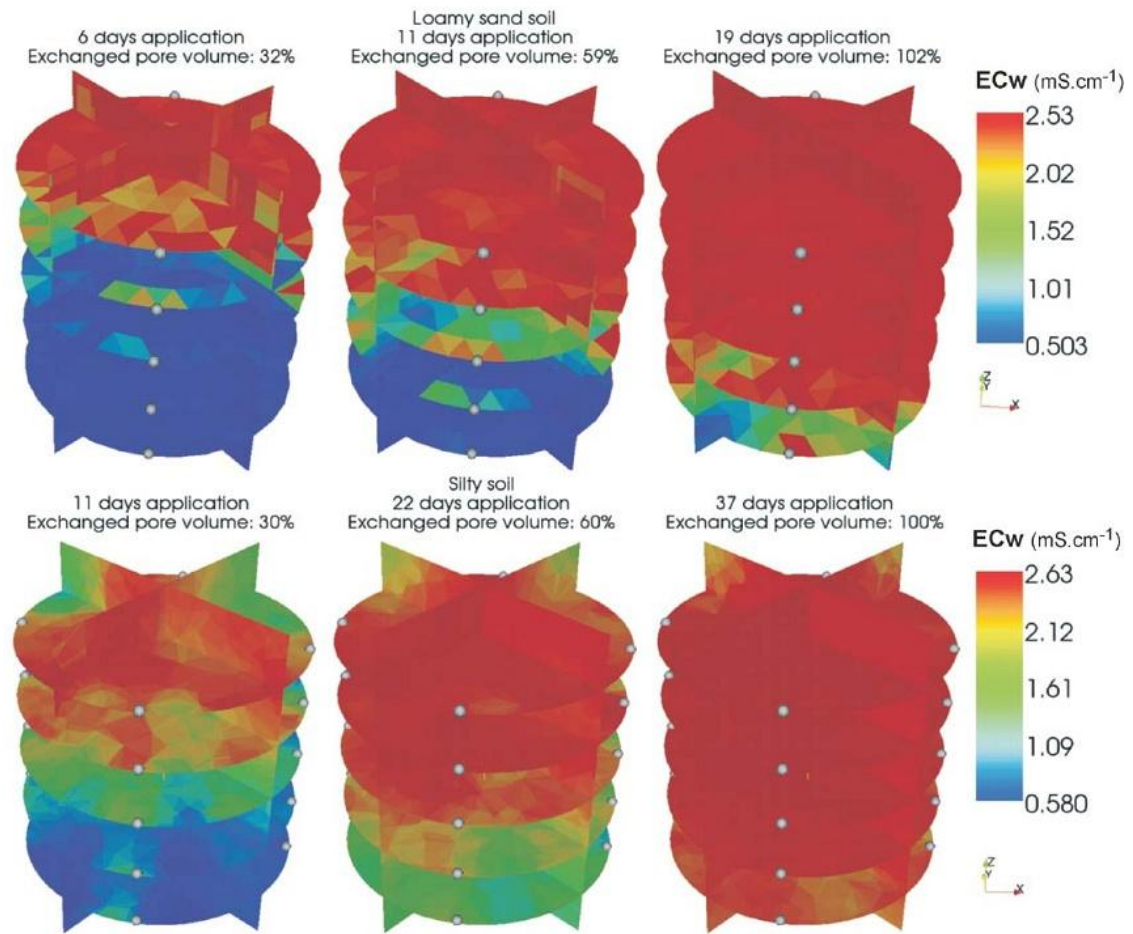
Figure 7. **3-D solute electrical conductivity for both lysimeter experiments. (top) Loamy sand soil at t=6days, 11days and 19days. (bottom) Silty soil S1 at t=11days, 22days and 37days. The grey spheres represent TDR probe locations in the lysimeters.**
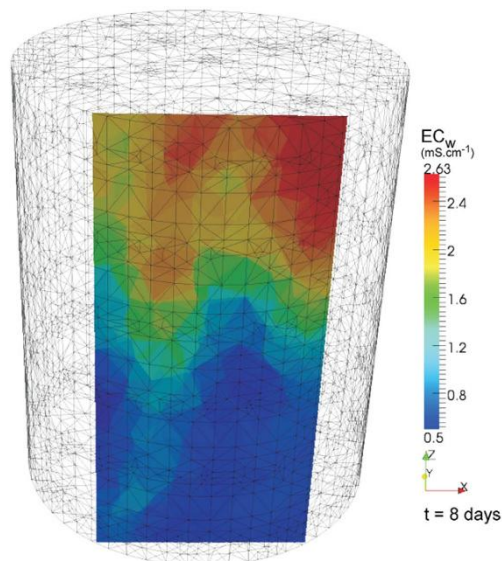
Figure 8. **Detail of a preferential flow tongue in terms of 3-D solute electrical conductivity after 8 days of tracer irrigation in lysimeter S1.**

3.2 Breakthrough curves at different scales as indicators of heterogeneity and preferential flow processes

Figure 6 shows the local (a) and column scale (b) BTCs that were measured in the LS and S lysimeters. The BTCs are normalized by the total pore volume of the column. This is a way to normalize time for experiments in two different soils and thus, it allows us to compare the shape of the BTCs. In the S soils, the local BTCs at one depth differ considerably in terms of arrival time suggesting heterogeneous transport in the lysimeter. The TDR probe of the second transect that shows an early breakthrough is located close to the preferential flow path in the lysimeter (see Figure 4 and Figure 8). In general, there is a good agreement between ERT and TDR. The ERT derived BTCs in the voxels located in the TDR sampling volume reproduce the tracer front arrival time measured by the TDR probes quite well. However, ERT seems to overestimate the spreading of the BTC. This effect stems from the smoothness constrained inversion of the resistivity data (Kemna et al., 2002; Vanderborght et al., 2005). This overestimation of the spreading has an effect on the estimated dispersivities from locally observed BTC in an ERT voxel as will be shown further.
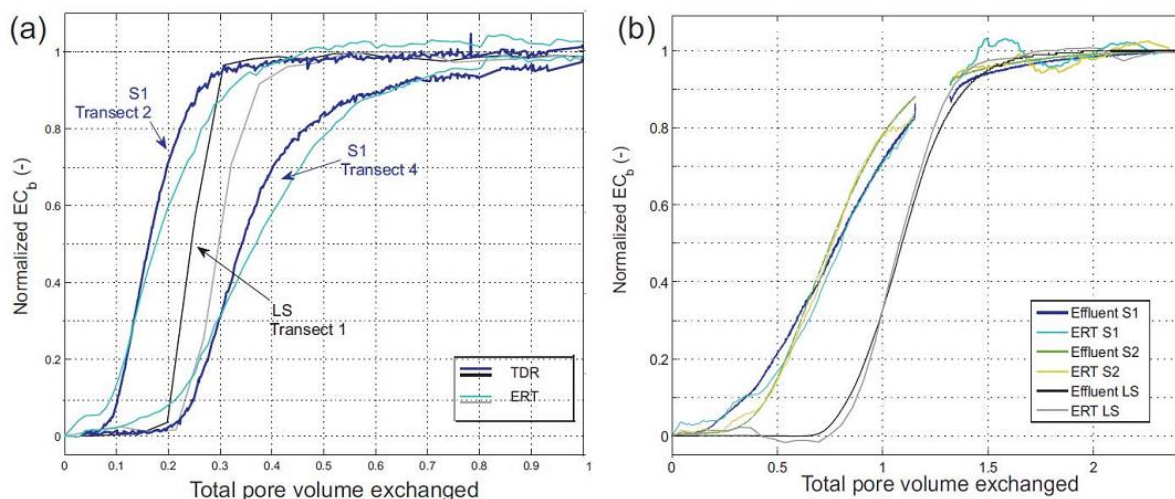
Figure 9. (a) Normalized breakthrough curves of ERT and TDR for the steady-state tracer experiment in both soils at a depth of -47.5cm (gray=LS, blue=S1). (b) Normalized breakthrough curves of column-scale averaged ERT and effluent conductivity measurements for the sand and silty soils (gray=LS, blue=S1, green=S2).

41

The BTCs that were measured in the effluent of the lysimeters correspond well with the column scale averaged BTCs that were derived from ERT measurements. The mean arrival time of the solute at the outlet is earlier in the S soil than in the LS soil if time is expressed in total pore volumes that are already exchanged. The column-scale BTCs also show a larger spreading in the S soil than in the LS soil, which again indicates a more heterogeneous transport in the S soil. It should also be noted that the preferential flow path that is observed in S1 corresponds to a more rapid increase of the tracer concentration in the effluent in S1 than in S2. However, this rapid increase in tracer concentration is not extremely outspoken and from the shape of the BTC in the effluent of S1, it is hard to infer the presence of a preferential flow path in this lysimeter.

3.3 Characterization and quantification of heterogeneous transport

A. Convection-dispersion parameters

Figure 10 shows the CDE parameters fitted to the TDR-scale breakthrough curves measured with ERT and TDR. The apparent integral velocities (v) of ERT and TDR measurements agree well apart from two outliers for the S soils. The coefficients of determination (R^2) are 0.975 for the LS and 0.593 for the ensemble of S1 and S2. The apparent dispersivity (λ) from both measurement methods also agrees, but there are some deviations. For the S soils, the R^2 is rather low: 0.308, whereas the LS has a R^2 of 0.774. The deviations are probably due to the effect of the smoothness constraint on the ERT breakthrough curves. Some measurements were characterized by very high dispersivities. This is caused by BTCs obtained along the preferential flow path, which can have a bimodal breakthrough or a quick increase of solute concentration followed by an extremely long tailing. In these cases, the fitted CDE parameters do not represent the real breakthrough well.

The apparent CDE parameters of column averaged data and effluent tracer breakthrough are plotted in Figure 11 together with the average of the local scale apparent CDE parameters. In general, there is a good agreement between parameters derived from ERT, TDR and effluent measurements
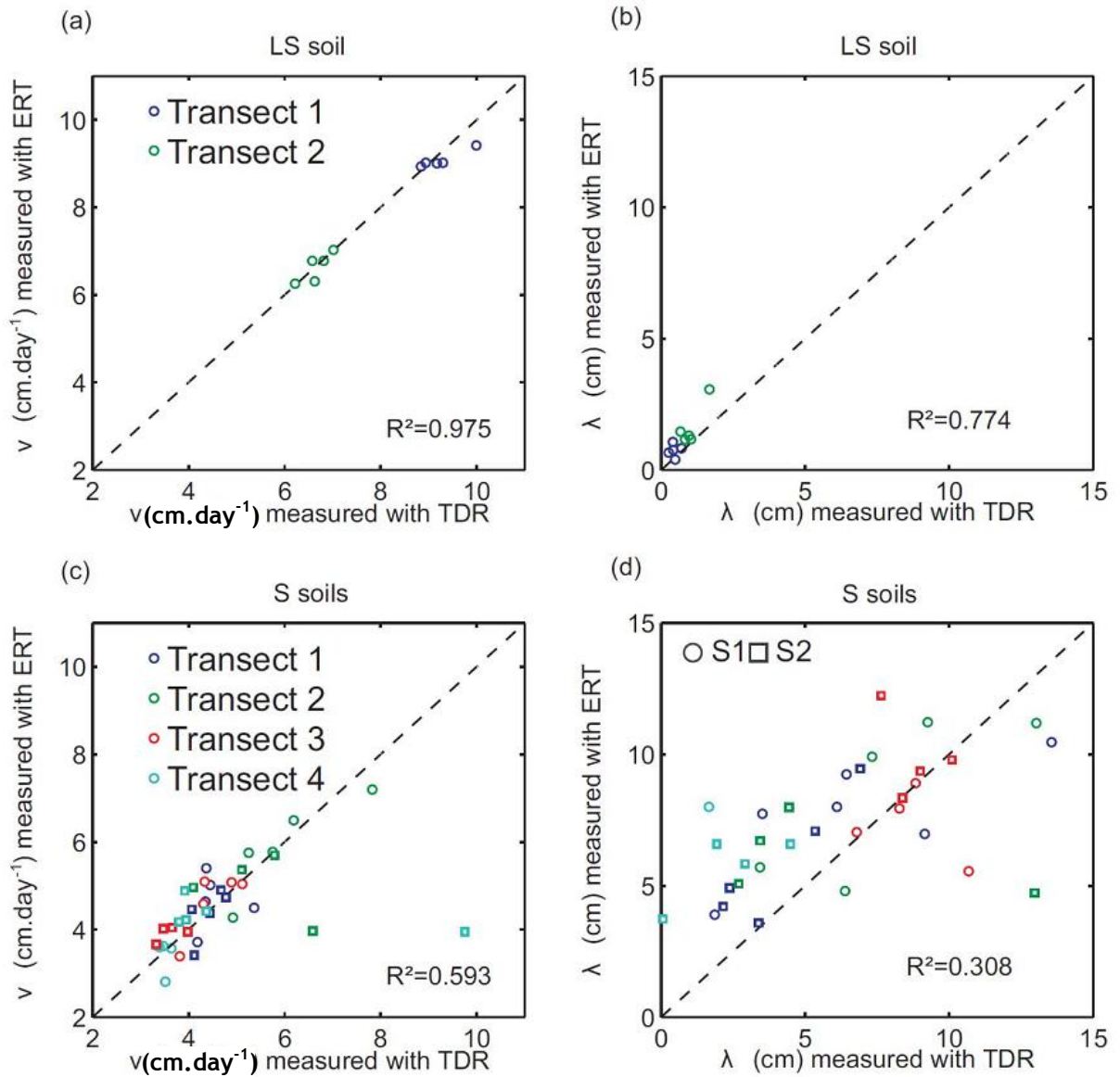
Figure 10. CDE parameters fitted to BTCs of ERT and TDR: (a) apparent velocity for the BTCs of the LS, (b) apparent dispersivity for the BTCs of the LS, (c) apparent velocity for the BTCs of the S soils (S1: circle, S2: square), (d) apparent dispersivity for the BTCs of the S soils (S1: circle, S2: square).

except for the apparent dispersivities at some depths for the S monoliths. This can be explained by the fact that the column scale dispersivity (λ_{col}) does not only account for local scale dispersion processes. It also contains the effect of the variation in stream tube velocity on the column scale averaged breakthrough. This effect may be missing in the TDR derived BTCs as the

number of TDR probes may be too small to obtain a representative sample of the stream tube velocities.
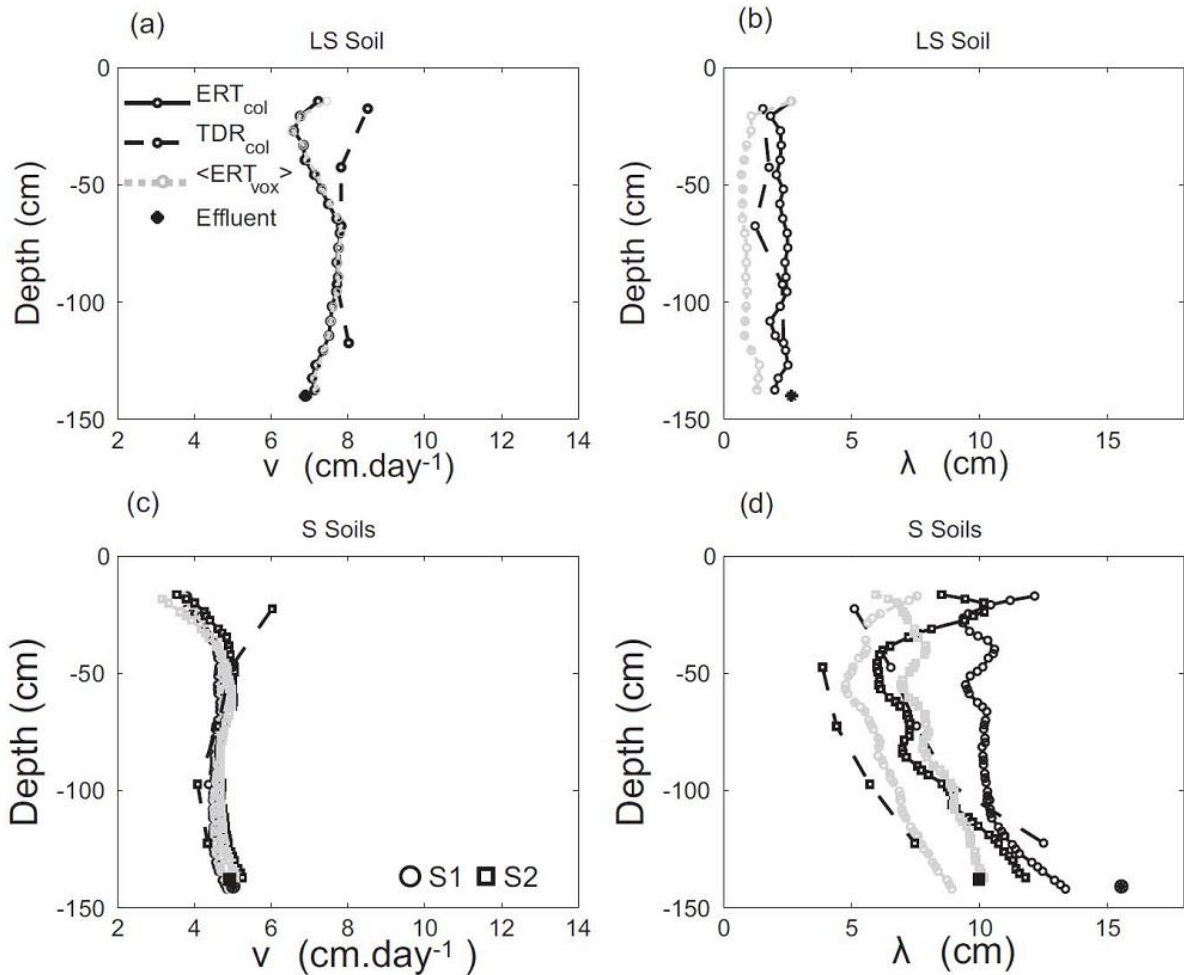
Figure 11. CDE parameters fitted to the column-scale BTCs from ERT, TDR and effluent conductivity measurements and the average of the CDE parameters for the voxel scale BTCs: (a) apparent velocity for the BTCs of the LS, (b) apparent dispersivity for the BTCs of the LS, (c) apparent velocity for the BTCs of the S (S1: circle, S2: square), (d) apparent dispersivity for the BTCs of the S (S1: circle, S2: square).

As can be expected, the velocities at voxel, TDR and column scale in the finer textured soils (S) are smaller than in the soil with the coarse texture (LS). The v_{tdr} and v_{vox} fitted to TDR and ERT BTCs vary mainly between 6 and 9 cm.day^{-1} for the LS and between 3 and 5 cm.day^{-1} for the S soil. The volumetric water content in the S soils is twice the water content in the LS soil (see Table 2) and the saturated hydraulic conductivity of the LS soil is higher than the one of the S

44

soils (see Table 1). This can explain the fact that the transport is slower in the S soils. The voxel and tdr scale dispersivity (λ_{vox} and λ_{tdr}) in the LS soil lie between 1 and 2 cm, whereas those of the S are mainly between 3 and 10 cm. The S soils clearly have a larger dispersivity than the LS soil. The differences between both soils are also visible at the column scale (see Figure 11). In both soils, the column scale dispersivity is larger than the voxel scale dispersivity. This indicates that variations in advection velocity that exist at a scale that is larger than the scale of an ERT voxel have an influence on the λ_{col} or solute spreading that is apparent at this scale. However in S2, the λ_{vox} determines λ_{col} to a large extent as the difference between the average voxel scale dispersivity ($< \lambda_{vox} >$) and λ_{col} is not big. This indicates that in S2 small scale dispersion processes, which cannot be resolved by ERT, play an important role. In this case, the variation of the local velocity should not have an important impact on the solute spreading. However, the local velocity variance is almost identical for both S1 and S2. This implies that the correlation scale of the local velocity must be larger in S1 than in S2. This is in line with the larger CV of the integral velocity in S1 than in S2. The different behaviour of the column scale dispersivity as compared to the average of the voxel scale dispersivity in S1 and S2 may thus be related to the vertical correlation of the advection velocities in the preferential flow path that was observed in S1.

An indicator for the identification of transport processes is the behaviour of λ_{col} with depth. A linear increase of λ_{col} with travel distance indicates that lateral mixing is not complete. The solute transport process can then be described as stochastic–convective. In contrast, a constant λ_{col} indicates that solute spreading can be described as a diffusive or Fickian process (Roth et al., 1996; Vanderborght et al., 2001). For the LS soil, there is no linear increase with depth (see Figure 11). Thus, the transport can be called convective-dispersive. S1 and S2 do have an increase of λ_{col} with depth, except for the top 25 cm. As Koestel et al. (2009) pointed out, the apparent dispersivity can only be used as an indicator for the mixing regime under the assumption that the local velocity variability remains constant and does not change with depth. For the LS soil,

45

this is the case, but for both S1 and S2 it should be noted that there are important changes in variability of the local velocities between the soil layers (see Figure 12). Therefore, it is not possible to draw an unambiguous conclusion about the transport behaviour in the silty lysimeters.

The change of the CDE parameters with depth is another indicator to characterize solute transport processes. The coefficients of variation of velocity (integral and local) for both soils are plotted in Figure 12. It can be seen that the coefficient of variation (CV) of the integral apparent velocities (CV(v)) decreases with depth for all three lysimeters. Meanwhile, the CV of the local velocities (CV(u)) stays more or less constant for LS. As already pointed out by Koestel et al. (2009), this is an indication that the LS soil has a Fickian solute mixing regime. For S1 and S2, the effect of soil layering on CV(u) profile is clearly visible, which is not the case for LS. The plough horizon in this agricultural soil is rather deep and the depth of the boundary of the horizon varies between 30 and 44 cm according to several studies in the test field the lysimeters were taken from (Pütz, 1993; Schmidt-Eisenlohr, 2001; Reinken, 2004 ; Burkhardt et al., 2005). The plough horizon seems to have an impact on u in S1 and S2. In the second horizon, the CV(u) stays high for both S lysimeters and decreases abruptly after. The sudden variation of local transport velocities across horizon interfaces may be due to a bad connectivity or redistribution between flow paths across the interfaces. In the neighbourhood of the compacted plough pan, which is occasionally perforated with earthworm holes and roots (Burkhardt et al., 2005), the main transport direction may become more lateral than vertical. This indicates that our method to calculate the local velocity is not appropriate in this case. In between the abrupt changes, the CV) is constant with depth for S1 and S2. Until now, the effect of soil layers on the transport process was not identified as clearly as we can see it in this study. Seuntjens et al. (2001) already showed that solute transport in a Spodosol is affected by the soil morphology by measuring and analysing BTCs with several TDR probes in different layers. However, ERT allowed us to analyze the transport process in

much more detail throughout the whole lysimeter volume and made it possible to show the effect of soil morphology very clearly.

If we now compare Figure 11 and Figure 12, we can see that the decrease of the dispersivity in the S1 beneath a depth of ca. 20 cm corresponds to a decrease in local velocity variance. In the deepest soil layer, the variance of the local velocity increases again drastically and this is accompanied by a stronger increase with depth of the dispersivity in this layer. This is again a proof for the fact that the column scale dispersivity in S1 depends on the variation of the local scale velocities.
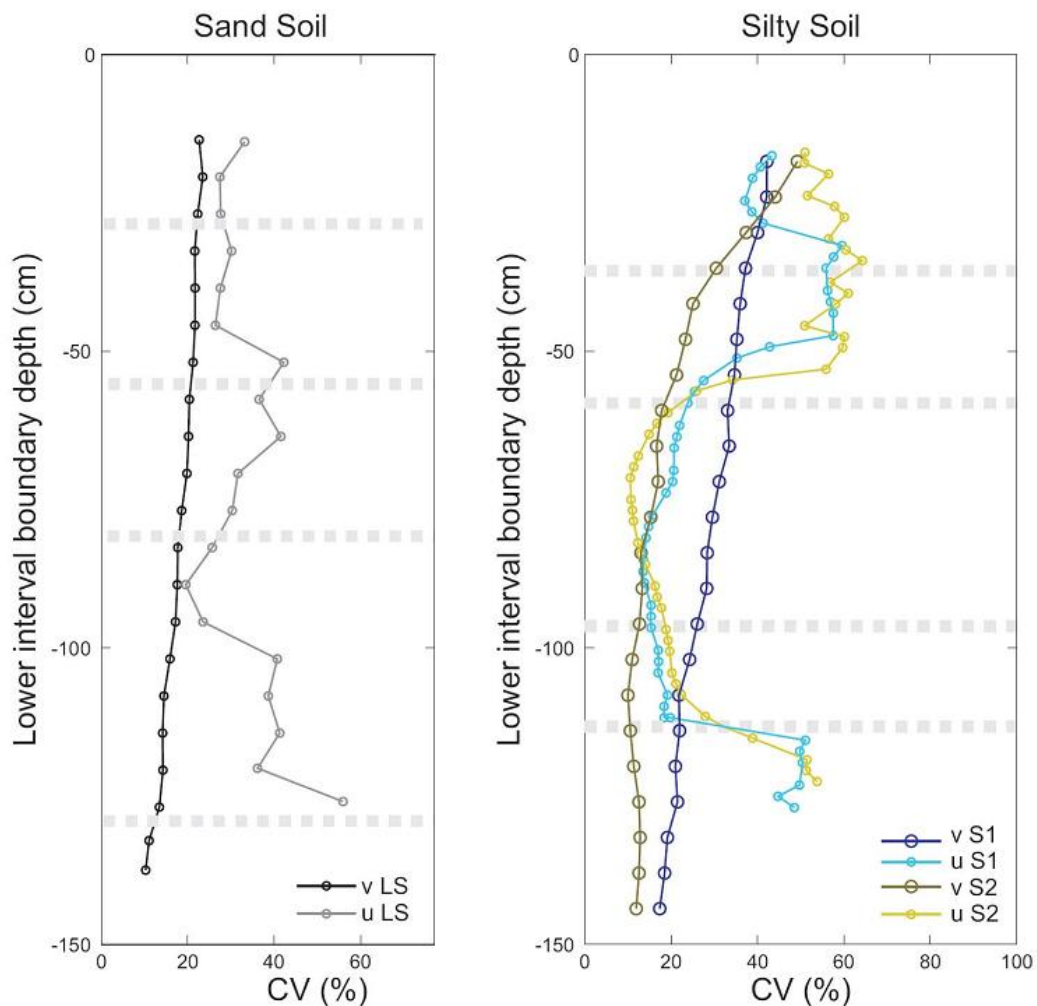
Figure 12. Coefficients of variation of the voxel-scale integral, v, and local, u, velocities for the LS soil (left) and S soil (right). Horizon boundaries are indicated with dashed lines.

B. Leaching surfaces

Figure 13 shows the local velocity-based leaching surfaces for both soils. The leaching surfaces are clearly different for the two soil types, which illustrates the different transport in the two soils. The S1 and S2 have a rather smooth leaching surface, with a very small portion showing a high peak. This high peak is most pronounced in S1, the lysimeter where a preferential flow path was detected with ERT. The leaching surface of the LS soil seems more irregular, which indicates that the local solute flux is not correlated with the tracer arrival at a certain location and that the spreading of the local breakthrough curves does not override the variation in arrival time. Since the apparent dispersivities of the local BTCs are smaller and the apparent velocities are larger in the LS than in the S soil, the peaks in the leaching surface are larger in the LS than in the S1 and S2.

Subsequently, we plotted the scaled total amount leached (STAL) for each area of the control plane and the fraction of the total leaching (FTL) in Figure 14. The smaller the curvature (i.e. wider curve) of the FTL curve, the more evenly distributed the leaching process is. The curves of LS, S1 and S2 are similar, but some differences can be seen. The Kolmogorov-Smirnov test indicates that there is a significant difference between the LS and the S curves at a significance level of 13 %. The biggest difference between the LS and the S soils can be seen between STAL(x=0.2) and STAL(x=0.9). Except for a limited number of areas with very high and very low leaching, the total amount leached through the areas is similar in the LS soil, which follows from the nearly horizontal course of the STAL curve between x=0.2 and x=0.9. This is not the case for both S soils. S1, the lysimeter with preferential flow behaviour, has the significance level of 13 %. The biggest difference between the LS and the S soils can be seen between STAL(x=0.2) and STAL(x=0.9). Except for a limited number of areas with very high and very low leaching, the total amount leached through the areas is similar in the LS soil, which follows from the nearly horizontal course of the STAL curve between x=0.2 and x=0.9. This is not the case for both S soils. S1, the lysimeter with preferential flow behaviour, has the
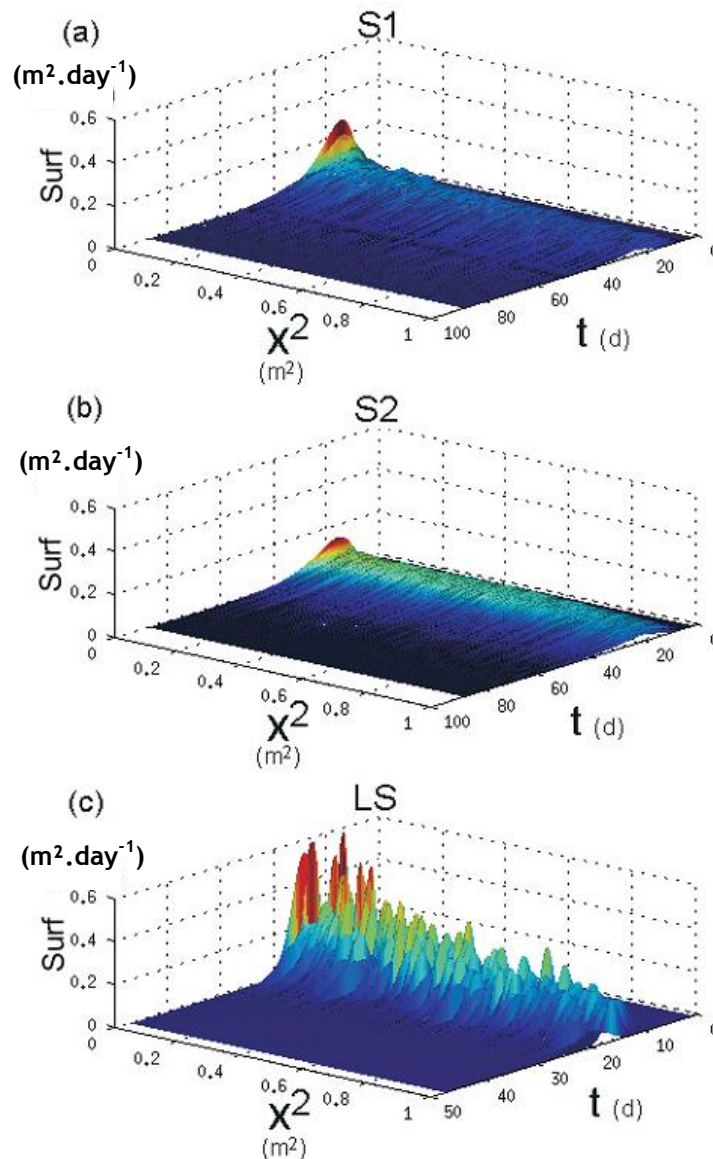
Figure 13. Apparent velocity based leaching surfaces for S1,S2 and LS (a,b and c). The subplots a and b were built of 1115 observations, whereas subplot c has 630 observations.

significance level of 13 %. The biggest difference between the LS and the S soils can be seen between STAL(x=0.2) and STAL(x=0.9). Except for a limited number of areas with very high and very low leaching, the total amount leached through the areas is similar in the LS soil, which follows from the nearly horizontal course of the STAL curve between x=0.2 and x=0.9. This is not the case for both S soils. S1, the lysimeter with preferential flow behaviour, has the

highest STAL of all three lysimeters in the highest ranked areas. This indicates that only a small number of voxels is responsible for the spotted preferential flow path. The heterogeneity index (HI) of the LS soil is 1.14, whereas HI(S1)=1.20 and HI(S2)=1.18. As Stagnitti et al. (1999) showed, a uniform distribution of the solute transport throughout the control plane will result in a HI=1. A non-uniform distribution is indicated when HI>1 and the magnitude of the HI>1 indicates the magnitude of the non-uniformity. The fact that HI is higher for the S soils than for the LS soil is also the result we would expect after observing the ERT data for the lysimeters. However, the difference between the HIs is rather small. De Rooij and Stagnitti (2000) reported a HI of 1.32 for a soil column from sandy mesic Typic Psammaquent. (Steenhuis et al., 1990) indicate values between 1.31 and 1.56 for soil cores from a dark basaltic soil with high organic content.
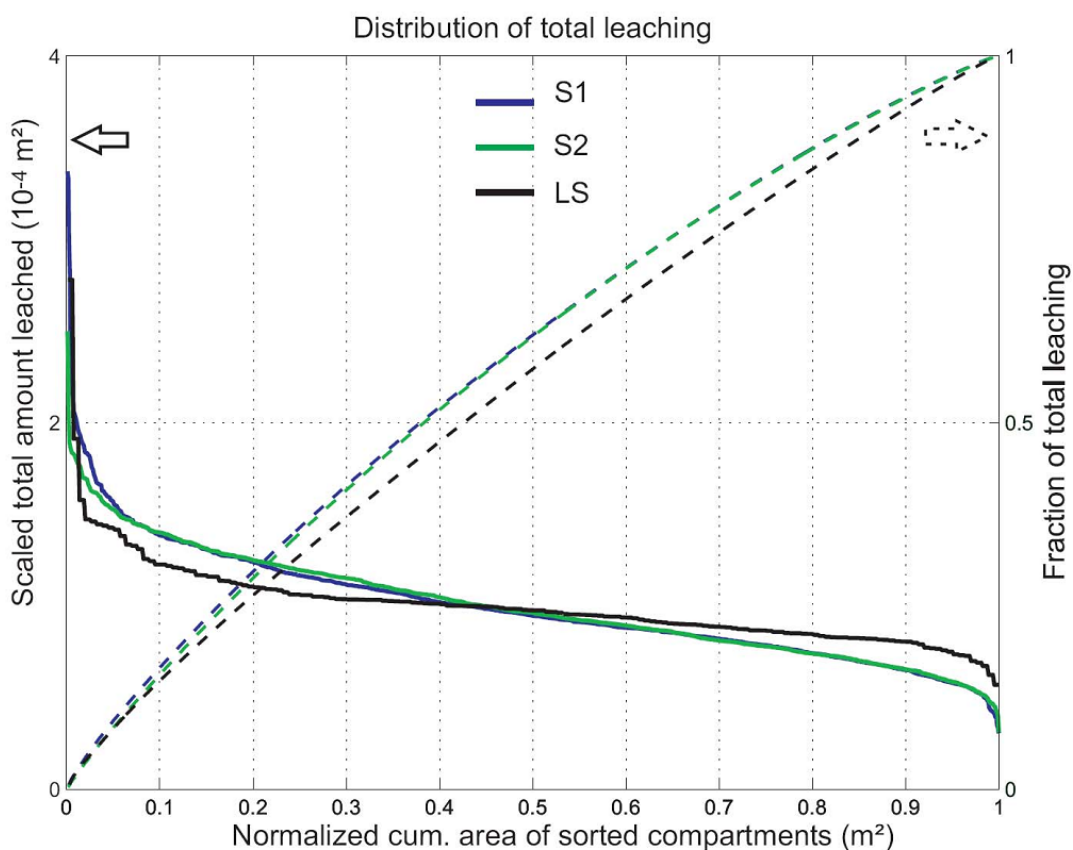
Figure 14. Cumulative solute leaching for the control plane in all 3 lysimeters.

4. Conclusions

In this paper, we compared solute transport in two different unsaturated and undisturbed soils: a loamy sand (LS) and a silty soil (S). The solute transport in the two soils differed considerably in terms of heterogeneity, solute spreading, and appearance of preferential transport. By using a non-invasive imaging technique, ERT, in combination with TDR measurements and concentration measurements in the effluent of the soil column, different aspects of the transport process and manifestations of preferential flow within two different soil types were investigated. We used voxel and column scale effective CDE parameters, leaching surfaces and local velocities that were derived from the imaged tracer front movement to analyze the observed transport process.

The presence of a constant apparent column scale dispersivity with depth in the LS soil combined with a decrease of the coefficient of variation of the apparent integral velocity and a rather constant coefficient of variation of the local velocity suggested a complete lateral solute mixing and therefore a convective-dispersive transport process at the lysimeter scale. However, the irregular leaching surface and the difference between the local and column scale dispersivities pointed at the presence of a heterogeneous transport process and preferential flow within this soil leading to spatial variations of local solute concentration in a horizontal plane. This implies that a transport process that appears homogeneous at a larger scale may hide preferential transport at smaller scales.

Transport in the lysimeters S1 and S2 was considerably more heterogeneous than in the LS lysimeter as indicated by the larger apparent column scale dispersivity and the smaller lateral mixing. Analysis of the leaching process in the S1 and S2 lysimeters showed a distinct preferential flow path in S1 which was not observed in the LS lysimeter and which affected the column scale averaged BTC. However, inference of the presence of such a preferential flow path from this BTC seems impossible. Despite the fact that its presence is hardly reflected in the effluent of the salt tracer, this preferential flow path may

have large impacts on the transport and leaching of reactive tracers. Analysis of leaching surfaces at selected reference planes was shown to be more suited to infer the presence of such preferential flow paths than the analysis of effluent data. A major part of the solute spreading that was observed in the effluent of the S soil was caused by small scale dispersion processes as is indicated by the smooth leaching surfaces and the large voxel scale dispersivities. Besides the large voxel scale dispersion, there was still an important variability in advection velocity. Our analysis showed that the variability of local scale velocities changed considerably across soil layer boundaries due to considerable differences in their transport properties. These properties are difficult to infer from a few local scale measured breakthrough curves. Using non-invasive techniques, breakthrough curves can be derived on a grid of locations from which local velocities can be inferred. These velocity distributions were closely linked with soil layers in the S soil. Furthermore, they could be used to derive leaching surfaces in situ, which is important to identify the presence of preferential flow paths.
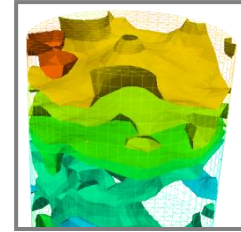
3-D Electrical Resistivity Tomography to Monitor Root Zone Water Dynamics[2]

Abstract.

Knowledge of soil moisture dynamics and its spatial variability is essential to improve our understanding of root water uptake and soil moisture redistribution at the local scale and the field scale. We investigated the potential and limitations of Electrical Resistivity Tomography (ERT) to measure 3-D soil moisture changes and variability in a large, undisturbed, cropped soil column and examined the interactions between soil and root system. Our analysis sustained the value of ERT as a tool to monitor and quantify water contents and water content changes in the soil, as long as the root biomass does not influence the observed resistivity. This is shown using a global water mass balance and a local validation using Time Domain Reflectrometry (TDR) probes. The observed soil moisture variability was rather high as compared to values reported in the literature for bare soil. The measured water depletion rate, being the result of combined effects of root water uptake and soil water redistribution, was compared with the evaporative demand and root length densities. We could observe a gradual downward movement of the maximum water depletion rate combined with periods of redistribution when there was less transpiration.

---

1. Introduction

An accurate knowledge of the processes governing soil moisture variability and water redistribution in the soil-plant continuum is necessary for agricultural water management and predictions of the fate of agrochemicals. The amount of water plants can take up and transpire depends on soil water availability and the distribution of roots in the soil. However, controversy still remains about the main factor(s) controlling root water uptake, especially for a non-uniform soil moisture distribution and intermediately wet soil (Green et al., 2006). Due to nonlinear dependencies on water content, upscaling of root water uptake and evapotranspiration requires knowledge of the spatial statistics of local water contents. During the past decades, many studies have focused on measuring and understanding soil moisture variability at the field-scale and its interaction with root water uptake (RWU) (Katul et al., 1997; Coelho et al., 1999; Green et al., 1999; Vrugt et al., 2001; Teuling et al., 2005; Vereecken et al., 2008). However, the conclusions of these studies differ with respect to the mechanisms controlling spatial variability of soil moisture. Both soil properties and root water uptake processes may create or reduce spatial variability of soil moisture (Teuling et al., 2005). As Coelho and Or (1999) stated, actual water uptake patterns in the field reflect a complex interplay between the root system and other soil factors such as water, nutrient and aeration status of the root zone.

Until now, a large number of the studies dealing with the interplay of plant roots and soil moisture at the large column or field scale used either destructive measurements of water contents such as soil cores (e.g. Sharp et al., 1985) or a grid of in-situ measurement techniques including time-domain reflectometry (TDR) (e.g. Katul et al., 1997; Musters et al., 1999; Musters et al., 2000; Teuling et al., 2005) and neutron probes (e.g. Vrugt et al., 2001; Hupet et al., 2002a; Koumanov et al., 2006). Destructive measurements do not provide information on the temporal dynamics of the soil moisture whereas in situ measurement

techniques have a good temporal resolution but limited spatial extent and coverage.

In addition to highly resolved soil moisture measurements in space and time, studying the interaction between soil moisture and the root system also requires monitoring of root growth and densities. Root densities were frequently measured destructively using soil cores (e.g. Sharp et al., 1985; Katul et al., 1997; Coelho et al., 1999; Green et al., 1999). Minirhizotrons offer the possibility to observe the development of the root system in a non-destructive, yet invasive, way in large soil columns. Minirhizotron images give spatial and temporal information on root characteristics in the soil (e.g. Heeraman et al., 1993; Merrill et al., 1994; Dubach et al., 1995; Hendrick et al., 1996; Johnson et al., 2001; Bernier et al., 2004). Nonetheless, the observed volume of the root zone is very small and obtaining high temporal resolution is hampered by the high work load of the method.

Electrical resistivity tomography (ERT) allows us to monitor the volumetric soil water content (WC) with a higher temporal and spatial resolution as compared to conventional methods by measuring the bulk soil electrical conductivity (EC_b), which is related to the WC. It has an advantage over ground penetrating radar (GPR) because GPR performance decreases in electrically conductive media such as fine textured soils. ERT has mainly been used to monitor drainage and infiltration processes (Stubben et al., 1998; Glass et al., 2002; LaBrecque et al., 2002; Zhou et al., 2002; Descloitres et al., 2003; French et al., 2004; Amidu et al., 2007) and to image and characterize solute transport in bare soils (Binley et al., 1996; Binley et al., 1996; Henry-Poulter, 1996; Koestel et al., 2008; Koestel et al., 2009). The technique has been applied from the lab (e.g. Olsen et al., 1999; Werban et al., 2008) over the lysimeter (e.g. Binley et al., 1996; French et al., 2002; Koestel et al., 2009; Garré et al., 2010) up to the field scale (e.g. Daily et al., 1995; Slater et al., 1997; Daily et al., 2000; LaBrecque et al., 2002; Oberdörster et al., 2010). Only a few studies have used ERT to estimate root water uptake or root densities. Michot et al. (2003) monitored soil moisture

changes in an unsaturated, irrigated soil under corn using surface ERT. They showed that an in-situ calibration was needed to convert EC_b, derived from ERT to WC, since the relationship depended on the volume of soil. Similar results were obtained by Srayeddin and Doussan (2009) who also used ERT to measure root water uptake RWU under maize and sorghum at the field. Additionally, they concluded that the sensitivity/resolution of the technique should be optimized in field settings to improve the quantitative estimation over the whole rooted zone. This problem has been addressed in several studies (Friedel, 2003; Furman et al., 2004; Stummer et al., 2004; Gharibi et al., 2005; Maillet et al., 2005; Singha et al., 2006; Singha et al., 2006). But general conclusions about an optimal ERT setup cannot be drawn since sensitivity and resolution of ERT do not only depend on the electrode configuration, but also on the heterogeneity of the studied system, its overall conductivity and the magnitude of changes during the measurement period. In addition, several studies reported on the effects of the presence of roots on the EC_b (al Hagrey, 2007; Werban et al., 2008; Zenone et al., 2008; Amato et al., 2009), but the results were equivocal. It is expected that young, non-suberized roots will increase the EC_b, while older, suberized root segments may decrease the conductivity. In addition, EC_b might be affected by water filling or depletion of the possibly changing void space between the root and the soil matrix.

In this paper, we used ERT to measure 3-D soil moisture changes in a system as close as possible to a cropped field, i.e. in a large lysimeter, with a growing crop, undisturbed soil horizons and other elements of heterogeneity such as earthworm holes, fissures, etc present in the monolith. The aim of this study was to (i) investigate the potential and limitations of ERT to monitor 3-D soil moisture changes in a natural, cropped soil over a range of soil moistures using an in-situ calibration of the pedo-physical relationship; (ii) validate the ERT measurements in a global way, i.e. using a total water mass balance, and in a local way, using measurements of local water contents with TDR; (iii) examine the influence of root water uptake on soil moisture variability and soil moisture

changes with time; (iv) observe root growth non-invasively using a minirhizotron and link it to the observed soil moisture changes.

2. Material and Methods

2.1 Experimental design of the barley experiment

An undisturbed soil monolith was sampled using a large PVC column with a height of 150 cm and an inner diameter of 116 cm. The monolith was taken from intensively used arable land near Merzenhausen (Germany). The soil that developed in the Loess parent material was classified as an orthic Luvisol. Four soil horizons were identified: A_p (0-40 cm), B_t (41-70 cm), B_{v1} (71-100 cm) and B_{v2} (>100cm). More information on the lysimeter excavation, soil properties and equipment can be found in Part II: experimental set-up. The bottom boundary of the lysimeter was kept at -50 hPa by a polyamid-membrane suction plate (ecoTech GmbH, Bonn, Germany) and a vacuum pump (UMS, Munich, Germany). We equipped the lysimeter with a vertical transect of four horizontally installed minirhizotron tubes at -19.5, -44.5, -69.5 and -119.5 cm depth. The tubes are made of plexiglass, were 60 cm long and had a diameter of 5.72cm. A BTC2 video microscope (Bartz Technology Corporation, Carpinteria, CA, USA) was used to monitor root length density (RLD) and root growth on the outer walls of the tubes. At the start of the experiment, the volumetric water content in the bare column varied with depth between 0.30 and 0.45. After the summer barley (*Hordeum vulgare L.*) was sown in parallel lines ca. 20 cm apart on DOY 132, the soil did not receive any additional water until DOY 209. The first day of the experiment is thus DOY 132. Crop senescence started at day 60 which corresponds to DOY 192.

2.2 Electrical resistivity tomography (ERT)

We used a 3D inversion of the ERT data to image changes in soil bulk electrical conductivity (EC_b). A 'skip one' dipole-dipole scheme was used as described in Slater and Sandberg (2000). In order to assess the data quality, half of the measurements were reciprocal measurements (LaBrecque et al., 1996). A finite element method was used to solve the Poisson equation, which is the forward problem:

$$\nabla.(EC_b \nabla \phi) - \nabla.j_s = 0 \,,$$

(18)

where EC_b is the bulk soil electrical conductivity ($S.m^{-1}$), Φ the electric potential (V) and j_s the source current density ($A.m^{-2}$). No-flow boundary conditions were applied on all boundaries.

The inversion was carried out using an error-weighted, smoothness constrained Occam type algorithm. This means that the smoothest model distribution that fits the data to a specified error level was searched for. Given a set of N measurements of four-electrode resistance (R_i, i=1,2,…,N), minimization of the objective function, ψ, given by

$$\Psi = \left\| \mathbf{W}_\varepsilon [\mathbf{d} - f(\mathbf{m})] \right\|_2^2 + \lambda \left\| \mathbf{W}_s (\mathbf{m} - \mathbf{m_0}) \right\|_2^2 \,,$$

(19)

produces an image of M voxel electrical resistivities ρ_j (j=1,2, …,M), where m_j=-log(ρ_j), d is the data vector, f(m) is the forward model that relates the model m to the measured apparent resistivities, W_s is a smoothness operator, W_ε an error weighting matrix and λ is a regularization parameter which determines the amount of smoothing imposed on m during the inversion. More information on the implementation of the objective function is given in Garré et al. (2010). An unstructured tetrahedral mesh with grid refinement close to the electrodes was used to calculate the electric potential. After the inversion, the data where interpolated on a structured wedge mesh with voxel height of 6.95 cm to represent the variability of the electrical conductivity. For further details on the inversion we refer to Kemna (2000) and Guenther et al. (2006).

The data error (ε_i) was calculated as in Koestel et al. (2009). It was assumed that the data error can be approximated using a Gaussian error model which comprises an absolute resistance error component (p, Ω) and a relative resistance error component (q, -). These two components are then used in the

inversion algorithm to calculate the error (ε_i) of each single data point d_i as follows:

$$\varepsilon_i = \frac{p}{R_i} + q.$$

(20)

The approach considers the error model being spatially and temporally constant, in order to reduce the degrees of freedom in the error estimation. In order to keep the inversion equal for all timeframes, a constant p and q were used for the inversion and set to the maximum p and q of the whole timeseries.

2.3 Conversion of bulk electrical conductivity to water content

There are various existing pedo-physical models published in the literature which relate the measured bulk electrical resistivity to the factors influencing this resistivity: surface conductivity of the soil matrix, pore water conductivity, porosity of the soil, temperature and water content (e.g. Archie, 1942; Waxman et al., 1968; Revil et al., 1998). Waxman and Smits (1968) (W-S) developed such a pedo-electrical model based on Archies law (1942) for the use in geological applications. Recently, it has been successfully applied by several authors for quantifying transport processes in the unsaturated zone using ERT (e.g. Koestel et al., 2009; Koestel et al., 2009; Garré et al., 2010). For this study, we used a simplified empirical equation which is closely related to the W-S model:

$$EC_b = a.WC^n + b,$$

(21)

where a (S.m^{-1}), b (S.m^{-1}) and n (-) are fitting parameters. In this equation, the surface EC is not affected by the water content or solution EC. The parameters in the simplified W-S function can be thus still be interpreted in a physical manner: a is affected by the pore water conductivity and b by the soil surface conductivity, both in combination with the porosity (+- constant for a soil horizon, but can be different between horizons). There is no consensus on the

physical meaning of n for the full W-S model, but it may be related to e.g. the pore connectivity.

We derived in-situ pedo-physical models for each soil horizon based on the simplified W-S model using $EC_b(ERT)$-$WC(TDR)$ couples at the TDR probe locations during the experiment in the lysimeter. Here, $EC_b(ERT)$ is the mean of inverted bulk electrical conductivities in the measurement volume of a TDR probe. This resulted in four EC_b-WC couples for each measurement time and each of the five depths with TDR-probes. We grouped the EC_b-WC couples in four categories belonging to four different pedological horizons as observed in the field and fitted the simplified W-S model to the data in each of the four horizons:

$$WC(ERT) = \left(\frac{(EC_b(ERT) - b)}{a} \right)^{1/n} , \qquad\qquad (\,22\,)$$

where a $(S.m^{-1})$, b $(S.m^{-1})$ and n (-) are fitting parameters. At -44.5 one of the four TDR probes and at -119.5 two TDR probes were malfunctioning and discarded. By assuming one specific pedo-physical relationship for a soil horizon, we discard some of the variability present in the volume.

2.4 Monitoring root length density

To derive the root length density (RLD), images were taken once a week along the horizontal rhizotubes at ten different locations in each tube. One image encompasses a soil window of ca. 1.5 x 2.2 cm² and a viewing depth of 0.1 cm is assumed (Taylor et al., 1970; Sanders et al., 1978; Itoh, 1985; Steele et al., 1997). An example of successive images in tube 2 is given in Figure 15. The images were analysed using the open source software RootFly (Wells et al., 2009). We used the software to register the length, diameter, and color of the roots. From the root length in each image, the RLD can be estimated as the length of the roots per unit volume of the sample, being 1.5 x 2.2 x 0.1 cm³. The root length density at a certain depth was then the mean RLD of all the locations at that depth.
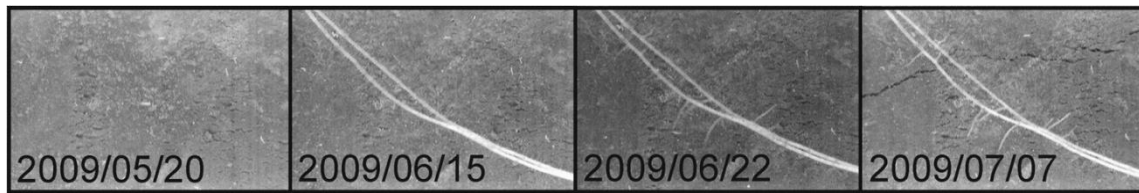
Figure 15. Four consecutive minirhizotron images at a depth of -44.5 cm and 38 cm from the lysimeter edge.

2.5 Total mass balance calculation

To understand the interaction of a crop and the soil moisture status, we estimated the different fluxes in and out of the soil. The weight (m, g) of the lysimeter was logged with an accuracy of 200 g. As no water was added to the soil during the experiment, changes in weight are equal to the sum of evapotranspiration (ET, m.day^{-1}) and drainage (D, m.d^{-1}). We used a glass vessel under suction to collect the effluent. Each time the effluent volume in the vessel reached 500 ml, the vessel was emptied and the time was logged. From the logged times and the known drainage volume, the drainage rate D was calculated.

The evaporation rate was estimated using the evaporation rate from a 5.8 cm deep water pan with a surface of 45 x 35 cm². The evaporation loss from the water pan was related to the reference evapotranspiration (ET$_0$) and the potential crop evapotranspiration (ET$_c$) by applying empirical coefficients (see Allen et al., 1998 for the exact equations). As such, ET$_c$ represents the sum of the crop transpiration (T) and the soil surface evaporation (E). In this experiment, E is supposed to be very small or even equal to zero, since the soil surface was very dry and the crop covered a large part of the surface. For each time step, we calculated the water loss from the difference between the initial water content and the water content at that time in the whole lysimeter volume. The water loss monitored with ERT was then compared to the weight loss of the lysimeter. This comparison allowed us to evaluate the performance of the ERT measurements and the pedo-physical relationship to establish a water balance

over time. The total correspondence of both measurements was tested with the root mean squared error (RMSE).

3. Results

3.1 In-situ calibration of ERT measurements

The EC_b-WC relationship for each of the four horizons in the lysimeter is shown in Figure 16. Table 5 shows the parameters of the simplified Waxman and Smits (W-S) model and the root mean squared errors (RMSE) of the optimized functions. The optimization was done by the minimization of a simple objective function (the RMSE) using the Nelder-Mead simplex method, an unconstrained nonlinear optimization algorithm. The pedo-physical relations vary considerably between the different soil horizons. This was expected since the surface conductivity is influenced by the clay content which is different across horizon, just like the porosity. In general, the simplified W-S model describes the data well for all horizons but the A_p. The course of measured EC_b-WC data in the A_p is more curved than the W-S fit. The rather bad fit in this horizon is probably due to the data at the end of the growing season. Starting from day 63 of the experiment (= DOY 195), the EC_b in the A_p horizon apparently started to increase with decreasing moisture content which leads to traces of EC_b-WC points (marked with two black arrows in Figure 16) deviating from the expected relation. In the B_t-horizon, more specifically the TDR probes at -44.5 cm depth, a part of the general course of the EC_b-WC couples cannot be described entirely by the W-S model (white arrow in Figure 16). Also in B_{v1} some deviations are visible; however these are less systematic than in the former horizons. These deviations from the fitted function can inflict small errors in the estimated water contents. As mentioned in the introduction, there is experimental evidence that the root biomass can alter the EC_b in both directions depending on the plant and root characteristics (al Hagrey, 2007; Werban et al., 2008; Zenone et al., 2008; Amato et al., 2009). For herbaceous plants, an increase of conductivity was reported. Since the observed anomalies in the general trend occur in the two upper TDR probes, they may be caused by the presence of a critical amount of roots in the measurement volume in

combination with a relatively dry soil. The increased EC_b for the same water content at the end of the experiment (in the dry range) might be caused by an alteration of the roots as the experiment was near to the end of the growing season. Using the minirhizotron images, we could observe that the roots were shrinking after day 60 (DOY 192) at -44.5 and -69.5 cm depth. This change of root structure as well as a change of physical contact between root and soil might explain the changing pedo-physical relationship. However, at -69.5 cm there is not a clear change of the pedo-physical relationship when the roots start shrinking, maybe because the soil is not that dry yet. In addition, as the soil dries out, the electrode contact might reduce so that the ERT measurement error and thus the noise on the ERT derived WC becomes larger for lower EC_b. This can also add deviations to the data in the dryer range.
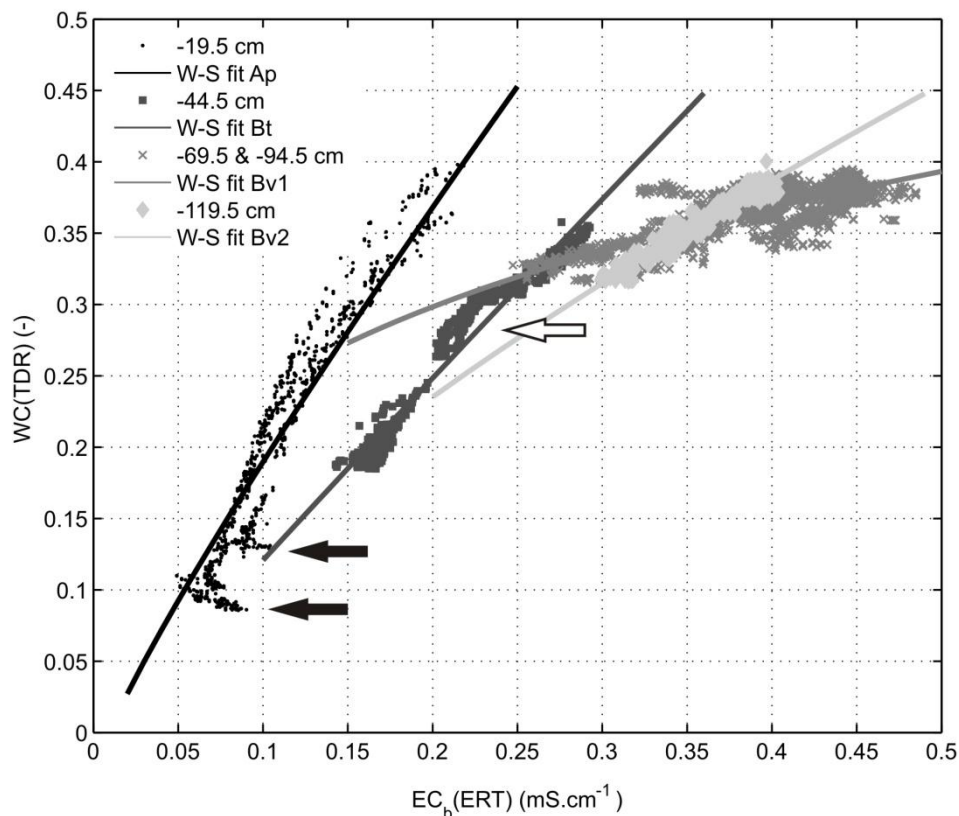
Figure 16. EC_b(ERT) -WC(TDR) couples and simplified W-S fits to these couples for four soil horizons. The black arrows indicate misfits starting in the 10th week of the experiment. The white arrow indicates a misfit in the B_t horizon.

Table 5. Parameters for the simplified W-S model for each of the four horizons.

	a (mS.cm^{-1})	b (mS.cm^{-1})	n (-)	RMSE (-)
A_p (> -40cm)	0.5861	0.00999991	1.1271	0.03
B_t (-40 - -70cm)	0.8037	0.00999531	1.0356	0.01
B_{v1} (-70 - -100cm)	12.0495	0.00999998	3.4314	0.01
B_{v2} (< -100cm)	1.5033	0.00166441	1.3996	0.005

3.2 Water content distributions and profiles in the lysimeter

Figure 17 shows 3-D water content distributions at three different days which were derived from ERT measurements. The irregular and non-horizontal isosurfaces of constant water content demonstrate the heterogeneity of the drying process in the lysimeter. In order to obtain these 3-D images of water content, the ERT-derived bulk electrical conductivity distributions were translated into water contents using the pedo-physical relations.
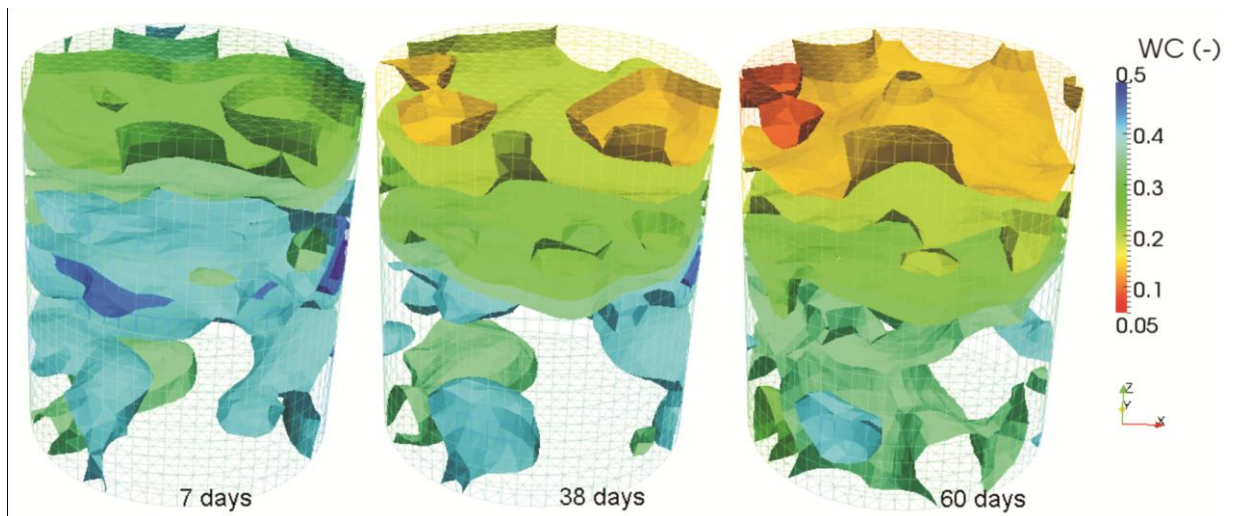
Figure 17. 3-D volumetric water content in the lysimeter after 7, 38 and 60 days. The surfaces are isosurfaces of equal water content. The distance between two isosurfaces is 0.05.

Figure 18 shows the bulk electrical conductivity in a vertical section of the soil column after 21 days. The black squares at the side of the sections represent the depths of the horizon boundaries as they were observed in the field. Each of the horizons is characterized by a different pedo-physical relationship (Figure

16). This differentiation adds structures to the moisture distribution in the lysimeter, which are not visible in the raw conductivity data.

Figure 19 depicts profiles of horizontally averaged bulk electrical conductivities and water contents for different times, as well as the standard deviation of the ERT-derived water contents. Unlike the EC_b profiles, the ERT derived water content profiles have important discontinuities at the soil horizon boundaries. The depths of these boundaries were not derived from ERT measurements but were based on observations in a nearby soil profile pit in the field. The shape of the boundary was approximated by a horizontal flat surface, since the resolution of ERT is not high enough to derive the real, probably slightly undulated boundary from the resistivity measurements. The abrupt changes in soil moisture were a consequence of the assumption that pedo-physical relation changed abruptly across the soil horizon boundary. Nevertheless, abrupt changes in water content may occur across boundaries of soil layers with different hydraulic properties.
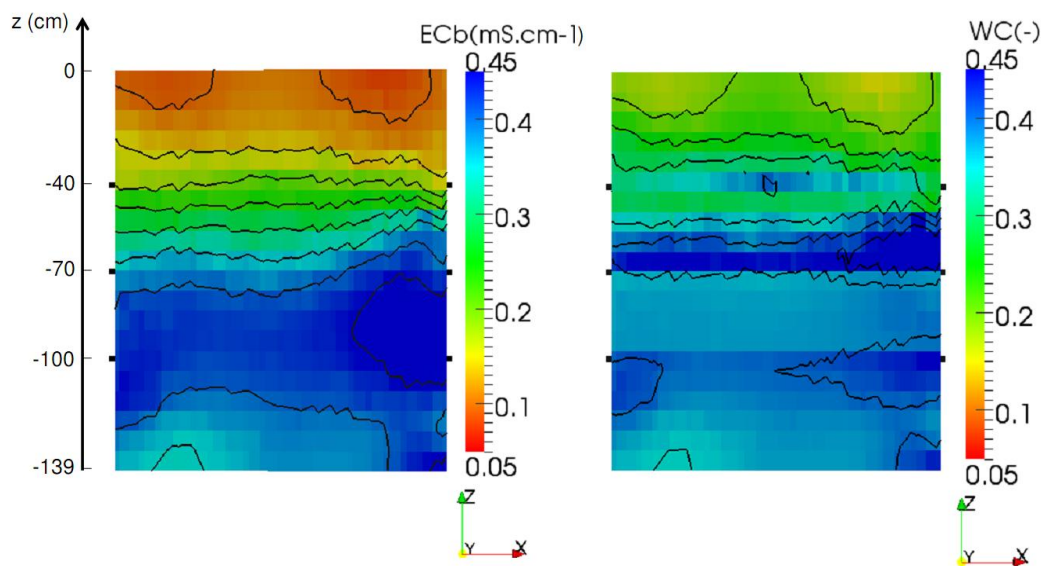
Figure 18. (right) Water content (WC, -) in a vertical section through the lysimeter estimated from ERT data 21 days after sowing. (left) Bulk electrical conductivity (EC_b, mS.cm^{-1}) in a vertical section through the lysimeter 21 days after sowing. In both plots contour lines are displayed for each interval of 0.05 cm^3.cm^{-3} for WC and 0.05 mS.cm $^{-1}$ for EC_b.

A validation of the exact location of the soil horizon boundaries, the shape of the boundary and the gradient of the pedo-physical relations across this boundary requires additional information. This information could be obtained potentially from other geophysical measurement techniques, such as georadar, which are sensitive to abrupt changes in water content or from process monitoring, such as transport experiments. Finally, it is of importance to notice that root development may also be affected by soil textural discontinuities leading to an additional uncertainty in the estimation of the soil moisture content at these boundaries.
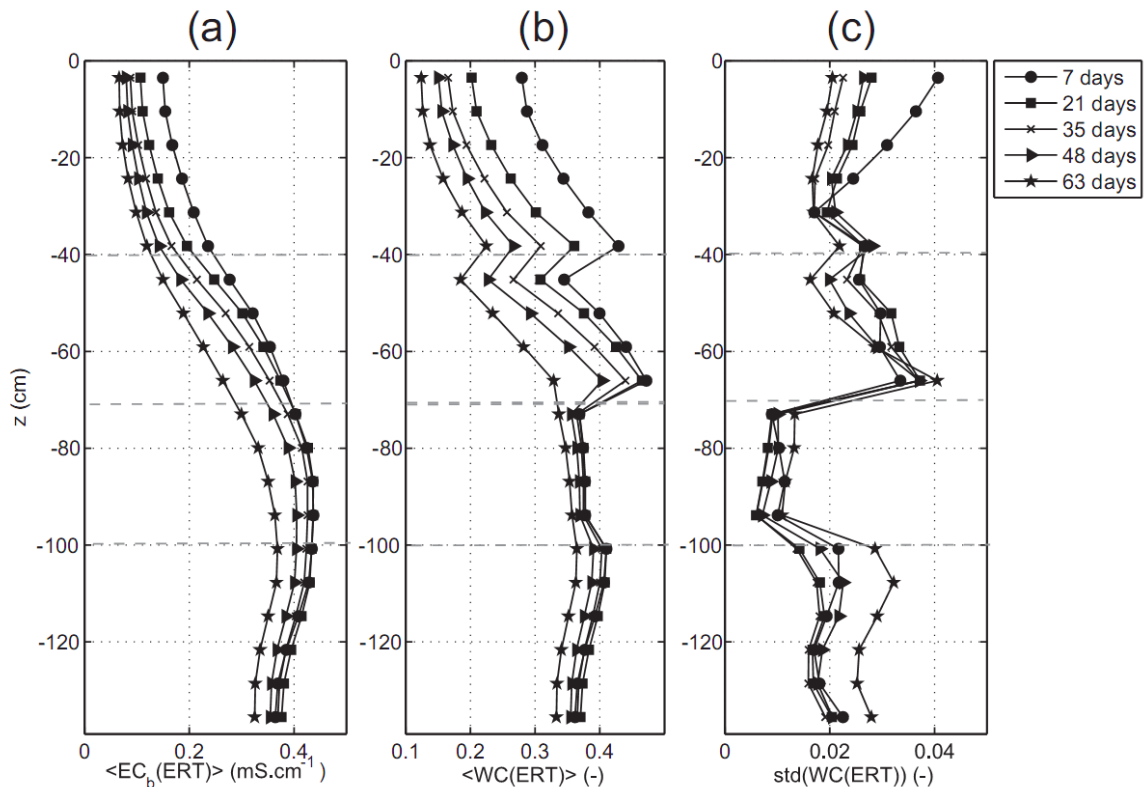
Figure 19.   (a) Mean bulk electrical conductivity (<ECb>), (b) mean (<WC>) and (c) standard deviation of the water content (std(WC)) from ERT measurements for all voxel layers in the lysimeter for t = 7, 21, 35, 48, 63 days after sowing.

By assuming one specific pedo-physical relationship for a soil horizon, we discard some of the variability present in the volume. To compare the results of ERT and TDR measurements, we averaged the ERT voxels in the TDR

measurement volume. Figure 20a shows the variability of the WC measured with the TDR probes against the variability of the WC from ERT in the measurement volume of the TDR probes for four depths. Soil moisture content measurements at a depth of -119.5 cm were not included as two out of four TDR probes did not function properly. The variability measured with ERT and TDR are in the same range. This indicates that applying one W-S model for a soil layer and using the smoothness constraint in the ERT inversion neither added nor removed variability artificially. The hatched area marks all standard deviations lying below the RMSE of the fitted pedo-physical relationship for the horizon under consideration. It becomes clear that only for the TDR probes which were closest to the soil surface the variability of the measured WC is high enough to validate the variability of the ERT measurements. However, the RMSE is a crude measure to evaluate a fit and bad correspondence in a small period of time can have a large influence on the overall RMSE of a fit. Therefore, this is a very strict criterion to evaluate the measured variabilities. In Figure 20b, the deviations of WC(TDR) and WC(ERT) from the mean WC(TDR) (<WC(TDR)>) and the mean WC(ERT) (<WC(ERT)>) at a certain depth are plotted against each other. A clustering of these deviations around the 1:1 line indicates that not only the total variability but also the patterns of the soil moisture variability are represented well by ERT. This can be represented quantitatively by a coefficient of determination (R^2), which is a measure for the fraction of the spatial variability of the TDR measurements explained by the WC derived from ERT measurements:

$$R^2 = 1 - \frac{\sum_{i,j}\left[\left(WC(ERT)_{i,j} - <WC(ERT)_j>\right) - \left(WC(TDR)_{i,j} - <WC(TDR)_j>\right)\right]^2}{\sum_{i,j}\left[WC(TDR)_{i,j} - <WC(TDR)_j>\right]^2} \qquad (23)$$

.

The R^2s for -19.5, -44.5, -69.5 and -94.5 cm depth are 0.37, 0.29, -0.34 and -0.97. The first two depths have an acceptable R^2. The variability and patterns of ERT and TDR correspond and the variability is high enough to be able to

distinguish patterns from measurement and fitting noise. Conversely, the coefficient of determination at -69.5 and -94.5 cm depth is negative. Additionally, the WC variability measured with TDR in these depths (< 0.01) was not high enough to be able to show the difference between measurement noise and real patterns. This can explain the R^2s. However, since we showed that ERT is capable of capturing the level of variability and the patterns of WC well in the top horizon, where the variability is higher, we assume that this will also be the case in the lower horizons when the soil dries out and the variability increases.

3.3 Global water mass balance analysis

An additional, indirect way to validate the water content profiles that were derived from ERT is to compare the total water loss obtained by weighing with the sum of the water loss in each voxel of the ERT mesh (Figure 21). The water loss from weight and ERT data agree very well. The RMSE between total water loss obtained by weight and the loss derived by ERT is 0.0032 cm³.cm⁻³. Notice that between t=42 days and t=48 days no data were available due to technical problems with data loggers. There are some small deviations visible between ERT and weight measurements. Between day 20 and 30, for example, the total water content estimated with ERT decreases more rapidly than the one from the lysimeter weight. This is probably due to deviations between the fitted W-S model in the A_p horizon and the data. Since we observed drainage only during the first 14 days of the experiment, the weight loss after day 14 is entirely due to evapotranspiration. During the first 14 days, the bottom flux decreased from 0.13 cm.day⁻¹ the first day over 0.05 cm.day⁻¹ already the second day and no drainage at day 15. The drainage was therefore negligible when compared with the total weight loss already after a few days.
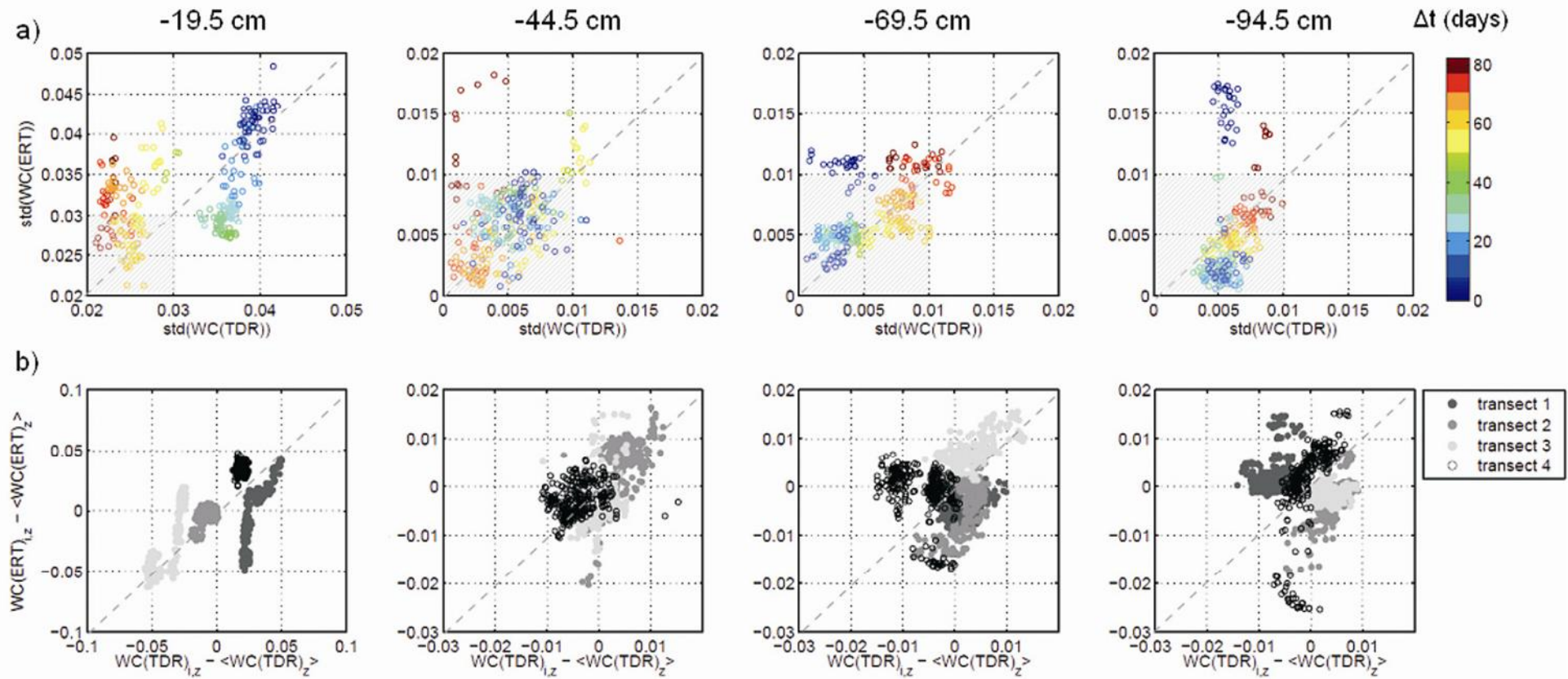
Figure 20. (a) Scatter plot of the standard deviation of the water content obtained by TDR and the one estimated by ERT. (b) The difference of the WC and mean WC for a depth for ERT against the same for TDR. The conductivities used to estimate WC(ERT) were the average of the voxels lying within the TDR measurement volume and therefore represent the mean WC (<WC(ERT)>) for that measurement volume.
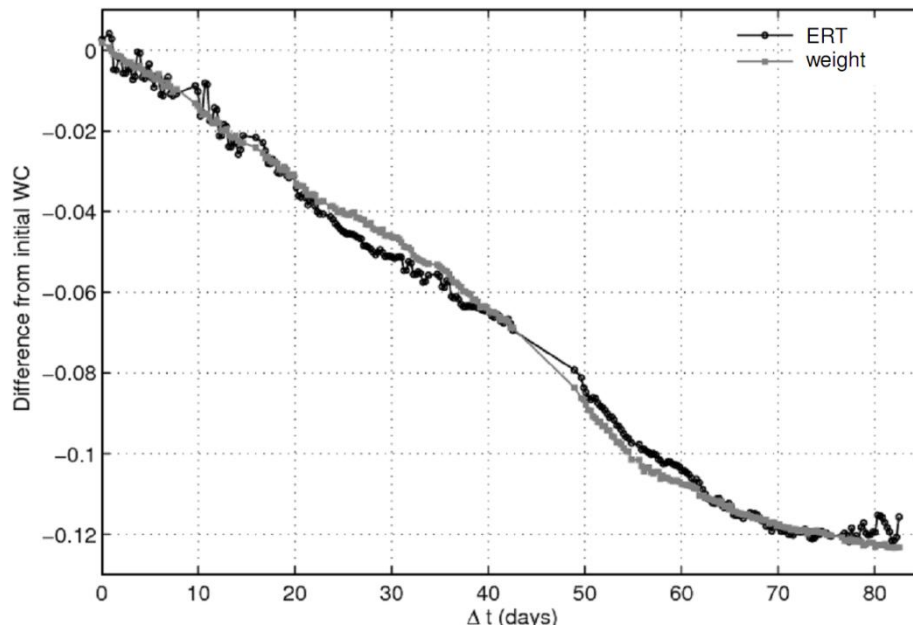
Figure 21. Mass balance of the lysimeter during the whole experiment.

3.4 Evolution of soil moisture variability at the voxel scale

The evolution of water content with time in two planes intersecting the column at -20 and -80 cm, respectively, are depicted in Figure 22. In general, the observed WC variability is much lower in the horizontal than in the vertical direction. The soil moisture pattern, i.e. the location of the driest and wettest regions in the horizontal cross section, at -20 cm changed during the course of the experiment. The observed patterns could not be linked visibly to the barley rows. Also at -80 cm depth, the soil moisture patterns changed during the experiment but the variation of soil moisture in time and space was smaller than in -20 cm depth as we already noticed looking at the TDR measurements.
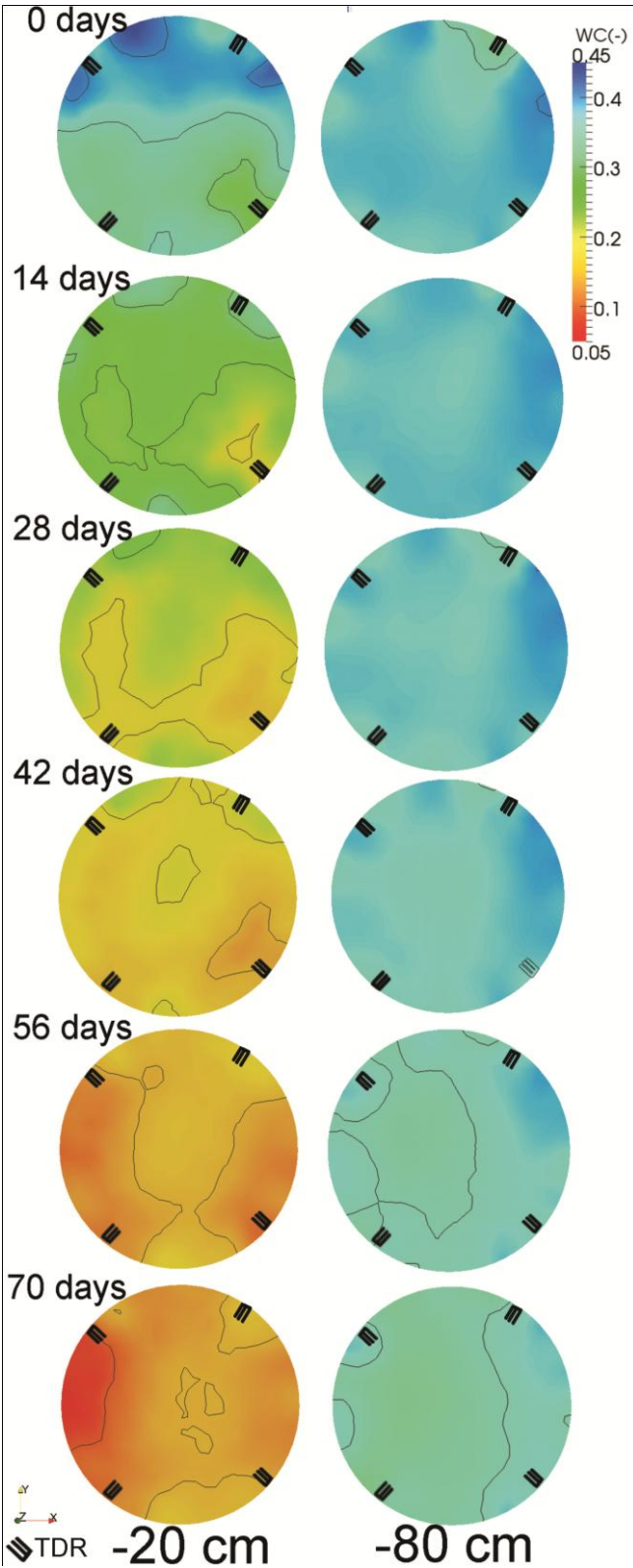
Figure 22. Horizontal section through the 3-D water content (WC, -) distribution in the lysimeter at depths -20 and -80 cm. The orientation of the barley rows is shown at the top of the image. The contours of [0.05,0.45] with steps of 0.05 are indicated with black lines.

Figure 23 shows the relation between mean water content for five different voxel layers of the soil column and the standard deviation of the WC at the voxel scale (h_{voxel} = 6.95 cm) for the measurement period. In the first and second depth, the variability is the highest when reaching an intermediate moisture content of ca. 0.3. For lower mean values the standard deviation decreases with decreasing mean WC. At the end of the experiment which corresponds to low mean average water content values, the variability of the water contents seems to increase again. As stated before, this might be an artefact caused by root effects on the soil electrical conductivity. In the lower voxel layers, the variability was still increasing at the end of the experiment and reached already a higher level than the maximum variability in the upper voxel layers.

Figure 19 shows that there are not only important gradients in the WC across horizon boundaries, but also gradients in variability. The fact that this variability is observed already at day 0 indicates that at least a part of the variability must be linked to the hydraulic properties of the different horizons, as Vereecken et al. (2007) indicated. The same authors showed that the relationship between soil moisture variability and mean moisture content for a bare soil is controlled by soil hydraulic properties, their statistical moments and their spatial correlation. As roots will develop differently in each horizon depending on soil hardness, soil water and nutrients availability (Bengough et al., 2006) and root uptake will also differ following soil and root hydraulic properties, this effect may be accentuated or decreased when soil is cropped. For a bare silty loam, Vereecken et al. predict a maximum standard deviation of 0.05. This soil type is comparable to the silty orthic Luvisol in this study, but the maximum standard deviation of our data set is higher. This discrepancy could be caused by spatially variable root water uptake and data noise.
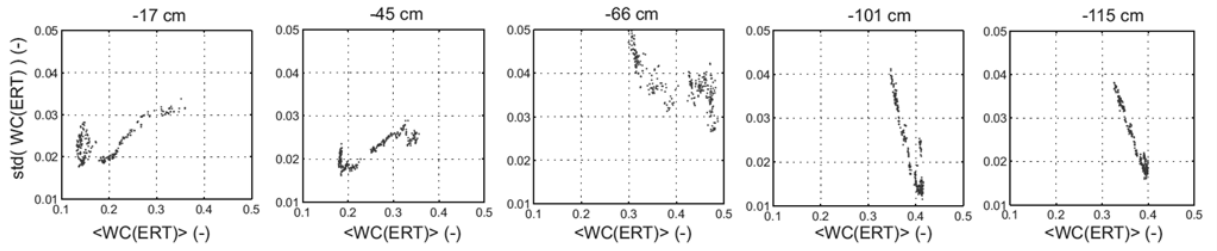
Figure 23. Standard deviation of the water content (std(WC(ERT))) in voxel layers at -17, -45, -66, -100 and -115 cm as a function of the mean of the water content (<WC(ERT)>) at the same depths.

3.5 Water depletion rate

Water depletion rates (DR, day^{-1}) in a horizontal layer of voxels were calculated from the change in average WC in the layer over a given time interval. The weekly rates were computed by moving a time window of a week day per day and taking the average over a week:

$$DR_j = \frac{\sum_{i=1}^{7}\left[\dfrac{\left(WC_{i+j} - WC_{i+j-7}\right)}{\left(t_{i+j} - t_{i+j-7}\right)}\right]}{7},$$

(24)

where j = [7, 14, 21,…,77] days. The total water depletion rate in the lysimeter DR$_{total}$ (m.day^{-1}) was obtained from integration of the average water depletion rates in the horizontal voxel layers over the lysimeter depth (Figure 24a). The water depletion rates in the voxel layers were then normalized by DR$_{total}$. These normalized mean weekly water depletion rates (nDR, m^{-1}) are displayed in Figure 24b as a function of time. Negative nDRs imply that the water content has increased over time at a certain depth. The line plot on top of the nDR evolution shows the resulting DR$_{total}$ calculated from the ERT data as well as from the weight data to validate the ERT-derived DRs.

The observed mean weekly DR$_{total}$ varies between 0.1 and 0.4 cm.d^{-1}. Due to the wet soil conditions at the start of the experiment, there was a considerable

water redistribution and internal drainage at the beginning of the experiment. This led to an increase in water content in the bottom half of the lysimeter. The first 20 days of the experiment, the front of maximum nDR stayed in the upper soil horizon and moved down gradually afterwards. From day 19 until day 32, the maximum nDR is at 0.4 m depth and a decrease of nDR can be observed at the top of the column. The decrease in nDR in the top soil may be the effect of a lower ET during this period in combination with water redistribution towards the top soil layer. The nDR increased again at the top of the lysimeter together with a slightly higher ET from day 35 until day 45. From day 45 until day 55, the ET is considerably larger than in the previous periods, but the water in the top soil is depleted so that the maximum nDR moves downwards. This could indicate that stress was occurring in a part of the root zone, causing the plant to adjust its rooted volume or the effectiveness of already existing roots. Potential ET rates were calculated from measured water pan evaporation rates (Allen et al., 1998). At the beginning of the experiment, the DR_{total} were higher than the calculated potential ET rates. This was due to an underestimation of the bare soil evaporation in the Allen et al. (1998) procedure. From day 25 until 58, the potential ET rates corresponded well with DR_{total}. The decrease in ET rate between day 50 and day 58 cannot be linked with water stress but is rather due to different meteorological conditions. Therefore, downward movement of the DR_{total} from day 50 due to water shortage in the top soil did probably not lead to a water stress at the plant level. From day 60, the measured DR_{total} was smaller than the calculated potential evaporation of a full grown barley crop. After day 60, crop senescence started and the transpiration rate reduced. The senescence of the barley in the lysimeter was not caused by the soil water regime in the lysimeter and cannot be linked to a water stress of the plants, since the barley in the field surrounding the lysimeters entered senescence around the same time.

Significant water loss below 70 cm in the B_v horizons occurred only after 60 days. Before the nDR front moved into the B_v horizon, it seemed to be blocked at the upper boundary of the B_v horizon. In the field we observed that these

horizons were harder to penetrate and this might have retarded root growth in the early stage of the experiment. Starting from day 61, there is a rather high nDR in the B_{v2} horizon, but there are almost no roots observed at -119.5 cm. This nDR may thus be due to vertical water redistribution from the deeper part of the soil to the root zone.

3.6 Relationship between root length density and water depletion rate

The root length density (RLD) and the DR profiles at different times are shown in Figure 25. We observed that a rather unusual RLD profile emerged in the soil column. At the end of the experiment, the highest density was observed at -70 cm, which was deeper than we expected. It must be noted that our first RLD measurement was at -19.5 cm. Therefore it is possible that there was first peak of RLD near to the soil surface which could not be observed. The measured RLD distribution is probably related to the WC distribution in the column and to the fact that the lysimeters received no water during the entire growing season. While the top soil dried out, the root length density in the deeper soil horizons increased causing the nDR to move downwards.
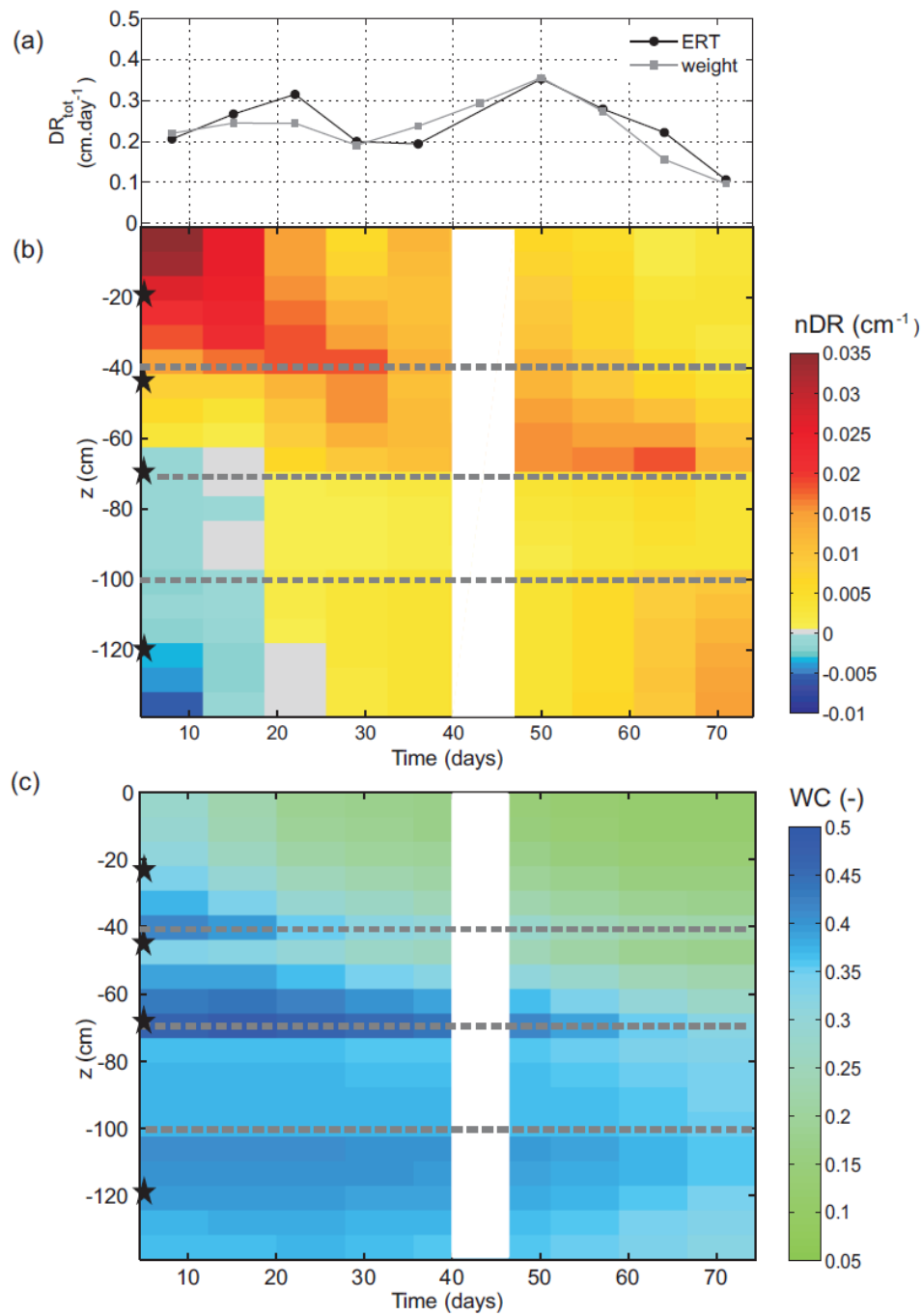
Figure 24. **(a) Total weekly water depletion rate (DR$_{tot}$) estimated by ERT and weight measurements; (b) normalized local water depletion rates (nDR) as a function of depth and time; (c) volumetric water content (WC) measured with ERT as a function of depth and time. The black stars indicate the rhizotube locations. The grey dashed line indicates horizon interfaces.**
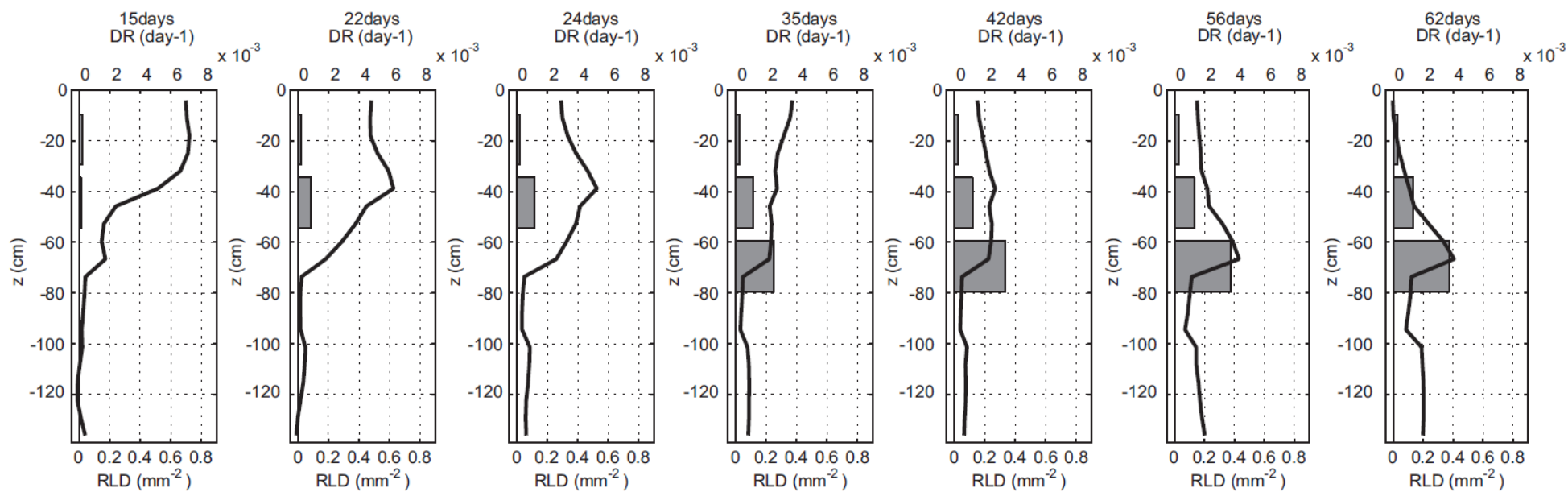
Figure 25. Water depletion rates (DR, black) and root length density (RLD, gray) profiles after 15, 22, 24, 35, 42, 56 and 62 days.

4. Conclusions

We validated 3-D ERT-derived moisture contents in a cropped, undisturbed soil column using a global mass balance method and a comparison between and ERT derived local variability of the soil water content. The global water mass balance of the soil column could be reproduced well by the ERT method. The standard deviation and patterns of the local water content within horizontal cross sections of the lysimeter that were measured with TDR could be reproduced in the top horizon. However, the observed variability was small and in the lower horizons even too small to be able to distinguish it with certainty from noise. These two observations are an important result of the quantitative evaluation of the ERT method. Our analysis sustains its value as a tool to monitor and quantify 3-D water content patterns and water content changes in a layered soil.

We have shown that a horizon-specific in-situ calibration of the ERT measurements was necessary to convert the bulk electrical conductivity to water content. However, more research is needed to understand and predict the effect of roots of herbaceous plants on the measured electrical conductivity, since we observed a change in the pedo-physical relationship probably due to root shrinkage at the end of the growing season. Additionally, knowledge about the location and shape of soil horizon boundaries proved to be important to improve the result of ERT-derived WC and estimated water depletion rates, especially at interfaces between horizons.

ERT proved to be a suitable technique to observe soil water dynamics at the decimetre scale and a promising tool to unravel the relationship between soil redistribution and root water uptake. We observed that the variability of the obtained water content distribution increased during drying until a threshold of water content was reached and then decreased again in the top horizon. In the lower horizons, the maximum WC variability was not yet reached. The observed variability was higher than what was expected from the literature which may be

due to spatially variable RWU. The spatial patterns of wetter and drier regions in a horizontal cross section of the lysimeter changed during the drying process. However, this needs further investigation, since in the literature both an increase and a decrease of soil moisture variability due to RWU are reported (e.g. Teuling et al., 2005).

Finally, a rather unexpected RLD profile with the maximum root length density at -70 cm depth was observed. This observation must be carefully interpreted, since the RLD was only measured at four depths. Nonetheless, it points out that the root architecture in a layered soil can depend on soil characteristics and dynamically adapt to soil moisture states in the soil profile. Our results indicate that this adaption can be a compensation mechanism for local water shortage in the soil profile.
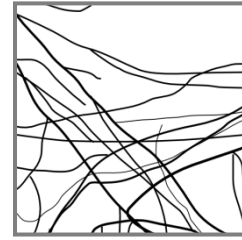
Parameterizing the Root System Development of Summer Barley using Minirhizotron Data[3]

Abstract.

Increasing computer power favors the use of complex mesoscopic models to predict root water uptake. These models explicitly consider the 3-D root architecture and root growth of a plant and may have variable hydraulic potentials in both soil and root. However, a lack of high-quality data to calibrate and validate these models remains, especially for non-woody plants in undisturbed, layered soils. We reconstructed the root system architecture for barley growing in an undisturbed lysimeter using minirhizotron data at four depths. The evolution of the number of roots in a minirhizotron image with time was used to optimize the root architecture model RootTyp (Pagès et al., 2004). We adjusted a simple architecture to the data, which contained only long primary roots starting from the seed and small, regularly spaced secondary roots. However, the result was not satisfying since the simple model could not reproduce an increasing root number with depth. The model could be improved making the branching and root elongation horizon-dependent and by making reiteration of root tips possible. Reiteration is an alternative form of branching, where secondary roots can become as long and thick as primary roots. However, minirhizotron data do not contain enough information to restrain the parameters governing these processes. Therefore, different experimental techniques should be combined to achieve a better model result.

---

[3] Adapted from: Parameterizing the root system development of summer barley using minirhizotron data. *To be submitted.* Garré, S., Pagès, L., Javaux, M., Vanderborght, J., Vereecken, H.

1. Introduction

Predicting soil-root interactions at the lysimeter and field scale remains a big challenge. Very often the complexity of the root system architecture and its dynamics, the lack of detailed data, as well as a lack of computing power caused researchers to decrease the problem dimensionality from 3-D to 1-D or to simplify the representation of the root system in such a way that solutions of 2- or 3-D water flow and solute transport equations could be derived. As a consequence, many modeling approaches co-exist to predict root water uptake, differing mainly in the spatial scale at which simulations are performed and in their dimensionality. The existing approaches can be classified within three categories (see Schröder, 2009). Firstly, there are microscopic models in which the uptake is modeled as a flux across the soil-root interface (Gardner, 1960; Cowan, 1965; de Willigen et al., 1987; van Lier et al., 2006). The magnitude of this flux depends on both soil and root properties. A second group contains the macroscopic models, dealing with uptake as an extraction or sink term in the soil water flow equation (Molz, 1981; Hopmans et al., 2002; Feddes et al., 2004; Green et al., 2006). This approach represents the root system by its spatial distribution (e.g. the root length density (RLD)). In these models, the sink can depend on the demand for water and nutrients by the plant, the root length density and the water and nutrient availability in the soil. Finally, there are hybrid models, using a mechanistic sink term approach to model the flow between soil and root, but integrated on the whole root architecture. Doussan et al. (2006), Javaux et al. (2008) and Schneider et al. (2010) developed such models. A mechanistic sink is an extraction term depending on microscopic water flow from the soil to, and through, individual roots.

Since computer power increased dramatically over the last decades more and more attention has been paid to the hybrid models (e.g. Javaux et al., 2008; Roose et al., 2008; Schröder et al., 2008; Draye et al., 2010; Schneider et al., 2010). These models require more detailed information about the root system than the lumped 1-D models, which require 'only' information about the root

length density. They consider the 3-D root system architecture (RA) explicitly and may consider variable hydraulic potentials in both soil and root. This allows to predict soil water depletion around the roots and the spatial distribution of water uptake in a soil profile, as well as water potentials in the root. Nonetheless, the lack of data to calibrate and validate root and soil water flow parameters and the root architecture of these models remains. Because of that lack of knowledge, inverse modeling appears as an appealing methodology to characterize the parameters of a root system development model and concurrently root water uptake models.

There are two reasons for this persisting lack of data for root architecture model calibration or direct parameter estimation. First of all, techniques to extract information on root system architecture and/or growth are extremely time-consuming and thus expensive. Secondly, in a real, undisturbed soil, it is almost impossible to assess the 3-D root system architecture of mature plants without destroying it. There are techniques though, that can be used for 3-D non-invasive monitoring: e.g. X-ray tomography (e.g. Tracy et al., 2010) and NMR (Pohlmeier et al., 2008). However, the problem with these techniques is, that they are restricted to small soil cores (with limited length) and to singe plants. This makes it unfeasible to follow root growth in a natural environment and study the interactions taking place. Typical traditional techniques in field soils are soil cores, observation of trench walls, ingrowth cores and root excavation (see Smit et al., 2000 for more information on sampling strategies). The only method to assess the dynamics of the root system which can be used in a lysimeter or field soil is the minirhizotron technique. Minirhizotrons are are clear glass or plastic tubes that are installed in the soil under plants. Using an endoscope, pictures can be taken of the roots growing along the outside walls of the tubes. By taking repeated images through time, the progress of the roots can be followed as they appear, mature and die. However, rhizotubes represent only a portion of the rooted volume and if they are installed horizontally, information will only be available at some discrete depths. Moreover, it has been shown that a rhizotube surface always acts as an altered environment for

the roots, possibly changing root length and other architectural characteristics (Bragg et al., 1983; Upchurch et al., 1983; Levan et al., 1987; McMichael et al., 1987; Vos et al., 1987; Parker et al., 1991). However, there are two important advantages to the minirhizotron technique: firstly, the method can be used to follow the evolution of the root arrival time in situ; secondly, root growth is not disturbed, until the roots reach the rhizotube. The number of roots arriving at the rhizotube as a function of time at a certain depth contains reliable information on root growth (e.g. Parker et al., 1991; Smit et al., 2000). When these root growth curves are assessed at several depths, minirhizotron data may be used to calibrate a simple RA model.

In this paper we will therefore (i) explore the value of the information that can be extracted from minirhizotron images in horizontally installed rhizotubes at four depths; (ii) identify parameters of the root architecture (RA) model RootTyp (Pagès et al., 2004) which can be estimated from this information together with expert knowledge and (iii) assess the optimal parameters for the root system architecture model of summer barley (*Hordeum vulgare L.*).

2. Materials and methods

2.1 Lysimeter and minirhizotron set-up

We excavated two undisturbed soil monoliths using a large PVC column (height=150 cm, inner diameter=116 cm) from intensively used arable land near Merzenhausen (Germany). The soil was classified as an orthic Luvisol (FAO/ISRIC/ISSS, 1998). Four soil horizons were identified: Ap (0-40 cm), Bt (41-70 cm), Bv1 (71-100 cm) and Bv2 (>100cm). Earthworm burrows were abundant down to more than 150 cm, although few direct connections to the soil surface exist, because of frequent plowing (Burkhardt et al., 2005). Root channels were generally <10 mm (with the maximum diameter resulting from tap roots of sugar beet) and were found up to a depth of 1.2 m. More information on the soil profile and equipment can be found in Part II: Experimental set-up.
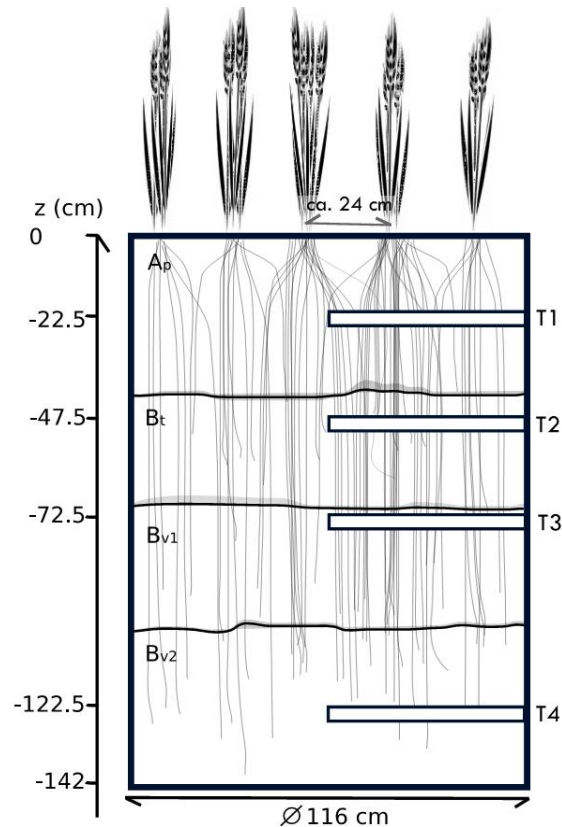
Figure 26. Scheme of lysimeter set-up with barley (lysimeter S1).

Four rhizotubes were installed horizontally at the side of the lysimeter at -22.5/19.5, -47.5/44.5, -72.5/69.5 and -122.5/119.5 cm depth for S1/S2 respectively. The installation was performed after the lysimeter excavation using a home-made, steel soil auger with a diameter which was slightly smaller than the rhizotube outer diameter to avoid voids between tube and soil. The rhizotubes were made of Plexiglas; were 60 cm long and had a diameter of 5.72 cm. A BTC2 video microscope (Bartz Technology Corporation, Carpinteria, CA, USA) was used to monitor the root growth on the outer walls of the tubes. Figure 26 shows an overview of the experimental set-up.

In each tube and for each sampling time, ten images were collected (image size: 2.2 cm x 1.5 cm); five at the left side of the tube and five at the same location at the right side of the tube. The images were not adjacent (5 cm apart) and were analyzed with the open source software RootFly (Wells et al., 2009). Figure 27 shows the principle of the image analysis. In a minirhizotron image,

roots were characterized by a line along their course and a circle, representing the root length and the root diameter respectively. The lines were prolonged and the diameter adjusted as the roots in the image grew. We made a distinction between primary and secondary roots based on their length, diameter and degree of ramifications. Primary roots are longer and have a bigger diameter than secondary roots. They may have ramifications, whereas secondary roots do not have ramifications. The number of circles, together with their label 'primary' or 'secondary' in an image, is thus the number of primary and secondary roots identified in the image. The number of roots in the rhizotube images was then extrapolated to the whole rhizotube. For this extrapolation, we assumed that all primary roots passing through a virtual rhizotube volume would be observed if the entire tube would be scanned through a viewing window with the same height as the images we used on the left and right hand side of the tube. Normalizing the number of roots in a rhizotube by the horizontal cross section of the rhizotube allows comparing data from rhizotubes with different length and/or diameter. If only a part of the tube length is scanned by images at the two lateral sides of the tube, the horizontal cross section that is scanned, $A_{cross,scan}$ is:

$$A_{cross,scan} = D_{tube}\frac{\sum_{N_{im}} b_{im(i)}}{2} = r_{tube}\sum_{N_{im}} b_{im(i)} \; , \tag{25}$$

where D_{tube} and r_{tube} are the tube diameter and radius, respectively, $b_{im(i)}$ is the width of the ith minirhizotron image along the tube, and N_{im} the number of images taken in one tube. The inferred normalized number of roots ($Nr_{norm}(T_i)$ L^{-2}) for a rhizotube T_i is:

$$Nr_{norm}(T_i) = \frac{\sum_{N_{im}} Nr_{im(i)}}{A_{cross,scan}} \; , \tag{26}$$

where $Nr_{im(i)}$ the number of roots counted in image i.

The evolution of Nr_{norm} with time represents a root arrival curve at a certain depth. The sigmoid arrival curve of the number of primary roots at each tube, $Nr_{norm}(T_i)=f(t)$, was characterized using three parameters: the time at which 50% of the final amount of primary roots was reached ($t_{50\%}$), the maximal amount of primary roots intercepted by each tube (Nr_{Max}) and the slope of the growth curve between $t_{80\%}$ and $t_{20\%}$ (SLP) (see Figure 27).
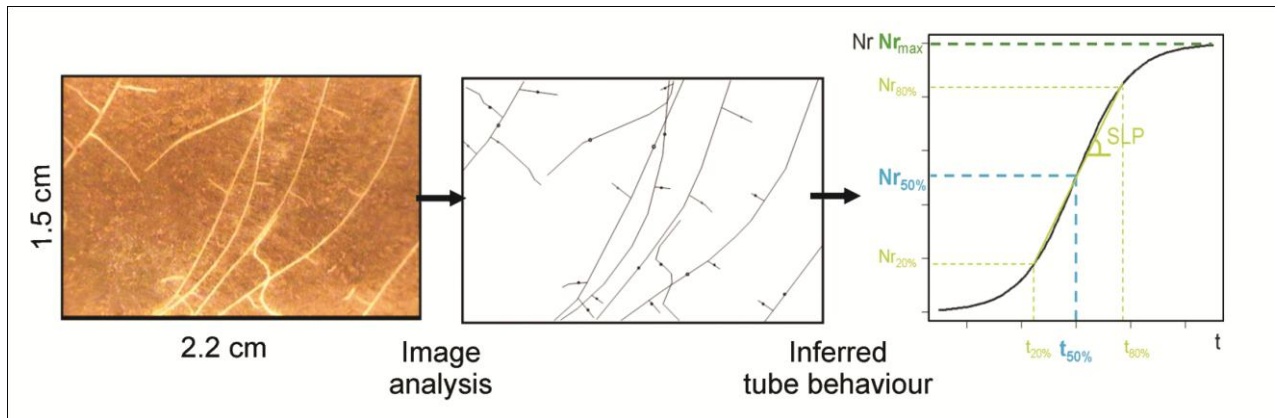
Figure 27. Minirhizotron image and scheme of typical image analysis. The circles in the central figure represent a single root and its diameter. From the counted circles, which represent primary roots, in all images taken in a rhizotube, the normalized number of roots in a rhizotube, Nrnorm (cm^{-2}) (Eq. 2) was calculated. A plot of Nrnorm versus time represents a root arrival curve which was characterized by three parameters: $t_{50\%}$, Nr_{Max} and SLP. (see text)

In the beginning of the experiment, the volumetric water content in the bare column varied with depth between 0.30 and 0.45 (Garré et al., 2011). We sew the summer barley (*Hordeum vulgare L.*) in parallel lines ca. 24 cm apart on DOY 132. We made small lines of ca. 2 cm deep, spread the barley seeds (ca. 0.6 seeds/cm) in these lines and covered them with soil. The soil did not receive any additional water until DOY 209. To estimate the plant density, the number of plants was counted just after emergence and at the end of the growing season using a picture of the lysimeter surface. In both lysimeters the photograph counts resulted in approximately 200 plants or 0.019 plants.cm^{-2} (S1: 198, S2: 217). It must be noted that these numbers are somewhat uncertain since it was not always straightforward to distinguish if we saw one or two plants. This counting method is however accurate enough to get an

estimate of the population density and compare it with densities that are typical for agricultural practice.

2.2 Root system architecture model

We used the generic model RootTyp (Pagès et al., 2004) to simulate the root system architecture of summer barley in the lysimeters. The root system of a single plant in this model is extended and branched by a set of root tips taking various states (modeled by root types). Processes like root elongation, growth direction and branching density are known to be dependent on the soil and the root tips can therefore also interact with it. Each root tip extends an axis (axial growth) and can develop lateral axes (branching). Figure 28 shows a scheme of how the root system is modeled in RootTyp.
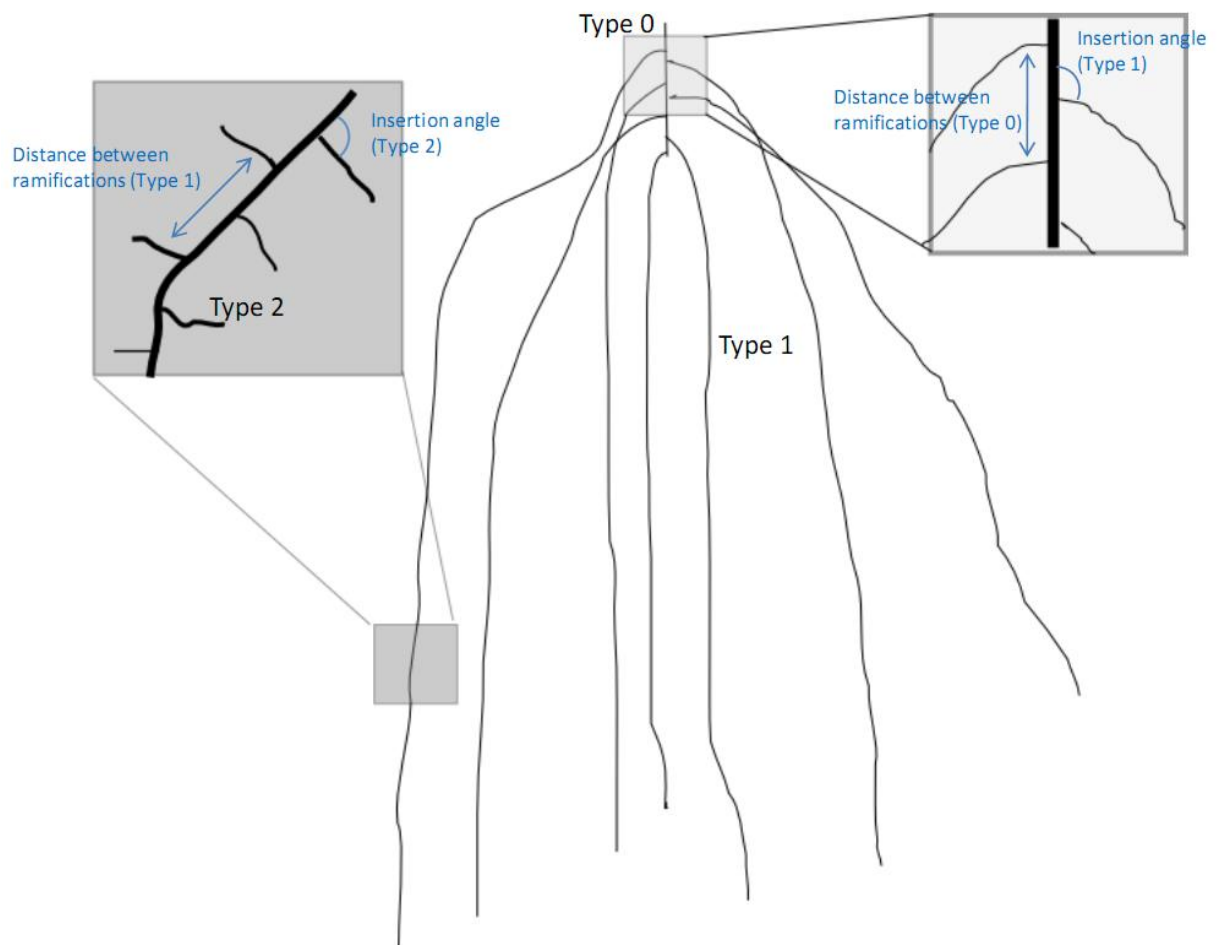
Figure 28. Scheme of root system build by a set of root tips taking various states as in RootTyp.

The root system starts with a small segment of type 0, representing the base of the shoot system. This segment has a certain amount of ramifications (Nr_{Prim}), which is defined by the length of this segment and the distance between the ramifications. The ramifications represent the primary roots. The growth velocity and length of the 0th order segment, together with the distance between the ramifications control the emission rhythm of the primary roots. For cereals, the emission generally starts a few days after the germination and may continue until flowering (Picard et al., 1985; Doussan et al., 2003; Draye, personal communcation August 2010).

The insertion angle of ramifications (α) is drawn from the normal distribution with mean <α> and std(α). The root segments grow according to

$$l = L_{max}(1 - e^{-v_{INIT} \cdot \frac{Age}{L_{max}}}),$$ (27)

with l, the length of the root; Age, the age of the root; L_{max}, the asymptote of the root length and v_{INIT}, the initial root growth velocity. v_{INIT} and L_{max} are drawn from normal distributions with mean <v_{INIT}>, <L_{max}> and standard deviations std(v_{INIT}), std(L_{max}). If L_{max} is set very high, the root growth will be linear and equal to v_{INIT}. At each time step, the growth direction of a root tip is updated, taking the gravitropism into account. In case of a positive gravitropism (downward), the new direction is calculated by

$$\mathbf{DI_{new}} = \mathbf{DI} + (c_{grav}.\Delta l.\mathbf{G}),$$ (28)

with DI_{new}, a vector representing the new direction; DI, a unit length vector representing the current direction; G, a vertical, normalized vector oriented downward; Δl, the elongation during that timestep and c_{grav}, the intensity of the gravitropism (0 means no gravitropism). More information on the methodology of RootTyp is given in Pagès et al. (1989,2004) .

2.3 From root growth curves to root architecture parameters.

Combining observed root growth curves and root architecture modeling, we will address the following questions: 'Which parameters of the root growth model RootTyp may be derived from root growth curves that are observed at different depths using minirhizotron images?' and 'What can we learn about the root growth in the two lysimeters from an optimized root architecture development model based on observed root growth curves?' The first question is directly linked to the question how different parameters of the root development model influence characteristics of the root arrival curves and the change of these characteristics with depth. The second question relates to the processes we can identify as being determining for the root growth in the lysimeters under investigation.

In order to address both questions, we simulated an ensemble of seven rows of barley plants with a distance between the rows of 24 cm. The individual barley plants were equally spaced in the row and the distance between two plants was 2 cm. This corresponds to the distribution in the real lysimeters with the counted number of plants and assumed that all plants were equally distributed over the rows. For a specific simulation, a parameter set was drawn for each individual root from the specified parameter distribution. This results in an ensemble of different plants.

The emission of primary roots was equal for all simulations. We assumed that five days after germination the primary roots started to be emitted and the emission continued until 22 days after germination. These values lie within the timespan we can expect for cereals (Picard et al., 1985; Wahbi et al., 1995; Doussan et al., 2003; Draye, personal communication) and are not are not measured during the experiment. However, it is important to fix this value for all simulations, since the emission rhythm may determine to a big extent the slope of growth curves of roots intercepted at a rhizotube. This influence depends on the period during which the 0th order segment grows in comparison with the duration of the plant growth. If the 0th segment stops growing already at an early

stage, the slope of the arrival curves will mainly be determined by the variance of the growth velocity and the insertion angle of the roots. If the 0th element grows during the entire period of the plant growth, roots will be emitted all the time and the slopes of the root arrival times will hardly change with depth. To be able to compare the influence of other parameters in the model between simulations, the emission rhythm needed to be fixed in advance by doing an intelligent guess based on expert knowledge.

The model performance was evaluated by comparing the characteristics of the measured growth curves with those of the 'virtual' root growth curves at virtual rhizotubes at the same location as in the real monoliths. The normalized virtual growth curves where calculated using two assumptions: (1) the number of roots counted within the volume of a virtual rhizotube equals the number of roots hitting a real rhizotube (see Figure 29a); (2) the total number of roots hitting a rhizotube can be inferred from non-adjacant rhizotube images with a limited range (see Figure 29b). The validity of the second assumption was evaluated conducting virtual sampling virtual rhizotubes in the best simulation. This test also allowed us to estimate the uncertainty measured root growth curves. The validity of the first assumption could not be checked.
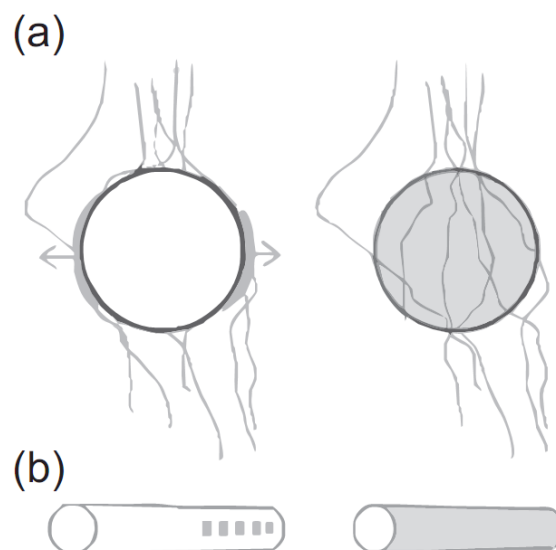
Figure 29. Assumptions for comparison between measured and simulated growth curves.

The optimization of the RA model was limited to the parameters Nr_{Prim}, $<v_{INIT}>$, $std(v_{INIT})$, $<\alpha>$ and $std(\alpha)$ for which we first defined possible parameter variations. The maximum length (L_{max}) of the primary roots was set very large in order to let them grow during the whole growing period. The boundaries of these intervals were extracted from literature (Bragg et al., 1984; Hansson et al., 1987; Hansson et al., 1992; Heeraman et al., 1993; Bingham et al., 2003; Kohl et al., 2007; Hargreaves et al., 2009) and personal communication (Draye, August 2010). $<v_{INIT}>$ was varied between 1-5 cm.day^{-1} and its standard deviation between 0.01-0.7 cm.day^{-1}, Nr_{Prim} was varied between 10 and 60. The optimization was started with three possible values of $<\alpha>$ and three possible values for $std(\alpha)$ within their defined realistic variations. The middle value of the insertion angle (α) of the primary roots and its standard deviation was chosen to produce plants of which 95% of the roots stayed within a circle with a diameter of 40 cm at 30 cm depth and occupied this space regularly. This resulted in a start value $<\alpha>$ = 2.83 rad and $std(\alpha)$= 0.171 rad. The other two angles represented plants with a slightly broader ($<\alpha>$ = 2.44 rad) and slightly narrower ($<\alpha>$ = 2.88 rad) root system. The parameters which are fixed for all simulations are: the type of tropism and its intensity, the sensitivity to mechanical resistance, life time of the roots and the probability of transformation of a root (see Appendix 1 and 2 for the values of these parameters).

In order to increase the computation effort of the optimization and to reduce cross-effects of parameters, we explored the parameters in a sequential way. Step by step, each of the model parameters was varied while keeping the others fixed to their initial or optimized values. We observed the changes in the growth curves and their characteristics $t_{50\%}$, Nr_{Max} and SLP. This was first done for v_{INIT}, then for Nr_{Prim}, after that for $std(v_{INIT})$ and finaly for $<\alpha>$ and $std(\alpha)$. For each step of this strategy, a decision criterion was defined according to the influence of the parameter on the related growth curve characteristics. The use of multiple criteria allowed us to separate the effect of parameters on different characteristics of the root growth curve. An example of the optimization criterion for $t_{50\%}$ is given below:

$$\min\left[\mathrm{RMSE}(t_{50\%}) = \sqrt{\sum_{i=T1}^{T3}(t_{50\%}(T_i, simulated) - t_{50\%}(T_i, measured))^2}\right].$$ **(29)**

The best v_{INIT} minimizes the RMSE($t_{50\%}$). The optimum growth velocity v_{INIT} emerged clearly from the simulations with varying v_{INIT} for the two extreme <α>'s. The simulations for the middle <α> were therefore already restricted to the optimum v_{INIT}. After having fixed v_{INIT}, the best Nr_{Prim} was defined as the one which minimizes RMSE(Nr_{Max}). This was tested for a series of simulations with fixed v_{INIT} and different values for <α>, std(α) and std(v_{INIT}). The third criterion determined the optimum std(v_{INIT}) as the one resulting in the lowest RMSE(SLP). We let std(v_{INIT}) vary for the selected <v_{INIT}> and <Nr_{Prim}> and for the several values of <α> and std(α). Once these three parameters were determined, we evaluated the different cases of <α> and std(α) which were simulated (<α> = 2.88, 2.44 and std(α)= 0.0171, 0.045, 0.085). The best <α> and std(α) were chosen using the RMSE of the total growth curve as a function of time t as a decision criterion:

$$\min\left[\mathrm{RMSE}_{total} = \sqrt{\sum_{i=T1}^{T3}\sum_{t=0}^{t_{end}}(Nr(T_i, t_j, simulated) - Nr(T_i, t_j, measured))^2}\right].$$ **(30)**

This last step was needed since <α> and std(α) have only a small influence on SLP, just like std(v_{INIT}), and a very small influence on Nr_{Max}, which is also affected by Nr_{Prim}. As the major influence on the form of the growth curves is coming from <v_{INIT}>, Nr_{Prim} and std(v_{INIT}), we first optimized these parameters. In total, we conducted 107 simulations. An overview of the parameter combinations which were used to adjust a simple RA to the data of S1 and S2 is given in Appendix 3.

2.4 Multi-objective optimization

The best realization for each of the lysimeters was determined using all criteria (RMSE($t_{50\%}$), RMSE(Nr_{Max}), RMSE(SLP) and the total RMSE) . We gave each

simulation a rank for each of the four criteria. The simulation with the lowest sum of ranks ánd having a rank between 1-5 for each of the four criteria was the best simulation. The selected simulation is regarded as the best realization. This procedure makes sure that each of the four curve characteristics is met in a fairly good way as opposed to a simulation which is doing extremely well for one criterion, but very bad for the others. The followed procedure does not necessarily imply that there is no better model than the selected simulation. Comparing the 'simple' root system architecture with the real data, shows if the simple model encompasses the processes determining the root architecture development. Although it is impossible to fit a unique parameter combination to the data if we make the model more complex, the rhizotron data give clear hints on which processes should and shouldn't be taken into account.

2.5 Measurement uncertainty

An important prerequisite for the calibration approach we presented, is that the dataset is reliable, representative and accurate. It is therefore necessary to assess the uncertainty on the measured mean tube behavior based on ten minirhizotron images. This cannot be tested using the data themselves, as we do not have repetitions of the minirhizotron measurements at other places in the lysimeter at the same depth. Additionally, the data are expected to be correlated, which makes it impossible to use the variance between individual images to estimate the variance of the mean. It is impossible to assess the uncertainty of the normalized mean number of roots directly from the minirhizotron images. However, the uncertainty can be investigated using the optimized growth model by assuming that this model is good enough to represent the actual evolution of the number of roots with time. Using a geostatistical analysis of stochastically simulated root systems, we can assess the variability and the uncertainty on the mean number of roots obtained from our measurement setup.

To characterize the uncertainty on the number of roots obtained from our images, we divided the soil column in a mesh with cells of dx=1.5 cm, dy=5.72 cm and dz=5.72 cm, where dx corresponds with the width of an image and dy

and dz represent the diameter of the minirhizotron.. Each cell represents a couple of minirhizotron images at the same location looking at the left and the right side of the tube. To mimic the real measurements we take n sample sets containing always five of these cells with a distance of 5 cm between the cells.

For each sample i, a local mean (μ_i) and a local standard deviation (σ_i) of the number of roots can be calculated. The global mean M was calculated for n possible samples in the soil column. The uncertainty of M with the chosen sampling design was estimated by calculating the variance of the local μ_i .

In a first analysis, the sample sets always had the same orientation with respect to the plant rows (i.e. perpendicular) but the set could be located anywhere on the Y-axis. In a second analysis, sample again had the same orientation with respect to the plant rows (i.e. perpendicular), but also same distance to the rows were considered. The variance of μ_i for both analyses represents an upper (sample sets located anywhere on the Y-axis) and a lower boundary (sample sets always with the same distance from the rows) for the variance of the estimated normalized number of roots in the rhizotube.

3. Results & Discussion

3.1 Characteristics of the root system development

Figure 30 shows the growth curves of the primary roots in S1 and S2 at tube 1 to 4 (T1-T4) with T1 the tube closest to the soil surface. The characteristics ($t_{50\%}$, Nr_{Max}, SLP) of the growth curves are indicated in Figure 30 and given in Table 6. The crops have a slightly different growth behavior in S1 than in S2. There is an important difference between S1 and S2 concerning the maximum number of roots at T1, T2 and most of all T3. In S2, the roots also reach the deepest horizon quicker than in S1. The effective growth velocity ($v=z/t_{50\%}$), calculated for a rhizotube at depth z, was situated between 1.1 and 1.6 cm.day^{-1} in S1, whereas v was between 1.4 and 2.6 cm.day^{-1} in S2. This effective growth velocity was slightly different for different depths. In soil column S1, the slopes of the growth curves were not equal for all depths, whereas in S2, they were nearly constant with depth. However, it must be noted that the temporal

resolution of the slopes is rather low and thus is the uncertainty of this characteristic rather high.

Table 6. Growth curve and root system architecture characteristics in all tubes (T) of lysimeter S1 and S2. If there were no roots or not enough roots to calculate a reliable average, no value is given (-). $t_{50\%}$= time at which 50% of the maximal amount of roots has arrived, Nr_{Max}= normalized maximal amount of primary roots seen at the tube, SLP= slope of the growth curve between $t_{20\%}$ and $t_{80\%}$, v= effective root growth velocity, $<D_{prim}>$= mean diameter of primary roots at the moment in time the mean diameter was at its maximum , $<D_{sec}>$= mean diameter of secondary roots at the moment in time the mean diameter was at its maximum, $<L_{sec}>$ = mean length of secondary roots, $<Dist_{Ram}>$= mean distance between ramifications.

		S1				S2			
		T1	T2	T3	T4	T1	T2	T3	T4
$t_{50\%}$	(days)	20	30.5	51.5	80.5	13.5	19.5	31.5	45.5
Nr_{Max}	(cm^{-2})	0.28	1.07	0.63	0.02	0.70	0.93	1.40	0.05
SLP	($cm^{-2}.day^{-1}$)	0.028	0.096	0.036	0.003	0.063	0.091	0.102	0.006
$v = \dfrac{z}{t_{50\%}}$	($cm.day^{-1}$)	1.1	1.6	1.4	1.5	1.4	2.3	2.2	2.6
$<D_{prim}>$, std(D_{prim}) (cm)		0.04, 0.006	0.04, 0.008	0.06, 0.01	-,-	0.04, 0.01	0.03, 0.02	0.04, 0.01	-,-
$<D_{sec}>$, std(D_{sec}) (cm)		-,-	0.03, 0.004	0.03, 0.003	-,-	-,-	0.02, 0.006	0.02, 0.005	-,-
$<L_{sec}>$ (cm)		-	0.4	0.6	-	-	0.5	0.4	-
$<Dist_{Ram}>$ (cm)		-	0.4	0.2	-	-	0.3	0.4	-
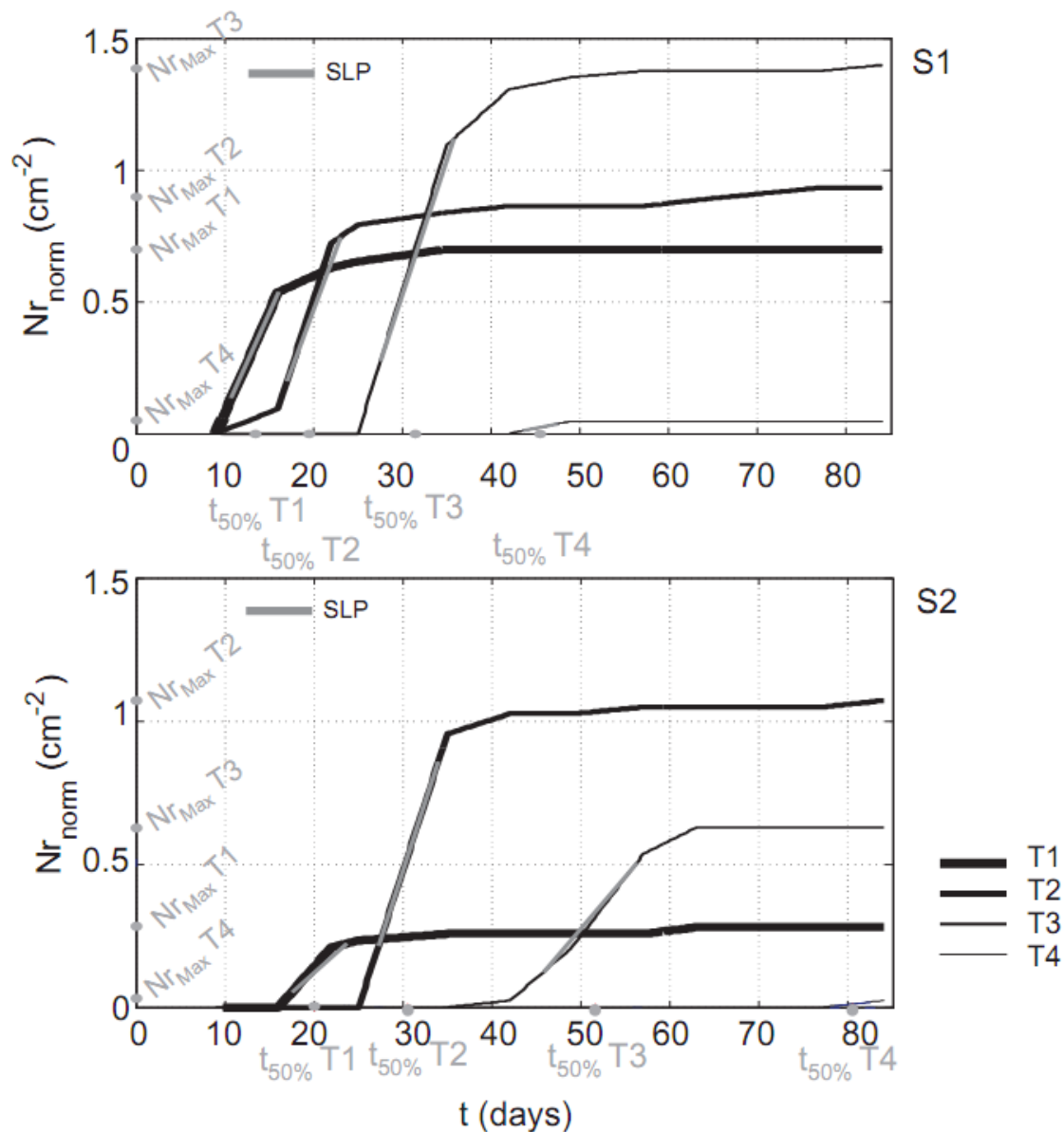
Figure 30. Normalized measured growth curves of primary roots for S1 (top) and S2 (bottom) at rhizotubes T1, T2, T3 and T4. The following growth curve characteristics are shown: $t_{20\%}$, $t_{50\%}$, $t_{80\%}$, $Nr_{norm,Max}$ and SLP.

At the end of the growing season, the number of primary and secondary roots was the highest at tube 2 (-47.5 cm) in S1 and at tube 3 (-72.5 cm) in S2 (see Figure 31). Only very few roots reached the last tube at -122.5/-119.5 cm (S1/S2 respectively). The number of primary roots in the first tube was very low in both lysimeters and almost no ramifications were observed. During the whole growing season, the moisture content increased with depth. As no irrigation was

applied, the topsoil dried out and the difference between the bottom and the top of the lysimeter became large (around 0.20 at the end of the experiment, see Garré et al. (2011).
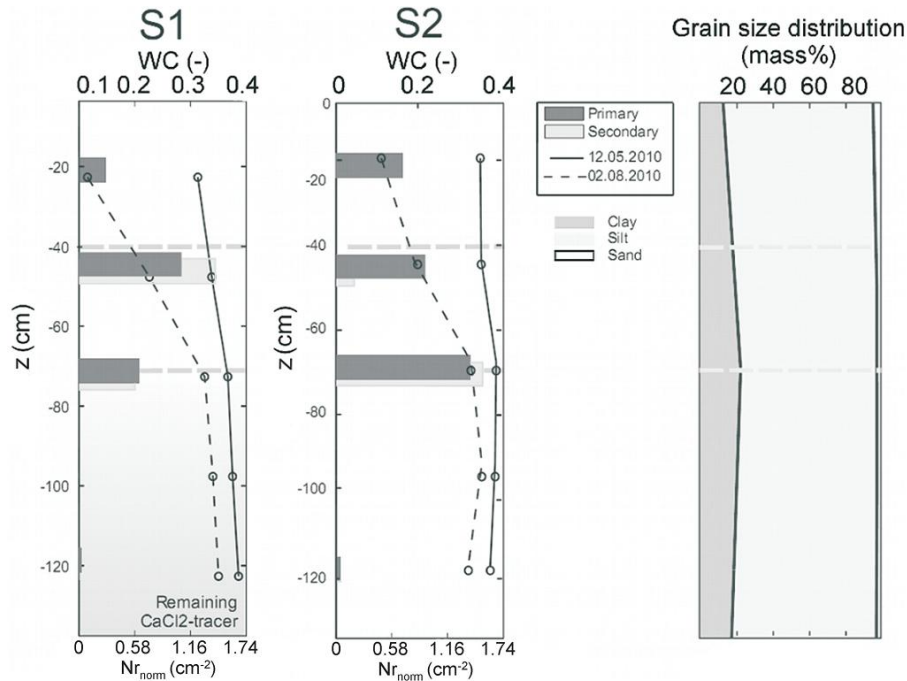
Figure 31. Measured normalized total number of roots (Nr$_{norm}$) per rhizotube at the end of the growing season and water content (WC) profiles at 12.05.2009 (DOY 132) and 02.08.2009 (DOY 214) and grain size distribution of the soil at the Merzenhausen field site (adapted from Weihermüller, 2005). The boundaries of the soil horizons are indicated with grey dashed lines.

Figure 32 shows the diameter of primary and secondary roots in both lysimeters on DOY 195. There is an overlap of both histograms, implying that is is almost impossible to distinguish primary from secondary roots only using the diameter. S1 and S2 show a similar behavior. The mean diameters per tube and the standard deviations are given in Table 6.
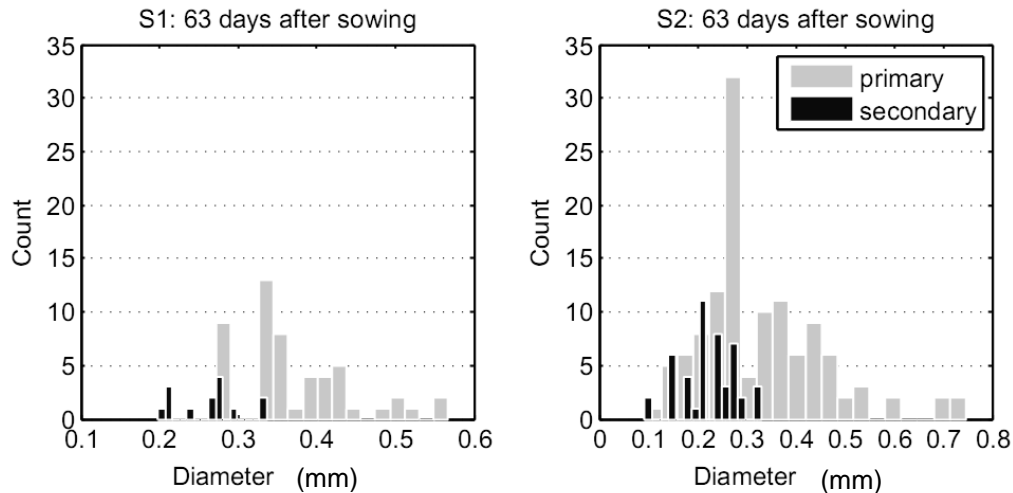
Figure 32. Histogram of root diameters in lysimeter S1 (left) and lysimeter S2 (right) on DOY 195.

3.2 Implications of the observations

If we summarize the observations, four important characteristics appear:

(1) The highest number of roots is not observed at the tube nearest to the soil surface. This implies that new thick and long roots should originate deeper in the soil profile if the observed root growth curves are accurate enough. Primary roots may develop secondary roots much longer and bigger than the normal ramifications. These extended secondary roots then behave almost like primary roots and can even develop ramifications of the third order. This process is called reiteration. It is an alternative form of branching, leading simultaneously to axis growth cessation and to production of a number of axes (of the same type) in sub-apical position. Thus, the reiteration process replaces a given root tip with several root tips of the same type (Pagès et al., 2004). Not very much is known on the origin of this transformation, but a few publications report the presence of reiteration (Lyford, 1980 ; Coutts, 1987 ; Atger et al., 1992; Vercambre et al., 2003). Unfortunately, we could not make a vertical section of the lysimeters to observe the whole rooting profile, but there is evidence that this process takes place with barley. Dupriez (2010, personal communication) followed the root growth of many barley plants in a 2-D rhizotron filled with a homogenous soil (50x100x0.4 cm^3) . They observed an enormous variability of the root system architecture between plants and regularly saw secondary roots

becoming very long and producing ramifications. One example of their unpublished raw root tracking images is given in Figure 33.

10 cm
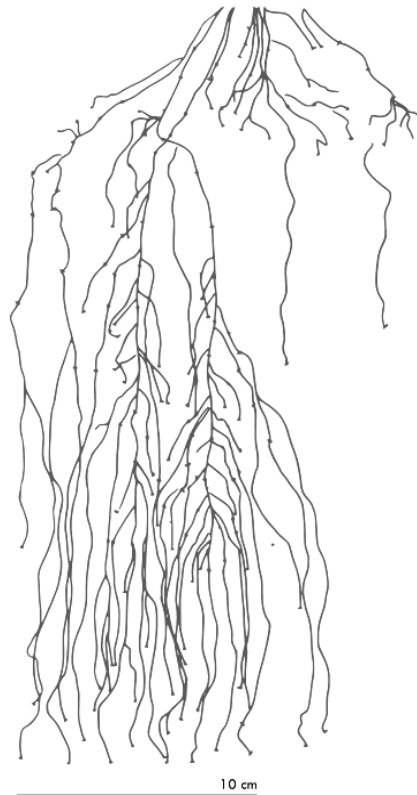
Figure 33. Root system of one barley plant in a 2D rhizotron homogeneously filled with a mixture of sand of Fontainebleau and clay. (Dupriez, 2010)

(2) We observed a difference between the root diameters of primary and secondary roots, but the histograms of the diameter both groups overlap. This may sustain the hypothesis of the formation of highly developed secondary roots in certain soil horizons. These secondary roots may behave almost like primary roots and thus also- have similar diameters, making it difficult to discriminate between primary and developed secondary roots.

(3) The effective growth velocity of the roots changes with depth, which could mean that the layered soil environment causes the roots to change their growth velocity or the tortuosity of their paths within certain horizons.

(4) The slope of the growth curves changes with depth. This may again be explained by the possibility of reiteration at some depths, by a changing root growth velocity depending on changing characteristics of the soil horizons or a

combination of both. However, the time resolution of the root growth curves must be good enough to have an accurate estimation of the slope.

3.3 Evaluation of RootTyp simulations

The sensitivity of the modeled growth curves to realistic changes of the parameters is shown using 107 performed simulations of a lysimeter with plants having simple root systems with long primary and small regularly spaced unramified secondary roots. We concentrate on the simulation performance for S1, but exactly the same procedure was followed for S2. Figure 34 shows the influence of the different parameter combinations (corresponding to columns of Figure 34) of all simulated cases on the growth curve characteristics $t_{50\%}$, Nr_{Max} and SLP (corresponding to the rows of Figure 34). The five 'best' realizations are indicated with a star. As stated above, the best realization is the one with the best sum of ranks and having a rank between 1 and 5 for each of the four criteria.

The first column of Figure 34 shows that the root growth velocity (v_{INIT}) influences mainly the moment at which 50 % of the roots have arrived at a certain depth ($t_{50\%}$). It also shows that $t_{50\%}$ does not depend a lot on the other parameters since for a constant value of v_{INIT}, the RMSE($t_{50\%}$) does not differ much due to variations in the other parameters. The optimal v_{INIT} for S1 was fixed to 2 cm.day^{-1} and for S2 to 3 cm.day^{-1}, as these velocities minimized the $t_{50\%}$-criterion. In S2, 3 cm.day^{-1} was not the absolute minimum, but higher velocities caused the roots to arrive much too early at the deepest tube and did not improve the RMSE($t_{50\%}$) greatly.

The number of primary roots (<Nr_{Prim}>) affected mainly the maximum number of roots counted at the rhizotube (Nr_{Max}). This is clear from the second column of Figure 34, which shows that for a changing Nr_{Prim}, the RMSE(Nr_{Max}) is much more affected than the other criteria. $t_{50\%}$ was not systematically influenced by <Nr_{Prim}>. However, RMSE(SLP) was affected by Nr_{Prim} given a fixed std(v_{INIT}). In the same time interval, more roots are generated from the type 0 axis and thus the maximum number of primary roots seen at the rhizotube increases. The

slope of the growth curve has to increase to obtain a higher root number in the same time interval. As Nr_{Prim} has the biggest influence in the chosen parameter intervals, Nr_{Prim} had to be fixed before optimizing $std(v_{INIT})$. Nr_{Prim} was set to 31 for S1 and 51 for S2, which is a very high number. It has to be noted that this number is affected by the number of plants in the simulation.

The influence of $std(v_{INIT})$ was not as clear as for the other parameters, showing the low sensitivity of the modeled data on this parameter. For the selected $<v_{INIT}>$ and $<Nr_{Prim}>$, we could find some cases which resulted in a very low RMSE(SLP) lying between 0-0.2 cm.day^{-1} for both lysimeters. However, these where not the only cases minimizing RMSE(SLP). Finally, we evaluated the cases with a different $<\alpha>$ and $std(\alpha)$. As Figure 34 shows, there was no big difference between the three insertion angles (2.44, 2.83 and 2.88) and the initial guess for $<\alpha>$ gave the best results. $std(\alpha)$ was varied between 0.0171 and 0.171, but no obvious superior $std(\alpha)$ was found looking at the RMSE as a function of $std(\alpha)$.
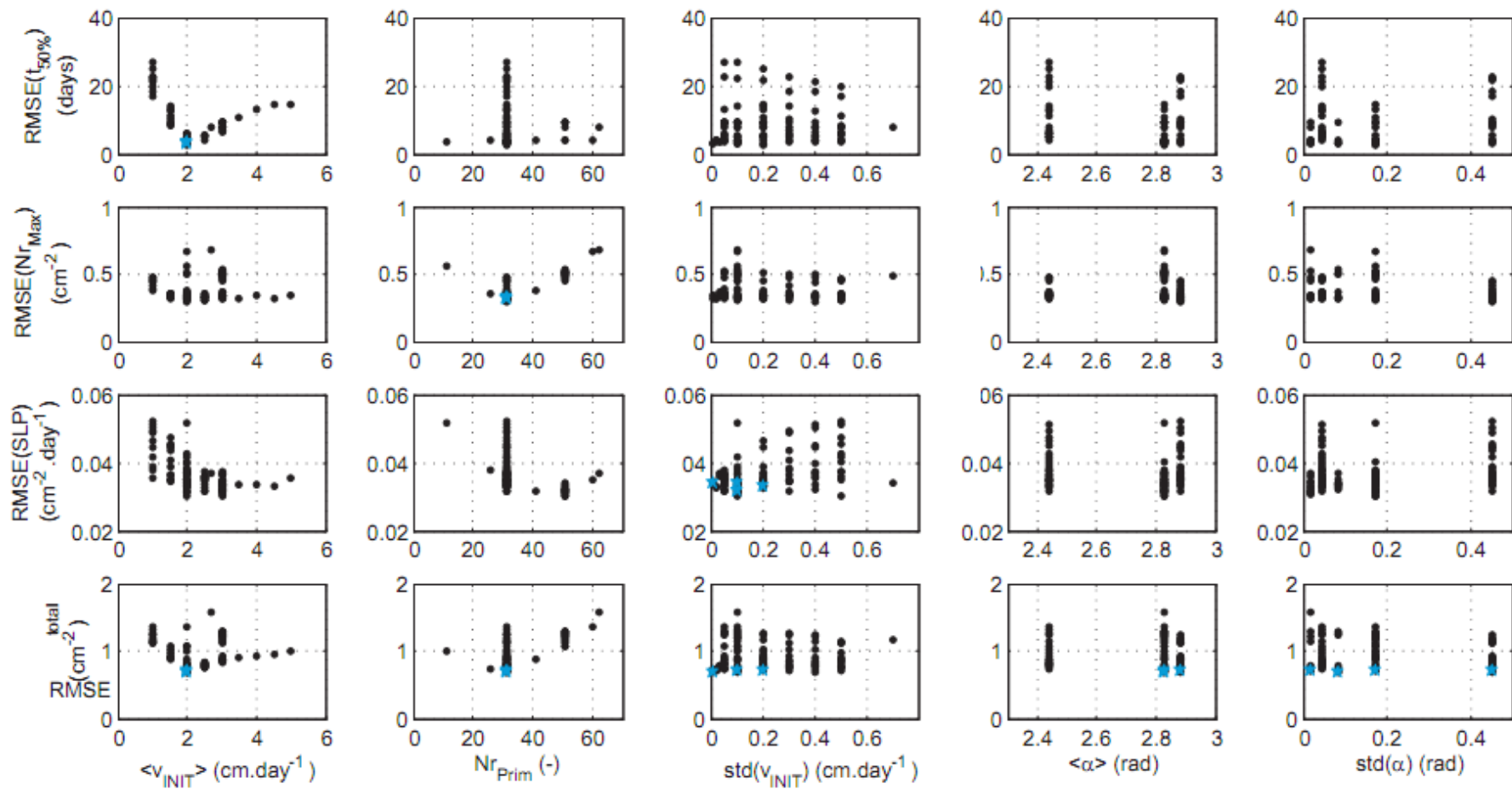
★5 best realizations
good performance on all 4 criteria + good overall performance

Figure 34. Performance of the 107 simulations on four optimization criteria (RMSE(t50%)) (days, RMSE(NrMax) (cm-2), RMSE(SLP) (day-1.cm-2) and RMSE (cm-2)) as a function of five parameter ranges (<vINIT> (cm.day-1), NrPrim (-), std(vINIT) (cm.day-1), <α> (rad) and std(α) (rad)) for lysimeter 1.
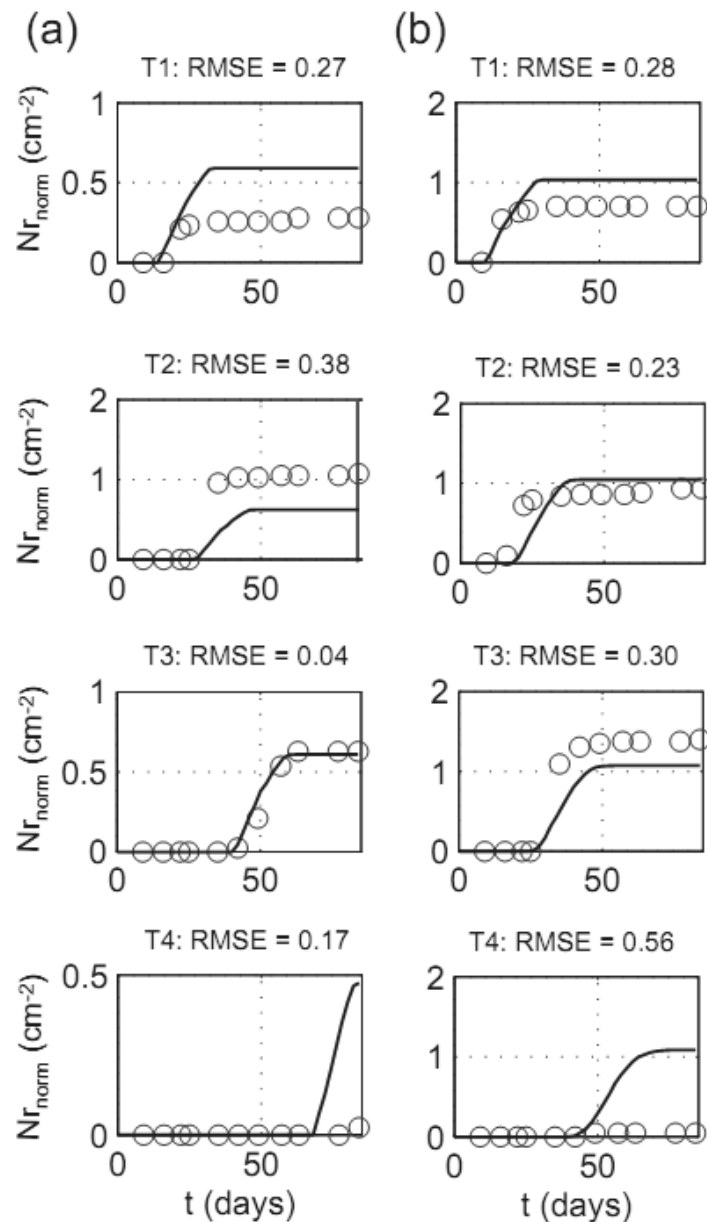
Figure 35. Normalized simulated and measured growth curves for tubes T1 – T4 in (a) lysimeter S1 and (b) lysimeter S2. The simulations shown are the best fits for S1 and S2.

3.4 Best realization

The best realization for S1 using a simple root model proved to be $\langle\alpha\rangle$= 2.83, std(α) = 0.085, $\langle v_{INIT}\rangle$= 2.0 cm.day^{-1}, std(v_{INIT})= 0.10 cm.day^{-1} and Nr_{Prim}= 31. The root diameters and distance between ramifications of the root architecture were taken to be the mean of what was observed on the rhizotubes.

Figure 35a shows the simulated and measured growth curves at the rhizotubes (T1-T4) and Figure 36a depicts the root system architecture of one single plant

of the simulation. The following parameters were best for S2: $<\alpha>$= 2.83, std(α) = 0.171, $<v_{INIT}>$= 3.0 cm.day^{-1}, std(v_{INIT})= 0.30 and Nr$_{Prim}$= 51. The root diameters and distance between ramifications of the root architecture were the mean of what was observed on the rhizotubes. Figure 35b shows the simulated and measured growth curves and Figure 36b depicts the root system architecture of one single plant. Firstly, these images show that the model cannot predict the increase in Nr$_{Max}$ with depth. Secondly, the model overpredicts the root growth at greater depths and this leads to unrealistically large rooting depths.
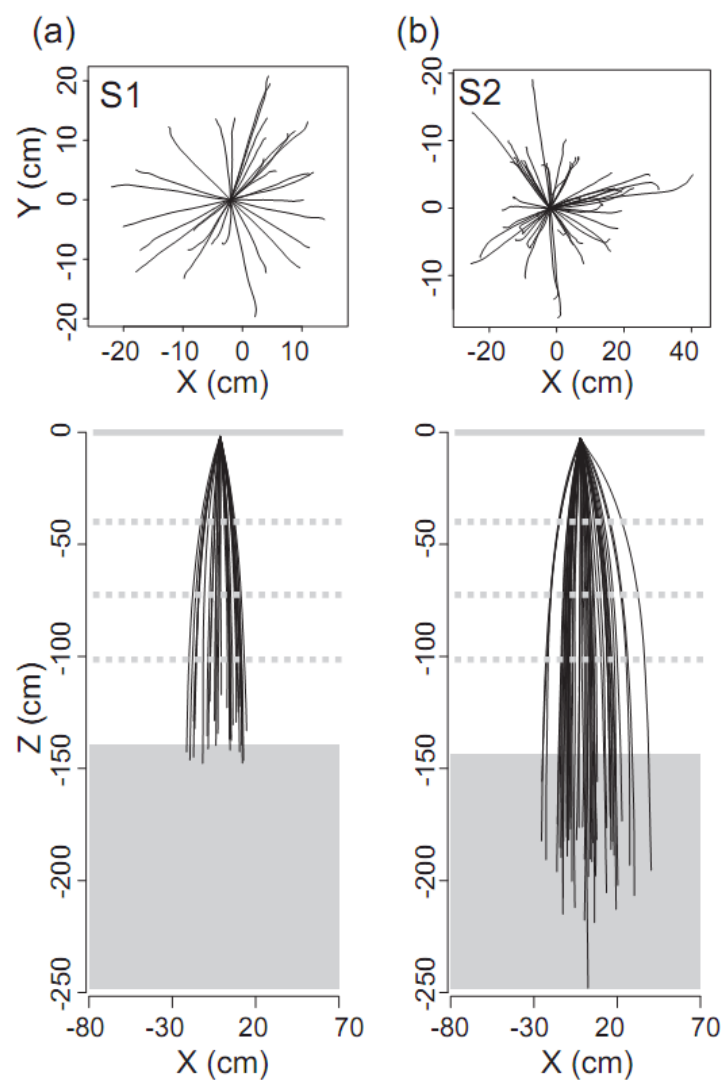
Figure 36. Simulated root system for lysimeter S1 and S2 (only primary roots). The grey dashed lines indicate the soil horizon boundaries. The gray patch at the bottom indicates the depth at which the lysimeter bottom is reached. The model did not impose this bottom boundary.

Finally, it has to be noted that for the parameter estimation of the simple RA model, the emission rhythm of primary roots from the 0th order axis should be kept constant. Varying this emission rhythm greatly affects the slope of the growth curves. In principle, if the temporal resolution of minirhizotron data is high enough, a real growth velocity and its standard deviation can be measured using root lengths in subsequent images of a root growing along the minirhizotube. However, the question remains if the growth velocity at the tube interface is the same as in the soil. If no information is available on the emission velocity from other studies, the difference between the emergence of a root, its growth velocity and the tortuosity of its path can't be made using minirhizotron data.

3.5 Towards a more detailed model

We observed a higher number of roots at -47.5/-44.5 cm depth than at -22.5/-19.5 cm depth. In S2, the number even still increased at -69.5 cm depth. We also observed that the slope of the growth curves in S1 changed with depth whereas in S2 these slopes were very similar in all depths. A simple root architecture (RA) model with a certain amount of primary roots and small ramifications could not reproduce these observations. The simple root system architecture model overpredicts the number of roots in the top soil a little and the rooting depth and the number of roots in the deeper soil very strongly. It also has a constant slope of the growth curves with depth, which is not in agreement with the observations. The simple model with long primary roots growing at a constant velocity in each soil horizon and ramified with short secondary roots does not reproduce the measured root number patterns. Looking at the data, we identified two additional processes which may be important to take into account: root reiteration and the influence of stochastic and structural soil heterogeneity.

If we simulate root growth with the possibility of a reiteration process, which replaces a given root tip with several root tips of the same type, it is possible to increase the root number with depth and to obtain variable slopes of the growth curve with depth. However, this increases the number of parameters to be

optimized with four: a date at which the reiteration starts, a probability for the reiteration to take place and a minimum and maximum number of roots to be formed at the root tip when it re-iterates. Using only minirhizotron data, it is impossible to estimate a unique parameter set, since there is no information on the origin of the roots arriving at the rhizotube.

The soil, conceptualized as an ensemble of horizontal layers, can affect root elongation and direction, as well as root branching density. Its influence is formalized in the model RootTyp using simple coefficients representing the soil constraint and the sensitivity of a certain root type to this constraint. Again, this adds many unknown parameters to the model which cannot be estimated using minirhizotron data alone. Even if the soil density and moisture content are known, the reaction of primary and secondary roots on their environment remains largely unknown. However, from the shape of the different growth curves and the changing effective growth velocities, it becomes clear that the soil must have influenced the root development and as such, the minirhizotron data do provide important information to formulate hypotheses for a better root architecture model.

Figure 37 (a) shows the simulated and measured root growth curves of lysimeter S2 using a complex model with reiteration and soil layering. Figure 37 (b) depicts the root system of a single plant in the simulation. This solution fits the data much better than the optimal simple RA model, however, the solution is not unique. Nevertheless, the minirhizotron data indicate that reiteration and soil influences should be taken into account.
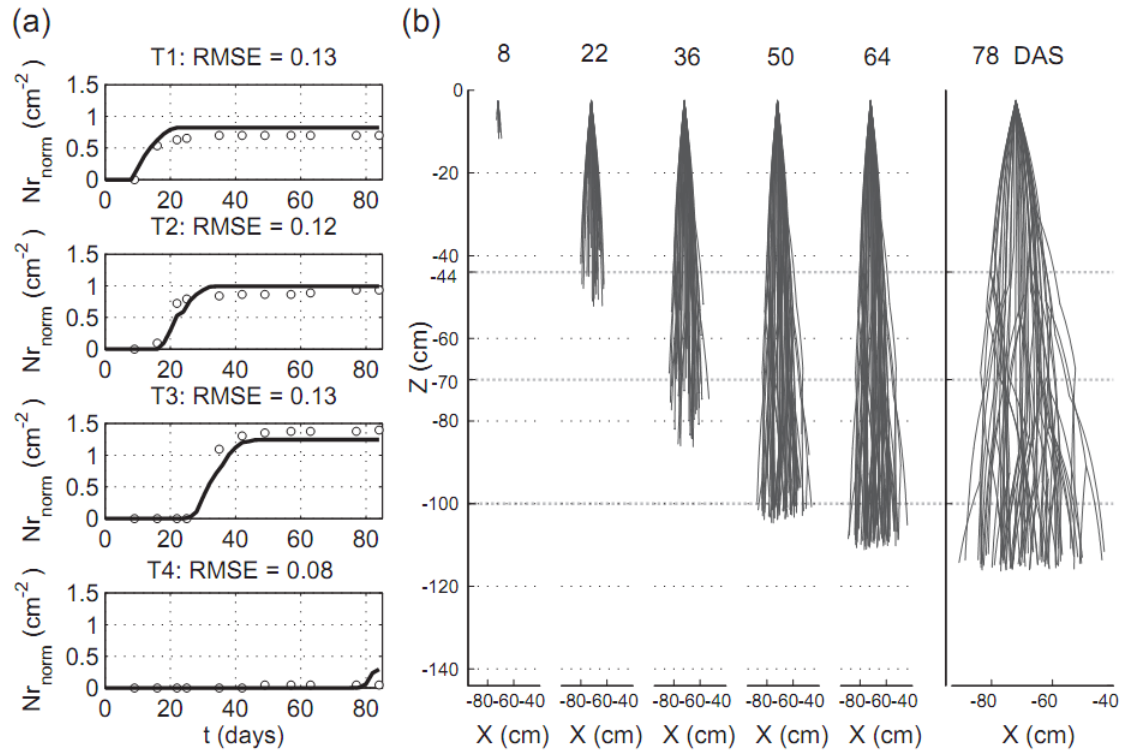
Figure 37. (a) Normalized simulated (complex model) and measured growth curves for tubes T1 – T4 in lysimeter S2; (b) evolution in time of the simulated complex root system with reiteration and soil layering for lysimeter S2. The grey dashed lines indicate the soil horizon boundaries. (DAS = days after sowing)

Table 7. Variance of the mean normalized number of roots ($<Nr_{norm}>$) for the simulation shown in figure 12 if samples of 5x2 images are taken anywhere in the column (VAR_{unres}) and variance of $<Nr_{norm}>$ if samples of 5x2 images are always situated the same way with respect to the plant rows (VAR_{res}).

	VAR_{unres} (cm^{-2})	VAR_{res} (cm^{-2})
	$n = 60$	$n = 600$
T1: -19.5 cm	0.042	0.022
T2: -44.5 cm	0.042	0.032
T3: -69.5 cm	0.063	0.086
T4: -119.5 cm	0.015	0.014

3.6 Reliability of the minirhizotron technique

The stochastic analysis was performed for two cases: samples of 5x2 images taken anywhere in the column (VAR_{unres}) and samples of 5x2 images always situated the same way with respect to the plant rows (VAR_{res}). Table 7 shows these variances of $<Nr_{norm}>$ for the simulation shown in Figure 37 84 days after sowing. At the top the unrestricted variance of the mean is clearly higher than the restricted one, but at the lower depths, this is not the case anymore. In general however, this variance is rather high as compared to the mean.

4. Conclusions

Minirhizotrons are the only way to retrieve dynamic information on root growth and root architecture (RA) in an undisturbed soil environment at the lysimeter or field scale without destroying parts of the root system. RA model parameters greatly influencing the root growth curve at a certain depth are the root growth velocity, its standard deviation, the number of primary roots emitted and the mean insertion angle of these roots and its standard deviation. Using a step-wise optimization procedure, we could estimate these parameters to fit the minirhizotron data at four depths in an undisturbed soil monolith. The deviation between the model results and the observations indicated that other processes which were not considered in the simple simulations, such as reiteration, played an important role in the root development during this experiment. It must be noted that the experiments were run under extreme conditions (i.e. no rain or irrigation during the entire growing season). Processes such as reiteration may therefore be a reaction of the plant to these conditions so as to optimize the water uptake from deeper soil layers.

However, we showed that the minirhizotron technique does not provide enough information to restrain a RA model with reiteration and soil layering in a satisfying way. To reduce measurement uncertainty, minirhizotron images should be continuous along the tube and made with high temporal resolution. The number of unknowns may be reduced by making a vertical section of the root system in a trench at the end of an experiment to measure e.g. root insertion angles and the occurrence and location of reiteration. The primary root emission rhythm could be measured at a smaller scale using non-invasive imaging techniques such as MRI. Additional information from other experiments on the plant under consideration and in a similar environment is thus necessary and may greatly improve the model results. Nevertheless, even with little information, a simple model can be adjusted, making it possible to explore realistic rooting profiles going beyond the limited, discrete measurements of a few rhizotubes. Since many water flow models rely on a root density profile to predict root water uptake, this is of great importance.

5. Appendix 1: RootTyp parameters lysimeter 1 (S1)

Simulation duration (days) (entier)	84		
Number of transplant axes (type 0)	1		
Number of reiteration wavees	9		
Reiteration dates	422, 440, 550, 760, 970, 1180, 1400, 1610		
Increase coefficient of diameter	0.0		
	TYPE 0	**TYPE 1**	**TYPE 2**
Insertion angle on preceding order (mean std)	3.1416 / 0.00	2.83 / 0.0850	1.4 / 0.6
Insertion angle with reiteration (mean std)	0.7 / 0.05	0.7 / 0.05	0.7 / 0.05
Duration primordium development (days)	4.0	3.0	5.0
Growth parameters: asymptote and initial velocity (mean)	1.0 / 0.04	1000.0 / 2.0	0.45 / 0.20
Growth parameters (std)	0.0 / 0.0	0.0 / 0.01	0.1 / 0.0
Parameters distance between ramifications (mean std)	0.0165 / 0.0025	0.3 / 0.01	1000.0 / 0.0
Gravitropism type	-1	+1	+2
Gravitropism intensity	0.001	0.001	0.05
Sensitivity to mechanical constraint	0.0	0.02	0.5
Initial diameter of the root tip	0.15	0.04	0.03
Period between growth stop and necrosis (days)	8000.0	1800.0	110.0
Probability of reiteration	0.0	0.0	0.0
Min and max number of roots when reiteration occurs	0 / 0	0 / 0	0 / 0
Trigger age for possible transformation	1000.0	1000.0	1000.0
Probability of transformation	0.0	0.0	0.0
Direction of transformation	-1	-1	-1
Proportion of types (0..7) within ramifications	0.0 1.0 0.0 0.0 0.0 0.0 0.0 0.0	0.0 0.0 1.0 0.0 0.0 0.0 0.0 0.0	0.0 0.0 0.0 1.0 0.0 0.0 0.0 0.0

6. Appendix 2: RootTyp parameters lysimeter 2 (S2)

Simulation duration (days) (entier)	84		
Number of transplant axes (type 0)	1		
Number of reiteration wavees	9		
Reiteration dates	422, 440, 550, 760, 970, 1180, 1400, 1610		
Increase coefficient of diameter	0.0		
	TYPE 0	**TYPE 1**	**TYPE 2**
Insertion angle on preceding order (mean std)	3.1416 / 0.00	2.83 / 0.171	1.4 / 0.6
Insertion angle with reiteration (mean std)	0.7 / 0.05	0.7 / 0.05	0.7 / 0.05
Duration primordium development (days)	4.0	3.0	5.0
Growth parameters: asymptote and initial velocity (mean)	1.0 / 0.04	1000.0 / 3.0	0.32 / 0.15
Growth parameters (std)	0.0 / 0.0	0.0 / 0.30	0.1 / 0.0
Parameters distance between ramifications (mean std)	0.01 / 0.0025	0.35 / 0.01	1000.0 / 0.0
Gravitropism type	-1	+1	+2
Gravitropism intensity	0.001	0.001	0.05
Sensitivity to mechanical constraint	0.0	0.02	0.5
Initial diameter of the root tip	0.15	0.03	0.02
Period between growth stop and necrosis (days)	8000.0	1800.0	110.0
Probability of reiteration	0.0	0.0	0.0
Min and max number of roots when reiteration occurs	0 / 0	0 / 0	0 / 0
Trigger age for possible transformation	1000.0	1000.0	1000.0
Probability of transformation	0.0	0.0	0.0
Direction of transformation	-1	-1	-1
Proportion of types (0..7) within ramifications	0.0 1.0 0.0 0.0 0.0 0.0 0.0 0.0	0.0 0.0 1.0 0.0 0.0 0.0 0.0 0.0	0.0 0.0 0.0 1.0 0.0 0.0 0.0 0.0

7. Appendix 3: overview conducted simulations and optimization strategy

Nr$_{Prim}$ (-)	<α> (rad)	std(α) (rad)	<v$_{INIT}$> (cm.day^{-1})	std(v$_{INIT}$) (cm.day^{-1})
31.00	2.44	0.05	1.00	0.05
31.00	2.44	0.05	1.00	0.10
31.00	2.44	0.05	1.00	0.20
31.00	2.44	0.05	1.00	0.30
31.00	2.44	0.05	1.00	0.40
31.00	2.44	0.05	1.00	0.50
31.00	2.44	0.05	1.50	0.05
31.00	2.44	0.05	1.50	0.10
31.00	2.44	0.05	1.50	0.20
31.00	2.44	0.05	1.50	0.30
31.00	2.44	0.05	1.50	0.40
31.00	2.44	0.05	1.50	0.50
31.00	2.44	0.05	2.00	0.05
31.00	2.44	0.05	2.00	0.10
31.00	2.44	0.05	2.00	0.20
31.00	2.44	0.05	2.00	0.30
31.00	2.44	0.05	2.00	0.40
31.00	2.44	0.05	2.00	0.50
31.00	2.44	0.05	2.50	0.05
31.00	2.44	0.05	2.50	0.10
31.00	2.44	0.05	2.50	0.20
31.00	2.44	0.05	2.50	0.30
31.00	2.44	0.05	2.50	0.40
31.00	2.44	0.05	2.50	0.50
31.00	2.44	0.05	3.00	0.05
31.00	2.44	0.05	3.00	0.10
31.00	2.44	0.05	3.00	0.20
31.00	2.44	0.05	3.00	0.30
31.00	2.44	0.05	3.00	0.40
31.00	2.44	0.05	3.00	0.50
31.00	2.83	0.02	2.00	0.01
31.00	2.83	0.02	2.00	0.02
31.00	2.83	0.02	2.00	0.04
31.00	2.83	0.02	2.00	0.05
31.00	2.83	0.02	2.00	0.10
31.00	2.83	0.02	2.00	0.10
62.00	2.83	0.02	2.70	0.10
51.00	2.83	0.02	3.00	0.05
51.00	2.83	0.02	3.00	0.10
51.00	2.83	0.02	3.00	0.10
31.00	2.83	0.09	2.00	0.01
31.00	2.83	0.09	2.00	0.02
31.00	2.83	0.09	2.00	0.04
31.00	2.83	0.09	2.00	0.05
31.00	2.83	0.09	2.00	0.10
31.00	2.83	0.09	2.00	0.10
51.00	2.83	0.09	3.00	0.05
51.00	2.83	0.09	3.00	0.10
51.00	2.83	0.09	3.00	0.10
31.00	2.83	0.17	2.00	0.05
31.00	2.83	0.17	2.00	0.10
31.00	2.83	0.17	2.00	0.10
31.00	2.83	0.17	2.00	0.20
31.00	2.83	0.17	2.00	0.30
31.00	2.83	0.17	2.00	0.40
31.00	2.83	0.17	2.00	0.50
51.00	2.83	0.17	3.00	0.05
51.00	2.83	0.17	3.00	0.10
51.00	2.83	0.17	3.00	0.10
51.00	2.83	0.17	3.00	0.20
51.00	2.83	0.17	3.00	0.30
51.00	2.83	0.17	3.00	0.40
51.00	2.83	0.17	3.00	0.50
51.00	2.83	0.17	3.00	0.70
51.00	2.83	0.17	2.00	0.10
41.00	2.83	0.17	2.00	0.10
51.00	2.83	0.17	2.00	0.10
60.00	2.83	0.17	2.00	0.10
31.00	2.83	0.17	2.00	0.20
31.00	2.83	0.17	2.50	0.20
31.00	2.83	0.17	3.00	0.20
31.00	2.83	0.17	3.50	0.20
31.00	2.83	0.17	4.00	0.20
31.00	2.83	0.17	4.50	0.20
31.00	2.83	0.17	5.00	0.20
31.00	2.88	0.45	1.00	0.05
31.00	2.88	0.45	1.00	0.10
31.00	2.88	0.45	1.00	0.20
31.00	2.88	0.45	1.00	0.30
31.00	2.88	0.45	1.00	0.40
31.00	2.88	0.45	1.00	0.50
31.00	2.88	0.45	1.50	0.05
31.00	2.88	0.45	1.50	0.10
31.00	2.88	0.45	1.50	0.20
31.00	2.88	0.45	1.50	0.30
31.00	2.88	0.45	1.50	0.40
31.00	2.88	0.45	1.50	0.50
31.00	2.88	0.45	2.00	0.05
31.00	2.88	0.45	2.00	0.10

113

31.00	2.88	0.45	2.00	0.20
31.00	2.88	0.45	2.00	0.30
31.00	2.88	0.45	2.00	0.40
31.00	2.88	0.45	2.00	0.50
31.00	2.88	0.45	2.50	0.05
31.00	2.88	0.45	2.50	0.10
31.00	2.88	0.45	2.50	0.20
31.00	2.88	0.45	2.50	0.30
31.00	2.88	0.45	2.50	0.40
31.00	2.88	0.45	2.50	0.50
31.00	2.88	0.45	3.00	0.05
31.00	2.88	0.45	3.00	0.10
31.00	2.88	0.45	3.00	0.20
31.00	2.88	0.45	3.00	0.30
31.00	2.88	0.45	3.00	0.40
31.00	2.88	0.45	3.00	0.50
11.00	2.83	0.17	2.00	0.10
26.00	2.83	0.17	2.00	0.10

Part IV
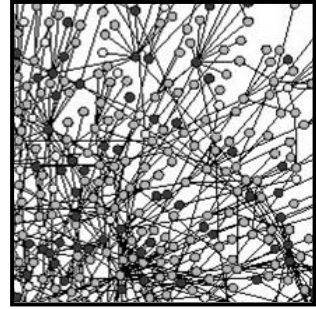
Synthesis

1. Final Conclusions

Electrical resistivity tomography (ERT) proved to be a valuable technique to monitor solute transport and soil moisture changes non-invasively in undisturbed soils. Under steady-state conditions using a salt tracer step experiment, the technique allows for quantitative solute tracking (Koestel et al., 2008; Garré et al., 2010). Also under non-stationary conditions, ERT was shown to be a promising technique. However, in those cases the success depends on the calibration of the relationship between the measured electrical resistivity and the quantity under consideration. The application of ERT to measure root zone water dynamics is possible, but needs to be further examined, since the influence of roots on the relationship between electrical resistivity and water content is not yet fully understood.

Water flow and solute transport in soils with plants is a complex process which is difficult to model. This is due to soil and plant heterogeneity, interactions and variable boundary conditions. Even in bare soils, flow and transport processes are very complex. Water flow is often irregular and exibits markedly non-uniform patterns, because soils are inherently heterogeneous and structured at different spatial scales. We showed that a combination of measurement techniques should be used to investigate different appearances of heterogeneous solute transport in soils at different spatial scales. These appearances are different for different soils and do not necessarily occur simultaneously.

Moisture content patterns in a cropped, undisturbed soil can be derived using 3-D ERT. We sustained this using a global mass balance method and a comparison between ERT- and TDR-derived local variablility of the soil water content. A horizon-specific in-situ calibration was necessary to convert bulk electrical resistivity to water content. The spatial patterns of wetter and drier regions changed during the drying process and our results indicated that the plants may have adapted there root system architecture in order to compensate for water shortage in the upper horizon.

The relationship between soil moisture depletion and water uptake can only be understood if we gain a better understanding of a plants' root system architecture and the dynamics of this system. We constructed a root architecture model for the barley plants using minirhizotron data. We found that these data provide valuable information to optimize a simple root model. Nonetheless, extra information was needed to use a more satisfying model incorporating root reiteration and soil density.

2. Outlook

2.1 ERT

ERT is a very promising technique for investigating the soil-plant continuum. However, many technical issues need to be solved before the technique can be used in any environment. First of all, it is still not possible to quantify the ensemble of measurement and inversion errors. Secondly, the smoothness constrained inversion remains suboptimal to represent a system which inherently has sharp contrasts. Development of other inversion strategies might be necessary to get a right impression of the the effect of boundaries between soil layers with different hydraulic and electrical properties on water content and salt tracer distributions in layered soil profiles. Finally, the relationship between measured electrical resistivity and water content and/or solute concentration is not always easy to calibrate. Soil structure and constitution, temperature and root tissue may change the relationship and it remains difficult to quantify their influence in certain cases. Carefull calibration under well-known conditions still remains necessary.

2.2 Water flow in the soil-plant continuum

We have shown some valuable measurements of soil water depletion by roots. However, we were not succesfull in separating root water uptake and resulting soil water fluxes. In order to calculate 3-D root water uptake from soil moisture measurements, the soils hydraulic characteristics have to be known. Predicting water fluxes in an undisturbed, structured soil at the lysimeter scale remains difficult and thus also the estimation of root water uptake. The research on the

estimation of soil hydraulic characteristics for real, layered soils should be continued. As Vogel et al. (2006) point out, the soil is structured hierarchically and the problem of stochastic and structural heterogeneity should be addressed. Durner et al. (2008) and Bayer et al. (2005) indicated that estimated effective hydraulic parameters depend on the experimental technique and that the arrangement of soil layers greatly influences the estimated effective parameters. Hydraulic properties should be determined for each layer and interlayer interactions should be studied (Carrick et al., 2010) and taken into account.

2.3 Solute transport in the soil-plant continuum

Solute transport proved to be already very complex in bare soil. A major cause of non-uniform flow fields are the structures present in real soil. Since plants contribute to the formation of soil structures, they are expected to affect solute transport. However, there are almost no studies dealing with this effect. The data analysis of the experiments done within this PhD project should be continued in order to investigate the effect of plants on solute transport. If such an effect can be seen, the effect of the physical presence of roots and of active and passive root water uptake should be separated and quantified.

References

Adams, E.E., and L.W. Gelhar. 1992. Field study of dispersion in a heterogeneous aquifer 2. Spatial moments analysis. Water Resour. Res. 28:3293-3307.

al Hagrey, S.A. 2007. Geophysical imaging of root-zone, trunk, and moisture heterogeneity. J. Exp. Bot. 58:839-854.

al Hagrey, S.A., and J. Michaelson. 1999. Resistivity and percolation study of preferential flow in vadose zone at bokhorst, germany. Geophysics 64:746-753.

Allen, R.G., L.S. Pereira, D. Raes, and M. Smith. 1998. Crop evapotranspiration - guidelines for computing crop water requirements. *In* N.R.M.a. Environment (ed.) FAO, Rome.

Amato, M., G. Bitella, R. Rossi, J.A. Gómez, S. Lovelli, and J.J.F. Gomes. 2009. Multi-electrode 3d resistivity imaging of alfalfa root zone. Eur. J. Agron. 31:213-222.

Amidu, S.A., and J.A. Dunbar. 2007. Geoelectric studies of seasonal wetting and drying of a texas vertisol. Vadose Zone J 6:511-523.

Archie, G.E. 1942. The electrical resistivity log as an aid in determining some reservoir characteristics. Trans. Am. Inst. Min. Metall. Pet. Eng. 146:54 - 67.

Aris, R. 1958. On the dispersion of linear kinematic waves. Proceedings of the Royal Society of London. Series A. Mathematical and Physical Sciences 245:268-277.

Atger, C., and C. Edelin. 1992. Premières données sur l'architecture comparée des systèmes racinaires et caulinaires des arbres. Can. J. Bot. 72.

Bayer, A., H.J. Vogel, O. Ippisch, and K. Roth. 2005. Do effective properties for unsaturated weakly layered porous media exist? An experimental study. Hydrol. Earth Syst. Sci. 9:517-522.

Bengough, A.G., M.F. Bransby, J. Hans, S.J. McKenna, T.J. Roberts, and T.A. Valentine. 2006. Root responses to soil physical conditions; growth dynamics from field to cell. J. Exp. Bot. 57:437-447.

Bernier, P.Y., and G. Robitaille. 2004. A plane intersect method for estimating fine root productivity of trees from minirhizotron images. Plant Soil 265:165-173.

Bingham, I.J., and A.G. Bengough. 2003. Morphological plasticity of wheat and barley roots in response to spatial variation in soil strength. Plant and Soil 250:273-282.

Binley, A., S. Henry Poulter, and B. Shaw. 1996. Examination of solute transport in an undisturbed soil column using electrical resistance tomography. Water Resour. Res. 32:763-769.

Binley, A., B. Shaw, and S. Henry Poulter. 1996. Flow pathways in porous media: Electrical resistance tomography and dye staining image verification. Meas. Sci. Technol. 7:384-390.

Bloem, E. 2008. Variation in space and time of water flow and solute transport in heterogeneous soils and aquifers. PhD Thesis. Wageningen University, Wageningen.

Bloem, E., F.A.N. Hogervorst, and G.H. de Rooij. 2009. A field experiment with variable-suction multi-compartment samplers to measure the spatio-temporal distribution of solute leaching in an agricultural soil. J. Contam. Hydrol. 105:131-145.

Bloem, E., J. Vanderborght, and G. H. de Rooij 2008. Leaching surfaces to characterize transport in a heterogeneous aquifer: Comparison between flux concentrations, resident concentrations, and flux concentrations estimated from temporal moment analysis. Water Resour. Res. 44:W10412.

Bragg, P., G. Govi, and R. Cannell. 1983. A comparison of methods, including angled and vertical minirhizotrons, for studying root growth and distribution in a spring oat crop. Plant and Soil 73:435-440.

Bragg, P.L., P. Rubino, F.K.G. Henderson, W.J. Fielding, and R.Q. Cannell. 1984. A comparison of the root and shoot growth of winter barley and winter wheat, and the effect of an early application of chlormequat. The Journal of Agricultural Science 103:257-264.

Bronshstein, I.N., and K.A. Semendyayev. 1979. Handbook of mathematics. [Online] Van Nostrand Reinhold, Frankfurt/Main.

Buchter, B., C. Hinz, M. Flury, and H. Fluhler. 1995. Heterogeneous flow and solute transport in an unsaturated stony soil monolith. Soil Sci. Soc. Am. J. 59:14-21.

Burkhardt, M., R. Kasteel, S. Giesa, and H. Vereecken. 2005. Characterization of field tracer transport using high-resolution images. Vadose Zone J. 4:101-111.

Carrick, S., P. Almond, G. Buchan, and N. Smith. 2010. In situ characterization of hydraulic conductivities of individual soil profile layers during infiltration over long time periods. Eur. J. Soil Sci.:no-no.

Cirpka, O.A., R.L. Schwede, J. Luo, and M. Dentz. 2008. Concentration statistics for mixing-controlled reactive transport in random heterogeneous media. J. Contam. Hydrol. 98:61-74.

Clothier, B.E., S.R. Green, and M. Deurer. 2008. Preferential flow and transport in soil: Progress and prognosis. Eur. J. Soil Science 59:2-13.

Coelho, E.F., and D. Or. 1999. Root distribution and water uptake patterns of corn under surface and subsurface drip irrigation. Plant Soil 206:123.

Coutts, M.P. 1987 Developmental processes in tree root systems. Can. J. For. Res. 17:761-767.

Cowan, I.R. 1965. Transport of water in the soil-plant-atmosphere system. J. Appl. Ecol. 2:221-239.

Daily, W., and A. Ramirez. 1995. Electrical resistance tomography during in-situ trichloroethylene remediation at the savanna river site. Journal Appl. Geophys. 33:239-249.

Daily, W., and A.L. Ramirez. 2000. Electrical imaging of engineered hydraulic barriers. Geophysics 65:83-94.

De Rooij, G.H., O.A. Cirpka, F. Stagnitti, S.H. Vuurens, and J. Boll. 2006. Quantifying minimum monolith size and solute dilution from multi-compartment percolation sampler data. Vadose Zone J. 5:1086-1092.

De Rooij, G.H., and F. Stagnitti. 2000. Spatial variability of solute leaching: Experimental validation of a quantitative parameterization. Soil Sci. Soc. Am. J. 64:499-504.

De Rooij, G.H., and F. Stagnitti. 2002. Spatial and temporal distribution of solute leaching in heterogeneous soils: Analysis and application to multisampler lysimeter data. J. Contam. Hydrol. 54:329-346.

de Willigen, P., and M. van Noordwijk. 1987. Roots, plant production and nutrient use efficiency. PhD Thesis. Wageningen University, Wageningen.

Descloitres, M., O. Ribolzi, and Y. Le Troquer. 2003. Study of infiltration in a sahelian gully erosion area using time-lapse resistivity mapping. Catena 53:229-253.

Desmedt, F., and P.J. Wierenga. 1984. Solute transfer through columns of glass beads Water Resour. Res. 20:225-232.

Doussan, C., L. Pagès, and A. Pierret. 2003. Soil exploration and resource acquisition by plant roots: An architectural and modelling point of view. Agronomie 23:419-431.

Doussan, C., A. Pierret, E. Garrigues, and L. Pagès. 2006. Water uptake by plant roots: Ii – modelling of water transfer in the soil root-system with explicit account of flow within the root system – comparison with experiments. Plant Soil 283:99-117.

Draye, X., Y. Kim, G. Lobet, and M. Javaux. 2010. Model-assisted integration of physiological and environmental constraints affecting the dynamic and spatial patterns of root water uptake from soils. J. Exp. Bot. 61:2145-2155.

Dubach, M., and M.P. Ruselle. 1995. Reducing the cost of estimating root turnover with horizontally installed minirhizotrons. Agron. J. 87:258-263.

Dupriez, M. 2010. Effets combinés de la croissance racinaire et de la prise d'eau chez l'orge MSc. thesis UCL, Louvain-la-Neuve.

Durner, W., U. Jansen, and S.C. Iden. 2008. Effective hydraulic properties of layered soils at the lysimeter scale determined by inverse modelling. Eur. J. Soil Sci. 59:114-124.

Edwards, W.M., M.J. Shipitalo, L.B. Owens, and W.A. Dick. 1992. Rainfall intensity affects transport of water and chemicals through macropores in no-till soil. Soil Sci. Soc. Am. J. 56:52-58.

EEA. 2000. Environmental signals 2001. p. 115. Environmental assessment report. European Environment Agency, Copenhagen.

FAO. 2010. Water at a glance. [Online] Available at http://www.fao.org/nr/water/docs/waterataglance.pdf

FAO/ISRIC/ISSS. 1998. World reference base for soil resources World soil resources reports. International Society of Soil Science, Rome.

Feddes, R.A., and P.A.C. Raats. 2004. Parameterizing the soil-water-plant root system. p. 95-141. *In* R.A. Feddes, G.H.d. Rooij, and J.C.v. Dam (ed.) Unsaturated-zone modeling: Progress, challenges and applications. Kluwer, Dordrecht.

Ferre, P.A., J.H. Knight, D.L. Rudolph, and R.G. Kachanoski. 1998. The sample areas of conventional and alternative time domain reflectometry probes. Water Resour. Res. 34:2971-2979.

Feyen, J., D. Jacques, A. Timmerman, and J. Vanderborght. 1998. Modelling water flow and solute transport in heterogeneous soils: A review of recent approaches. J. Agric. Eng. Res. 70:231-256.

Flury, M., H. Fluhler, W.A. Jury, and J. Leuenberger. 1994. Susceptibility of soils to preferential flow of water - a field-study. Water Resour. Res. 30:1945-1954.

Flury, M., and N.N. Wai. 2003. Dyes as tracers for vadose zone hydrology. Rev. Geophys. 41.

French, H., and A. Binley. 2004. Snowmelt infiltration: Monitoring temporal and spatial variability using time-lapse electrical resistivity. J. Hydrol. 297:174-186.

French, H.K., C. Hardbattle, A. Binley, P. Winship, and L. Jakobsen. 2002. Monitoring snowmelt induced unsaturated flow and transport using electrical resistivity tomography. J. Hydrol. 267:273-284.

Freyberg, D.L. 1986. A natural gradient experiment on solute transport in sand aquifer- 2. Spatial moments and the advection and dispersion of nonreactive tracers. Water Resour. Res. 22:2031-2046.

Friedel, S. 2003. Resolution, stability and efficiency of resistivity tomography estimated from a generalized inverse approach. Geophys. J. Int. 153:305-316.

Furman, A., T.P.A. Ferre, and A.W. Warrick. 2004. Optimization of ert surveys for monitoring transient hydrological events using perturbation sensitivity and genetic algorithms. Vadose Zone J. 3:1230-1239.

Gardner, W.R. 1960. Dynamic aspects of water availability to plants. Soil Sci. 89:63-73.

Garré, S., M. Javaux, J. Vanderborght, L. Pagès, and H. Vereecken. 2011. 3-d electrical resistivity tomography to monitor root zone water dynamic. Vadose Zone J In Press.

Garré, S., J. Koestel, T. Guenther, M. Javaux, J. Vanderborght, and H. Vereecken. 2010. Comparison of heterogeneous transport processes observed with electrical resistivity tomography in two soils. Vadose Zone J 9:336-349.

Gharibi, M., and L.R. Bentley. 2005. Resolution of 3-d electrical resistivity images from inversions of 2-d orthogonal lines. Journal of Environmental and Engineering Geophysics 10:339-349.

Giorgi, F., X. Bi, and J.S. Pal. 2004. Mean, interannual variability and trends in a regional climate change experiment over europe. I. Present-day climate (1961–1990). Climate Dynamics 22:733-756.

Gjettermann, B., K.L. Nielsen, C.T. Petersen, H.E. Jensen, and S. Hansen. 1997. Preferential flow in sandy loam soils as affected by irrigation intensity. Soil Technol. 11:139-152.

Glass, R.J., M.J. Nicholl, A.L. Ramirez, and W.D. Daily. 2002. Liquid phase structure within an unsaturated fracture network beneath a surface infiltration event: Field experiment. Water Resour. Res. 38.

Green, S., and B.E. Clothier. 1999. The root zone dynamics of water uptake by a mature apple tree. Plant Soil 206:61-77.

Green, S.R., M.B. Kirkham, and B.E. Clothier. 2006. Root uptake and transpiration: From measurements and models to sustainable irrigation. Agr. Water Manage. 86:165.

Guenther, T., C. Ruecker, and K. Spitzer. 2006. Three-dimensional modelling and inversion of dc resistivity data incorporating topography - ii. Inversion. Geophys. J. Int. 166:506-517.

Hansson, A., and O. Andrén. 1987. Root dynamics in barley, lucerne and meadow fescue investigated with a mini-rhizotron technique. Plant and Soil 103:33-38.

Hansson, A.C., E. Steen, and O. Andrén. 1992. Root growth of daily irrigated and fertilized barley investigated with ingrowth cores, soil cores and minirhizotrons. Swed. J. Agric. Res. 22:141-152.

Hargreaves, C., P. Gregory, and A. Bengough. 2009. Measuring root traits in barley (hordeum vulgare ssp. Vulgare and ssp. Spontaneum) seedlings using gel chambers, soil sacs and x-ray microtomography. Plant and Soil 316:285-297.

Haustein, S., B. Mittermaier, and D. Tunger. 2009. Bibliometric analysis asia-pacific research area. p. 149. International Bureau of the BMBF Bonn.

Heeraman, D.A., P.H. Crown, and N.G. Juma. 1993. A color composite technique for detecting root dynamics of barley from minirhizotron images. Plant Soil 157:275-287.

Heimovaara, T.J. 1993. Design of triple-wire time domain reflectometry probes in practice and theory. Soil Sci. Soc. Am. J. 57:1410-1417.

Heimovaara, T.J. 1995. Assessing temporal variations in soil water composition with time domain reflectometry. Soil Sci. Soc. Am. J. 59:689-698

Hendrick, R.L., and K.S. Pregitzer. 1996. Applications of minirhizotrons to understand root function in forests and other natural ecosystems. Plant Soil 185:293-304.

Henry-Poulter, S. 1996. An investigation of transport properties in natural soils using electrical resistance tomography. Unpublished Ph.D. Lancaster, Lancaster.

Herrmann, K.H., A. Pohlmeier, D. Gembris, and H. Vereecken. 2002. Three-dimensional imaging of pore water diffusion and motion in porous media by nuclear magnetic resonance imaging. J. Hydrol. 267:244-257.

Hillel, D. 1998. Environmental soil physics. p. 771. Academic press. Elsevier, San Diego.

Hoffman, F., D. Ronen, and Z. Pearl. 1996. Evaluation of flow characteristics of a sand column using magnetic resonance imaging. J. Contam. Hydrol. 22:95-107.

Hopmans, J.W., and K.L. Bristow. 2002. Current capabilities and future needs of root water and nutrient uptake modeling. Advances in Agronomy 77:103-183.

Hupet, F., S. Lambot, M. Javaux, and M. Vanclooster. 2002a. On the identification of macroscopic root water uptake parameters from soil water content observations. Water resources research 38:1300.

Itoh, S. 1985. In situ measurement of rooting density by micro-rhizotron. Japanese Society of Soil Science and Plant Nutrition, Tokyo, Japan.

Jackson, R.B. 2000. Root water uptake and transport: Using physiological processes in global predictions. Trends in plant science 5:482.

Javaux, M., R. Kasteel, J. Vanderborght, and M. Vanclooster. 2006. Interpretation of dye transport in a macroscopically heterogeneous, unsaturated subsoil with a one-dimensional model. Vadose Zone J. 5:529-538.

Javaux, M., T. Schroder, J. Vanderborght, and H. Vereecken. 2008. Use of a three-dimensional detailed modeling approach for predicting root water uptake. Vadose Zone J. 7:1079-1088.

Javaux, M., and M. Vanclooster. 2003. Scale- and rate-dependent solute transport within an unsaturated sandy monolith. Soil Sci. Soc. Am. J. 67:1334-1343.

Jaynes, D.B., S.I. Ahmed, K.-J.S. Kung, and R.S. Kanwar. 2001. Temporal dynamics of preferential flow to a subsurface drain. Soil Sci Soc Am J 65:1368-1376.

Johnson, M.G., D.T. Tingey, D.L. Phillips, and M.J. Storm. 2001. Review: Advancing fine root research with minirhizotrons. Environ. Exp. Bot. 45:263-289.

Jury, W.A., and K. Roth. 1990. Transfer functions and solute movement through soil. Theory and applications. Birkhäuser Verlag, Basel, Switzerland.

Kanti Sen, T., and K.C. Khilar. 2006. Review on subsurface colloids and colloid-associated contaminant transport in saturated porous media. Adv. Colloid Interface Sci. 119:71-96.

Kasteel, R., H.J. Vogel, and K. Roth. 2002. Effect of non-linear adsorption on the transport behaviour of brilliant blue in a field soil. Eur. J. Soil. Sci. 53:231-240.

Katul, G., F. Todd, D. Pataki, Z.J. Kabala, and R. Oren. 1997. Soil water depletion by oak trees and the influence of root water uptake on the moisture content spatial statistics. Water Resourc. Res. 33:611.

Kemna, A. 2000. Tomographic inversion of complex resistivity: Theory and application. Der Andere Verlag, Osnabrück.

Kemna, A., J. Vanderborght, B. Kulessa, and H. Vereecken. 2002. Imaging and characterisation of subsurface solute transport using electrical resistivity tomography (ert) and equivalent transport models. J. Hydrol. 267:125-146.

Kitanidis, P.K. 1994. The concept of the dilution index. Water Resour. Res. 30:2011-2026.

Koestel, J., A. Kemna, M. Javaux, A. Binley, and H. Vereecken. 2008. Quantitative imaging of solute transport in an unsaturated and undisturbed soil monolith with 3-d ert and tdr. Water Resour. Res. 44:17.

Koestel, J., J. Vanderborght, M. Javaux, A. Kemna, A. Binley, and H. Vereecken. 2009. Non-invasive 3d transport characterization in a sandy soil using ert i: Investigating the validity of ert-derived transport parameters. Vadose Zone J. 8:711-722.

Koestel, J., J. Vanderborght, M. Javaux, A. Kemna, A. Binley, and H. Vereecken. 2009. Non-invasive 3d transport characterization in a sandy soil using ert ii: Transport process inference. Vadose Zone J. 8:723-734

Kohl, M., U. Böttcher, and H. Kage. 2007. Comparing different approaches to calculate the effects of heterogeneous root distribution on nutrient uptake: A case study on subsoil nitrate uptake by a barley root system. Plant and Soil 298:145-159.

Koster, R.D., Y.C. Sud, Z. Guo, P.A. Dirmeyer, G. Bonan, K.W. Oleson, E. Chan, D. Verseghy, P. Cox, H. Davies, E. Kowalczyk, C.T. Gordon, S. Kanae, D. Lawrence, P. Liu, D. Mocko, C.-H. Lu, K. Mitchell, S. Malyshev, B. McAvaney, T. Oki, T. Yamada, A. Pitman, C.M. Taylor, R. Vasic, and Y. Xue. 2006. Glace: The global land-atmosphere coupling experiment. Part i: Overview. J. Hydrometeor. 7:590-610.

Koumanov, K., J. Hopmans, and L. Schwankl. 2006. Spatial and temporal distribution of root water uptake of an almond tree under microsprinkler irrigation. Irrigation Science 24:267-278.

Kreft, A., and A. Zuber. 1978. On the physical meaning of the dispersion equation and its solutions for different initial and boundary conditions. Chem. Eng. Sci. 33:1471-1480

LaBrecque, D.-J., D. Alumbaugh, X.J. Yang, L. Paprocki, and J.R. Brainard. 2002. Three-dimensional monitoring of vadose zone infiltration using electrical resistivity tomography and cross-borehole ground-penetrating radar. Meth. Geoch.

LaBrecque, D.J., M. Miletto, W. Daily, A. Ramirez, and E. Owen. 1996. The effects of noise on occam's inversion of resistivity tomography data. Geophysics 61:538-548.

Levan, M.A., J.W. Ycas, and J.W. Hummel. 1987. Light leak effects on near surface soybean rooting observed with minirhizotrons. p. 89-98. *In* H.M. Taylor (ed.) Minirhizotron observation tubes: Methods and applications for measuring rhizosphere dynamics. Madison.

Lindsey, R. 2009. Climate and earth's energy budget. [Online] Available at http://earthobservatory.nasa.gov/Features/EnergyBalance/page5.php (accessed August 10, 2010)

Looms, M.C., K.H. Jensen, A. Binley, and L. Nielsen. 2008. Monitoring unsaturated flow and transport using cross-borehole geophysical methods. Vadose Zone J. 7:227-237.

Lyford, W.H. 1980 Development of the root system of northern red oak (quercus rubra l.). Harv. For. Pa. 21:1-30.

Maillet, G.M., E. Rizzo, A. Revil, and C. Vella. 2005. High resolution electrical resistivity tomography (ert) in a transition zone environment: Application for detailed internal architecture and infilling processes study of a rhone river paleo-channel. Marine Geophysical Researches 26:317-328.

Mallants, D., M. Vanclooster, N. Toride, J. Vanderborght, M.T. van Genuchten, and J. Feyen. 1996. Comparison of three methods to calibrate tdr for monitoring solute movement in undisturbed soil. Soil Sci. Soc. Am. J. 60:747-754.

Maxwell, R.M., and S.J. Kollet. 2008. Interdependence of groundwater dynamics and land-energy feedbacks under climate change. Nature Geosci 1:665-669.

McMichael, B.L., and H.M. Taylor. 1987. Applications and limitations of rhizotrons and minirhizotrons. p. 1-13. *In* H.M. Taylor (ed.) Minirhizotron

observation tubes: Methods and applications for measuring rhizosphere dynamics. Madison.

Merrill, S.D., and D.R. Upchurch. 1994. Converting root numbers observed at minirhizotrons to equivalent root length density. Soil Sci. Soc. Am. J. 58:1061-1067.

Michot, D., Y. Benderitter, A. Dorigny, B. Nicoullaud, D. King, and A. Tabbagh. 2003. Spatial and temporal monitoring of soil water content with an irrigated corn crop cover using surface electrical resistivity tomography. Water Resour. Res. 39.

Molz, F.J. 1981. Models of water transport in the soil-plant system: A review. Water Resour. Res. 17:1245-1260.

Mooney, S.J., and C. Morris. 2008. A morphological approach to understanding preferential flow using image analysis with dye tracers and x-ray computed tomography. Catena 73:204-211.

Musters, P.A.D., and W. Bouten. 1999. Assessing rooting depths of an austrian pine stand by inverse modeling soil water content maps. Water Resour. Res. 35:3041-3048.

Musters, P.A.D., and W. Bouten. 2000. A method for identifying optimum strategies of measuring soil water contents for calibrating a root water uptake model. J. Hydrol. 227:273-286.

Oberdörster, C., J. Vanderborght, A. Kemna, and H. Vereecken. 2010. Monitoring and imaging preferential flow processes in a forest soil with tdr and ert. Vadose Zone J. 9:350-361.

Olsen, P.A., A. Binley, S. Henry-Poulter, and W. Tych. 1999. Characterizing solute transport in undisturbed soil cores using electrical and x-ray tomographic methods. Hydrol. Processes 13:211-221.

Oswald, S., W. Kinzelbach, A. Greiner, and G. Brix. 1997. Observation of flow and transport processes in artificial porous media via magnetic resonance imaging in three dimensions. Geoderma 80:417-429.

Padilla, I.Y., T.C.J. Yeh, and M.H. Conklin. 1999. The effect of water content on solute transport in unsaturated porous media. Water Resources Research 35:3303-3313.

Pagès, L., M.O. Jordan, and D. Picard. 1989. A simulation model of the three-dimensional architecture of the maize root system. Plant and Soil 119:147-154.

Pagès, L., G. Vercambre, J.-L. Drouet, F. Lecompte, C. Collet, and J. Le Bot. 2004. Root typ: A generic model to depict and analyse the root system architecture. Plant and Soil 258:103-119.

Parker, C.J., M.K.V. Carr, N.J. Jarvis, B.O. Puplampu, and V.H. Lee. 1991. An evaluation of the minirhizotron technique for estimating root distribution in potatoes. The Journal of Agricultural Science 116:341-350.

Picard, D., M.O. Jordan, and R. Trendel. 1985. Rythme d'apparition des racines primaires du maïs (zea mays l.) i. — etude détaillée pour une variété en un lieu donné. Agronomie 5:667-676.

Pimentel, D., J. Houser, E. Preiss, O. White, H. Fang, L. Mesnick, T. Barsky, S. Tariche, J. Schreck, and S. Alpert. 1997. Water resources:Agriculture, the environment, and society. An assessment of the status of water resource. BioScience 47:97-106.

Pohlmeier, A., A. Oros-Peusquens, M. Javaux, M.I. Menzel, J. Vanderborght, J. Kaffanke, S. Romanzetti, J. Lindenmair, H. Vereecken, and N.J. Shah. 2008. Changes in soil water content resulting from root uptake monitored by magnetic resonance imaging. Vadose Zone J. 7:1010-1017.

Poletika, N.N., and W.A. Jury. 1994. Effects of soil surface management on water-flow distribution and solute-dispersion. Soil Sci. Soc. Am. J. 58:999-1006.

Pütz, T. 1993. Lysimeterversuche zum verlagerungsverhalten von methabenzthiazuron und gelöstem organischen kohlenstoff in einer parabraunerde, aufbau von zwei klimameßstationen und untersuchungen zur validierung des lysimetersystems. p. 1-223. Berichte des Forschungszentrums Jülich. Jülich.

Quisenberry, V.L., R.E. Phillips, and J.M. Zeleznik. 1994. Spatial distribution of water and chloride macropore flow in a well-structured soil. Soil Sci. Soc. Am. J. 58:1294-1300.

Reinken, G. 2004 Bodenphysikalische untersuchungen zur prozeßanalyse der wasserbewegung und des stofftransportes in ungesättigten, strukturierten böden unter besonderer berücksichtigung der mechanismen der präferentiellen wirkstoffverlagerung. PhD Thesis Univ. Köln

Revil, A., L.M. Cathles, S. Losh, and J.A. Nunn. 1998. Electrical conductivity in shaly sands with geophysical applications. Journal of Geophysical Research-Solid Earth 103:23925-23936.

Robinson, D.A., S.B. Jones, J.M. Wraith, D. Or, and S.P. Friedman. 2003. A review of advances in dielectric and electrical conductivity measurement in soils using time domain reflectometry. Vadose Zone J. 2:444-475.

Roose, T., and A. Schnepf. 2008. Mathematical models of plant-soil interaction. Philos. Trans. R. Soc. A-Math. Phys. Eng. Sci. 366:4597-4611.

Roth, K., and K. Hammel. 1996. Transport of conservative chemical through an unsaturated two-dimensional miller-similar medium with steady state flow. Water Resour. Res. 32:1653–1663.

Salamon, P., D. Fernàndez-Garcia, and J.J. Gómez-Hernàndez. 2007. Modeling tracer transport at the made site: The importance of heterogeneity. Water Resour. Res. 43:W08404.

Sander, T., and H.H. Gerke. 2007. Preferential flow patterns in paddy fields using a dye tracer. Vadose Zone J. 6:105-115.

Sanders, J.L., and D.A. Brown. 1978. A new fiber optic technique for measuring root growth of soybeans under field conditions. Agron J 70:1073-1076.

Schar, C., P.L. Vidale, D. Luthi, C. Frei, C. Haberli, M.A. Liniger, and C. Appenzeller. 2004. The role of increasing temperature variability in european summer heatwaves. Nature 427:332-336.

Schmidt-Eisenlohr, A. 2001. Räumliche und zeitliche variabilität von bodenparametern und die beschreibung des wassertransports in einer parabraunerde aus schwemmlöß in der jülicher börde. Rheinische Friedrich-Wilhelms Universität, Bonn.

Schneider, C.L., S. Attinger, J.O. Delfs, and A. Hildebrandt. 2010. Implementing small scale processes at the soil-plant interface - the role of root

architectures for calculating root water uptake profiles. Hydrol. Earth Syst. Sci. 14:279-289.

Schoen, R., J.P. Gaudet, and T. Bariac. 1999. Preferential flow and solute transport in a large lysimeter, under controlled boundary conditions. J. Hydrol. 215:70-81.

Schröder, T. 2009. Three-dimensional modelling of soil-plant interactions: Consistent coupling of soil and plant root systems. Ias series. Forschungszentrum Jülich Zentralbibliothek, Verlag, Jülich.

Schröder, T., M. Javaux, J. Vanderborght, B. Korfgen, and H. Vereecken. 2008. Effect of local soil hydraulic conductivity drop using a three-dimensional root water uptake model. Vadose Zone J. 7:1089-1098.

Seneviratne, S.I., D. Luthi, M. Litschi, and C. Schar. 2006. Land-atmosphere coupling and climate change in europe. Nature 443:205-209.

Seuntjens, P., D. Mallants, N. Toride, C. Cornelis, and P. Geuzens. 2001. Grid lysimeter study of steady state chloride transport in two spodosol types using tdr and wick samplers. J. Contam. Hydrol. 51:13-39.

Sharp, R.E., and W.J. Davies. 1985. Root growth and water uptake by maize plants. J. Exp. Bot. 36:1441-1456.

Sharp, R.E., and W.J. Davies. 1985. Root growth and water uptake by maize plants in drying soil. J. Exp. Bot. 36:1441-1456.

Shiklomanov, I.A. 1993. World fresh water resources p. 13-24 *In* G. P. (ed.) Water in crisis: A guide to the world's fresh water resources. Oxford University Press, Oxford (UK).

Singha, K., and S.M. Gorelick. 2006. Effects of spatially variable resolution on field-scale estimates of tracer concentration from electrical inversions using archie's law. Geophysics 71:G83-G91.

Singha, K., and S. Moysey. 2006. Accounting for spatially variable resolution in electrical resistivity tomography through field-scale rock-physics relations. Geophysics 71:A25-A28.

Slater, L., A. Binley, R. Versteeg, G. Cassiani, R. Birken, and S. Sandberg. 2002. A 3d ert study of solute transport in a large experimental tank. J. Appl. Geophys. 49:211-229.

Slater, L.D., A. Binley, and D. Brown. 1997. Electrical imaging of fractures using ground-water salinity change. Ground Water 35:436-442.

Slater, L.D., and S.K. Sandberg. 2000. Resistivity and induced polarization monitoring of salt transport under natural hydraulic gradients. Geophysics 65:408-420.

Smit, A.L., E. George, and J. Groenwold. 2000. Root observations and measurements at (transparant) interfaces with soil. p. 587. *In* A.L. Smit, A.G. Bengough, C. Engelset al (ed.) Root methods: A handbook. Springer, Berlin.

Srayeddin, I., and C. Doussan. 2009. Estimation of the spatial variability of root water uptake of maize and sorghum at the field scale by electrical resistivity tomography. Plant Soil 319:185-207.

Stagnitti, F., L. Li, G. Allinson, I. Phillips, D. Lockington, A. Zeiliguer, M. Allinson, J. Lloyd-Smith, and M. Xie. 1999. A mathematical model for estimating the extent of solute- and water-flux heterogeneity in multiple sample percolation experiments. J. Hydrol. 215:59-69.

Stagnitti, F., N. Villiers, J.Y. Parlange, T.S. Steenhuis, G.H. de Rooij, L. Li, D.A. Barry, X. Xiong, and P. Li. 2003. Solute and contaminant transport in heterogeneous soils. B. Environ. Contam. Tox. 71:737-745.

Steele, S.J., S.T. Gower, J.G. Vogel, and J.M. Norman. 1997. Root mass, net primary production and turnover in aspen, jack pine and black spruce forests in saskatchewan and manitoba, canada. Tree Physiol 17:577-587.

Steenhuis, T.S., J.Y. Parlance, and M.S. Andreini. 1990. A numerical model for preferential solute movement in structured soils. Geoderma 46:193-208.

Stubben, M., and D. LaBrecque. 1998. 3-d ert inversion used to monitor an infiltration experiment. Proceedings of the Symposium on the Application of Geophysics to Environmental and Engineering Problems (SAGEEP) 1998.

Stummer, P., H. Maurer, and A.G. Green. 2004. Experimental design: Electrical resistivity data sets that provide optimum subsurface information. Geophysics 69:120-139.

Taylor, H.M., M.G. Huck, B. Klepper, and Z.F. Lund. 1970. Measurement of soil-grown roots in a rhizotron. Agron J 62:807-809.

Teuling, A.J., and P.A. Troch. 2005. Improved understanding of soil moisture variability dynamics. Geophys. Res. Lett. 32:L05404: 1-4.

Topp, G.C. 1980. Electromagnetic determination of soil water content: Measurements in coaxial transmission lines. Water Resour. Res. 16:574-582.

Tracy, S.R., J.A. Roberts, C.R. Black, A. McNeill, R. Davidson, and S.J. Mooney. 2010. The x-factor: Visualizing undisturbed root architecture in soils using x-ray computed tomography. J. Exp. Bot. 61:311-313.

Upchurch, D.R., and J.T. Ritchie. 1983. Root observations using a video recording system in mini-rhizotrons. Agron. J. 75:1009-1015.

van Genuchten, M.T., and J.C. Parker. 1984. Boundary-conditions for displacement experiments through short laboratory soil columns. Soil Sci. Soc. Am. J. 48:703-708.

van Lier, Q.d.J., K. Metselaar, and J.C. van Dam. 2006. Root water extraction and limiting soil hydraulic conditions estimated by numerical simulation. Vadose Zone J. 5:1264-1277.

Vanclooster, M., M. Javaux, and J. Vanderborght. 2005. Solute transport in soil at the core and field scale. p. 1041-1055. *In* M.G. Anderson (ed.) Encyclopedia of Hydrological Sciences. Wiley, New York.

Vanderborght, J., D. Jacques, and J. Feyen. 2000. Deriving transport parameters from transient flow leaching experiments by approximate steady-state flow convection-dispersion models. Soil Sci. Soc. Am. J. 64:1317-1327.

Vanderborght, J., R. Kasteel, and H. Vereecken. 2006. Stochastic continuum transport equations for field-scale solute transport: Overview of theoretical and experimental results. Vadose Zone J. 5:184-203.

Vanderborght, J., A. Kemna, H. Hardelauf, and H. Vereecken. 2005. Potential of electrical resistivity tomography to infer aquifer transport characteristics from tracer studies: A synthetic case study. Water Resour. Res. 41.

Vanderborght, J., A. Timmerman, and J. Feyen. 2000. Solute transport for steady-state and transient flow in soils with and without macropores. Soil Sci. Soc. Am. J. 64:1305-1317.

Vanderborght, J., M. Vanclooster, A. Timmerman, P. Seuntjens, D. Mallants, D.J. Kim, D. Jacques, L. Hubrechts, C. Gonzalez, J. Feyen, J. Diels, and J. Deckers. 2001. Overview of inert tracer experiments in key belgian soil types: Relation between transport and soil morphological and hydraulic properties. Water Resour. Res. 37:2873-2888.

Vanderborght, J., and H. Vereecken. 2007. Review of dispersivities for transport modeling in soils. Vadose Zone J. 6:29-52.

Vercambre, G., L. Pagès, C. Doussan, and R. Habib. 2003. Architectural analysis and synthesis of the plum tree root system in an orchard using a quantitative modelling approach. Plant Soil 251:1-11.

Vereecken, H., J.A. Huisman, H. Bogena, J. Vanderborght, J.A. Vrugt, and J.W. Hopmans. 2008. On the value of soil moisture measurements in vadose zone hydrology: A review. Water Resour. Res. 44:W00D06.

Vereecken, H., T. Kamai, T. Harter, R. Kasteel, J. Hopmans, and J. Vanderborght. 2007. Explaining soil moisture variability as a function of mean soil moisture: A stochastic unsaturated flow perspective. Geophys. Res. Lett. 34:L22402.

Vidale, P.L., D. Lüthi, R. Wegmann, and C. Schär. 2007. European summer climate variability in a heterogeneous multi-model ensemble. Anglais 81:209-232.

Vogel, H.J., I. Cousin, O. Ippisch, and P. Bastian. 2006. The dominant role of structure for solute transport in soil: Experimental evidence and modelling of structure and transport in a field experiment. Hydrol. Earth Syst. Sci. 10:495-506.

Vos, J., and J. Groenwold. 1987. The relation between root growth along observation tubes and in bulk soil. p. 39–49. *In* H.M. Taylor (ed.) Minirhizotron observation tubes: Methods and applications for measuring rhizosphere dynamics. Madison.

Vrugt, J.A., J.W. Hopmans, and J. Simunek. 2001. Calibration of a two-dimensional root water uptake model. Soil Sci Soc Am J 65:1027-1037.

Vrugt, J.A., M.T. van Wijk, J.W. Hopmans, and J. Simunek. 2001. One-, two-, and three-dimensional root water uptake functions for transient modeling. Water Resour. Res. 37:2457-2470.

Wahbi, A., and P.J. Gregory. 1995. Growth and development of young roots of barley (hordeum vulgare l.) genotypes. Annals of Botany 75:533-539.

Waxman, M.H., and L.J.M. Smits. 1968. Electrical conductivities in oil-bearing shaly sands. Soc. Petrol. Eng. J. 8:107-&.

Weihermueller, L. 2005. Comparison of different soil water extraction systems for the prognoses of solute transport at the field scale using numerical simulations, field and lysimeter experiments. Rheinische Friedrich-Wilhelms Universität, Bonn.

Wells, C.E., and S. Birchfield. 2009. Rootfly: Software for minirhizotron image analysis. Clemson University.

Werban, U., S.A.a. Hagrey, and W. Rabbel. 2008. Monitoring of root-zone water content in the laboratory by 2d geoelectrical tomography. J. Plant Nutr. Soil Sc. 171:927-935.

WRI. 2005. Agriculture and food. Data tables. http://earthtrends.wri.org/datatables/index.php?theme=8. World Resources Institute.

Zenone, T., G. Morelli, M. Teobaldelli, F. Fischanger, M. Matteucci, M. Sordini, A. Armani, C. Ferre, T. Chiti, and G. Seufert. 2008. Preliminary use of ground-penetrating radar and electrical resistivity tomography to study tree roots in pine forests and poplar plantations. Commonwealth Scientific and Industrial Research Organization, Collingwood, Australia.

Zhou, Q.Y., J. Shimada, and A. Sato. 2002. Temporal variations of the three-dimensional rainfall infiltration process in heterogeneous soil. Water Resourc. Res. 38.